HALTERE MEDIATED FLIGHT STABILIZATION IN DIPTERA: RATE DECOUPLING, SENSORY ENCODING, AND CONTROL REALIZATION

By

RHOE A. THOMPSON

A DISSERTATION PRESENTED TO THE GRADUATE SCHOOL
OF THE UNIVERSITY OF FLORIDA IN PARTIAL FULFILLMENT
OF THE REQUIREMENTS FOR THE DEGREE OF
DOCTOR OF PHILOSOPHY

UNIVERSITY OF FLORIDA

2009

I dedicate this work to
my wife, Ann, and children, Ryan, Rachel, and Jessica.

ACKNOWLEDGMENTS

I would like to acknowledge my committee chair, Dr. Warren Dixon, for his timely words of encouragement and the example he has provided. His passion for his work and professionalism have been a motivational factor in the success of all of his students. I would also like to acknowledge the other members of my committee, Dr. Carl Crane, Dr. Norman Fitz-Coy, Dr. Daniel Hahn, Mr. Ric Wehling and Mr. Johnny Evers for taking the time to review my work and for providing insightful suggestions for improvement.

I would like to acknowledge the many distinguished professors I have learned from over the years at the University of Florida, one of the most memorable being the late Prof. Knox Millsaps. To the dismay of some students, Prof. Millsaps would at times spend much of his class telling fascinating stories about his career and the historical figures he had encountered. He told us once, "Learning is best accomplished late at night, solving problems in the company of a good text book and a desk lamp." I have come to believe that the stories he told to motivate the desire to learn were at least as important as the examples he worked on the board. Learning from Prof. Millsaps and the other outstanding members of the University of Florida faculty has been an honor.

I would like to thank the Air Force Research Laboratory which allowed me a paid sabbatical to pursue my PhD studies and then minimal disturbance when I returned to complete my degree. In particular, I would like to thank Ms. Sandra Lefstad for being supportive when I brought up the idea of leaving my job to go back to school. In general, AFRL deserves a great deal of credit for fostering innovation and allowing engineers to study biological systems in search of revolutionary new technologies.

Finally, I must acknowledge the many scientists who have laid the foundation for this research. Their ingenuity and never ending fascination with an animal as maligned as the fly have inspired me at every step of the way. Their work convinces me that there are many scientists who understand that love for this world's ever evolving creation is more than a personal passion, it is also a gift back to life's source.

TABLE OF CONTENTS

LIST OF TABLES

LIST OF FIGURES

Abstract of dissertation Presented to the Graduate School
of the University of Florida in Partial Fulfillment of the
Requirements for the Degree of Doctor of Philosophy

HALTERE MEDIATED FLIGHT STABILIZATION IN DIPTERA:
RATE DECOUPLING, SENSORY ENCODING, AND CONTROL REALIZATION

By

Rhoe A. Thompson

August 2009

Chair: Dr. Warren Dixon
Major: Mechanical and Aerospace Engineering

Insects of the order Diptera have a single pair of wings. The rear wings of Dipteran insects have evolved into organs that allow stabilizing control responses through sensing and encoding of body angular rate feedback. This dissertation documents research on the physical and physiological mechanisms that enable a pair of halteres to distinguish and encode three orthogonal components of the body rate vector. While the knowledge that the halteres play a role in flight stability has been prevalent for centuries, the understanding of how insect's very simple sensory structures are able to encode and decouple the orthogonal components of the rate vector has been lacking. The work described in this report furthers this understanding through modeling and simulation. First, a natural decoupling of the observable rate components has been identified that asserts proportionality of body rate components to averaged strain characteristics near the center of the haltere stroke. Second, a means of encoding and decoding the necessary rate information in a manner compatible with the insect's sensory structures and flight motor physiology has been identified and demonstrated. Finally, the ability of the proposed haltere model to stabilize flight in a 6DOF environment with competing behavioural objectives and randomly generated obstructions has been demonstrated.

CHAPTER 1
INTRODUCTION AND PROBLEM STATEMENT

Insects have evolved the ability to perform stable flight within the constraints of many competing objectives that influence wing and body form. Optical and inertial feedback for motion control is expressed in great variety in biological control system architectures. The order Diptera, commonly referred to as "flies," has differentiated over hundreds of millions of years in to several hundred thousand species that have only two wings. In the dipterans, which include many of the most dynamic flying forms of insects, the rear wings evolved in the mid-Triassic period into small club like structures that oscillate out of phase but at the same frequency as the wings during flight (Figure 1-1). In some species haltere oscillation also occurs during walking on the ground without wing motion, indicating that the halteres might impart stability during other modes of locomotion. The halteres have been likened to gyroscopes, providing inertial rate feedback to both wing, leg and neck muscle functions.

The history of haltere research will be reviewed in detail in Chapter 2. The halteres have been documented as necessary for flight stability since the early 18th century. Not until the early- to mid-twentieth century was sufficient evidentiary data and analysis provided to convince the scientific community that halteres influenced flight stability through their role as an inertial rate feedback sensor. While data associated with neurological pathways and compensatory responses has been abundant, the details about the mechanism by which the halteres are able to decouple the body rate components has been lacking. The lack of details is in part due to an emphasis in the biological community on higher system level interactions between the haltere and the wing and neck control structures, and in part due to the difficulty in untangling the signals associated with haltere mechano-sensory complex. At the base of the haltere are between three and four hundred individual strain sensors, called campaniform sensilla, on the surface of the cuticle. Internal to the hinge are other sensory structures, the chordotonal organs,

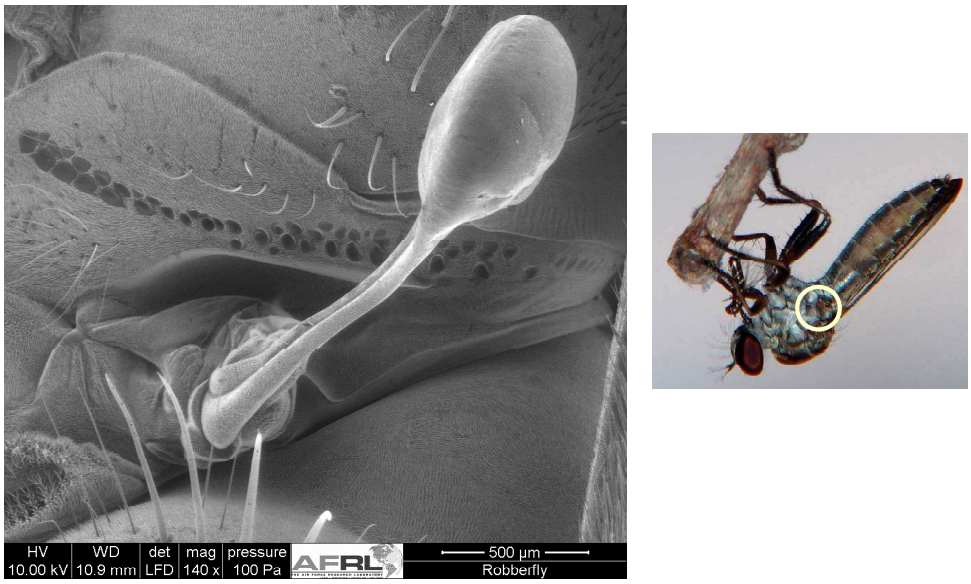

Figure 1-1. Environmental Scanning Electron Micrograph (ESEM) of the haltere of the robber fly, family *Asilidae*. Image collected at Eglin AFB, July 2008.

thought to be sensitive in extension only. As of this time, very little detailed knowledge exists about the function and purpose of the majority of these sensors. Compounding the problem is the difficulty differentiating individual nerve fibers in the bundle that leaves the haltere. Typically, compound extracellular potentials are measured as opposed to measurements known to be expressed from individual sensillum, although more recently there have been examples of more detailed measurements [1], [2].

One objective of this dissertation is to expand upon the current knowledge of the mechanics of the haltere. While several biologists have applied kinematic analysis of the haltere, none have gone to the level of simulating the dynamics of the haltere. This research goes to that level and as a result has uncovered mechanisms that may explain how dipterans decouple two rate components in the plane of each haltere. With two rate components from two halteres an orthogonal triad can be constructed which explains compensatory flight and head responses to orthogonal rate disturbances. Researchers in the early 20th century discovered unique frequency characteristics associated with the Coriolis forces acting on the halteres (Figure 1-2). From that time forward, decoupling

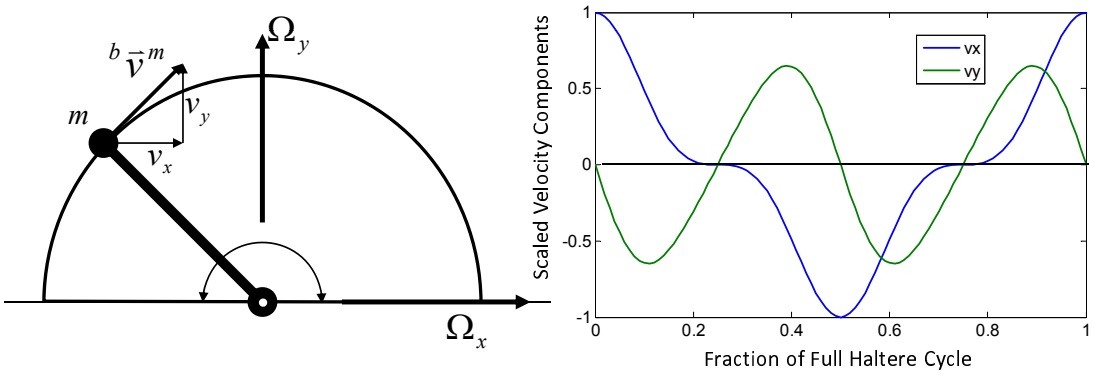

Figure 1-2. The Coriolis force changes sign as the velocity component perpendicular to the rate component changes sign (w cross v).

based on frequency characteristics has been assumed by most of the scientific community without further substantiation. While the frequency content of the driving forces must be represented in the continuous response of the halteres, the sensory mechanisms involved are not continuous. The sensilla are thought to fire at some threshold near saturation only in a unidirectional sense, once or twice per stroke cycle. Therefore, the halteres may only provide output when forced out of plane in one direction. Also, there are indications that the signals near the ends of the stroke are dominated by the accelerations associated with haltere motion reversal. This means that the smooth idealistic representations of Figure 1-2 are far from from representative of the true haltere afferents. In part, the goal of this research was to look for other possible means by which rate decoupling could occur that are directly compatible with the haltere sensory physiology.

Chapter 3 of this dissertation provides a detailed analysis of the kinematics and dynamics of the haltere, demonstrating that an alternative decoupling mechanism does exist if measurements proportional to averaged strain and strain rate near the center of the stroke are available. This result is limited to cases involving constant inertial rates although the impact of angular accelerations are discussed to some extent. Chapter 4 attempts to reconcile the physical model of the ideal haltere with the realities of what

is known about the sensory structure at the base of the haltere and the experimental observations by a number of authors of compensatory responses and neurological pathways to the motor control functions of the wings and the neck. In particular, averaged strain and strain rate must be shown to be proportional to some characteristic of a signal coming out of the a field of approximately 110 rapidly saturated strain sensors that only respond in one direction. The role of the chordotonal organ within the haltere is assumed to have no impact on rate measurement although this should not be entirely ruled out from a theoretical perspective if no other means is found to obtain the necessary signals. There is, however, no experimental evidence of its influence. Chapter 5 demonstrates the closed-loop performance of the haltere in environments involving more general controlled motion. A 6DOF simulation with the general inertial characteristics of a fly is described that uses a navigation solution that combines the influence of competing objectives through summation of non-linear activation functions. The simulated fly is shown to navigate through a complex, unanticipated environment of obstructions prior to homing in on a predefined target location. Comparison between flight with exact knowledge of inertial rates and haltere measurements of rates is used to demonstrate the viability of the proposed rate decoupling scheme in the presence of highly dynamic motion. Additionally, Chapter 5 addresses the impact of control cross coupling and ipsilateral versus bilateral feedback to the flight control functions. Finally, Chapter 6 summarizes the accomplishments and shortcomings of this assessment of the haltere and the proposed mechanism for rate decoupling.

Roland Hengstenberg [3] concisely states the deficit in knowledge regarding the haltere that this dissertation attempts to address:

> At present, the central projections of the haltere sensilla are only coarsely known, and it is totally unknown how *Calliphora* extracts, from the spatio-temporal pattern of excitation of haltere sensilla, the information to control its head and wings correctly.

CHAPTER 2
HISTORICAL SUMMARY OF HALTERE RESEARCH

The research on halteres relative to flight stability has been limited to a few dozen researchers over the last two centuries. These researchers have been predominantly biologists with a general prerequisite background in physics, but no formal training in control system design or engineering mechanics. More recently, with greatly increased interest in robotics and micro- air vehicles there has been more multi-disciplinary involvement, even to the point of attempts to patent and build mechanical versions of a haltere [4]. Understanding of the haltere and its system level implications requires understanding of insect physiology, engineering mechanics, and the fundamentals of control system design. Since the haltere is an integral part of a system that involves electro-optical sensing and aerodynamic actuation, knowledge of the constraints imposed by the subjects of these disciplines is also quite helpful. Following is a summary of the literature involving halteres.

2.1 Theories for the Haltere's Stabilizing Influence

Early theories on the function of the haltere are summarized by Gottfried Fraenkel [5]. In 1714, Derham proposed that the halteres were organs which provided mechanical balance similar to the pole of a tight rope walker [6]. Loew, in 1858, assessed the mass of the halteres to be much too small to influence the equilibrium of the fly by their own movements [7]. This corroborated the observation by Schelver in 1802, that removal of a single haltere only had a small impact on flight stability [8]. Two other theories for the influence of the halteres were proposed that were quickly rejected. In 1878, Jousset de Bellesme proposed that the halteres influence the wing motion through mechanical interference during the downstroke [9]. The anatomy of the insects was shown to make this impossible. Weinland, in 1891, proposed that the halteres are moved fore and aft to change the center of gravity, a theory which it appears had already been excluded as a possiblity by Loew [7], [10]. Buddenbrock, in papers published in 1917 and 1919, ignored

previous facts that led to the consideration of halteres as organs of "balance" and asserted that halteres act to stimulate the central nervous system into a state of activity necessary for flight [11], [12]. His reasoning was later shown to be invalid as described below.

An article was published in 1938 by G. Fraenkel and J.W.S. Pringle [13] that rejected the assertion by Buddenbrock [12]. The reasoning provided is as follows: 1) the flight reflex can be induced in flies whether or not they have intact halteres, 2) any loss of spontaneity of the flight reflex is a transient phenomenon, 3) amplitude and wingbeat after ablating the halteres is identical to normal flies, 4) reduction of flight motor stimulation through fatigue does not reduce stability, but haltere removal causes complete lack of control, 5) loss of control is particularly pronounced in yaw, and 6) attaching a piece of cotton thread to the abdomen almost eliminates the instability resulting from loss of the halteres. The following year Fraenkel elaborated considerably on his arguments against Bruddenbrock, adding facts such as the observation of haltere activity during walking and the flight instability of a bithorax mutant of the fruit fly which has two sets of wings [5]. Fraenkel further proposed the theory that the halteres were inertial sensors, a theory which was subsequently elaborated on by Pringle in 1948 [5], [14]. Brauns (1939) is also reported to have established a correlation between the development of the halteres and the flight capability of species [15].

Pringle published one of the most important manuscripts regarding the function of halteres, providing sufficient evidence to convince the community of their role as inertial angular rate sensors to the present day [14]. Pringle not only addressed the kinematics of the haltere, but also observed the dynamics of haltere oscillation, studied the sensory physiology of the haltere, performed neurological experiments, and measured the influence of the haltere on flight of insects using flash photography. While this work was quite comprehensive it had its weaknesses. Primary among these was the lack of understanding of the importance of the non-orthogonality of the halteres for distinguishing between pitch and roll rates. Pringle came to the conclusion that the halteres were only used to

measure and stabilize yaw rate because a single haltere cannot distinguish between rate components in the horizontal plane (pitch and roll). This position was later recanted in a book on insect flight [16] based on observations by others of compensatory response of the wings and head to pitch and roll rate [17].

Two publications, one by Sandeman alone and a slightly earlier one by Sandeman and Markl looked at compensatory responses of the wings and the head to forces on the haltere [18], [19]. These papers appeared to start off with the misconception that the gyroscopic forces that influence the haltere are due to body angular acceleration and the resistance of the haltere mass to the body's angular acceleration. This partial understanding of the forces influencing the haltere led to experimental setups that confirmed the influence of yaw angular acceleration on the haltere, but ignored the impact of Coriolis forces that are proportional to the body's angular rate. These authors found that the haltere expresses an electrical potential only when the haltere is forced rapidly forward. They deduced from their results that the haltere is used during rapid maneuvers involving high accelerations for which the flies visual input is disrupted. This conclusion appears to completely ignore the general instability of flies after haltere ablation. This result was superseded by subsequent work where head stabilization was correlated with roll rate which is at least in part inferred from the halteres [3], [20]–[22]. The work by Sandeman [18], [19], which included tracing of the neurological pathways of the haltere did add significantely to understanding of the ipsa- and contralateral pathways of the haltere.

Nalbach published a number of papers related to the mechanosensory function of the halteres [23]–[25]. The first of these papers looked at the relative magnitudes of the forces acting on the haltere, concluding the Coriolis forces were predominant and that some of the conclusions of Sandeman were not well founded. The second of these papers demonstrated experimentally that the haltere of a fly is insensitive to the component of the rate vector perpendicular to the plane of motion of the haltere. The

fact that the insect could not distinguish between roll and pitch with a single haltere was experimentally demonstrated.

A number of other significant findings have occurred that may expand on the general theory of haltere functionality. In a detailed study of the haltere hinge physiology, Chan, et al. [26], discovered that there are 11 control muscles associated with the haltere, two of which receive strong activation from directionally sensitive visual interneurons. This discovery opens up the possibility that certain flight reflexes may be induced through manipulation of the haltere in a feedforward manner. Heide discovered that the first basalar motor neuron (mnb1) controlling wing kinematics receives a phasic once per cycle impulse from the halteres regardless of insect motion during flight [27]. This discovery may lend some credibility to the proposition by von Buddenbrock that the halteres act to nervously stimulate the wing motion. Heide's finding has led to some current debate over the interpretation of previous flight instability results. Fayazzudin and Dickinson found that the connection between the haltere and mnb1 consists of both a fast electrical monosynaptic impulse and a slow chemical synapse that attenuates at high frequency [28]. Their proposed model of the phasic stimulus from the haltere was that it had no effect on flight control if there were not Coriolis forces acting on the haltere.

2.2 Sensory Physiology

Pflugstaedt documented the arrangement of the sensilla and showed that the sensilla of the basal plate at the base of the haltere are oriented diagonal to the length of the haltere [29]. Figure 2-1, taken from Hengstenberg [3], shows the general configuration of sensilla at the base of the haltere. Gnatzy assessed the topology of the campaniform sensilla on the body of *Calliphora* [30]. Hengenstenberg [3] summarized current knowledge including sensory hairs and chordotonal organs as follows:

> The haltere knob carries about 13 innervated hairs, the haltere base contains 2 chordotonal organs and cs. 340 campaniform sensilla, arranged in 5 distinct fields. The haltere nerve contains 370-380 sensory fibres, allowing for 20-30 fibres to be attributed to the chordotonal organs. Compared to the wing,

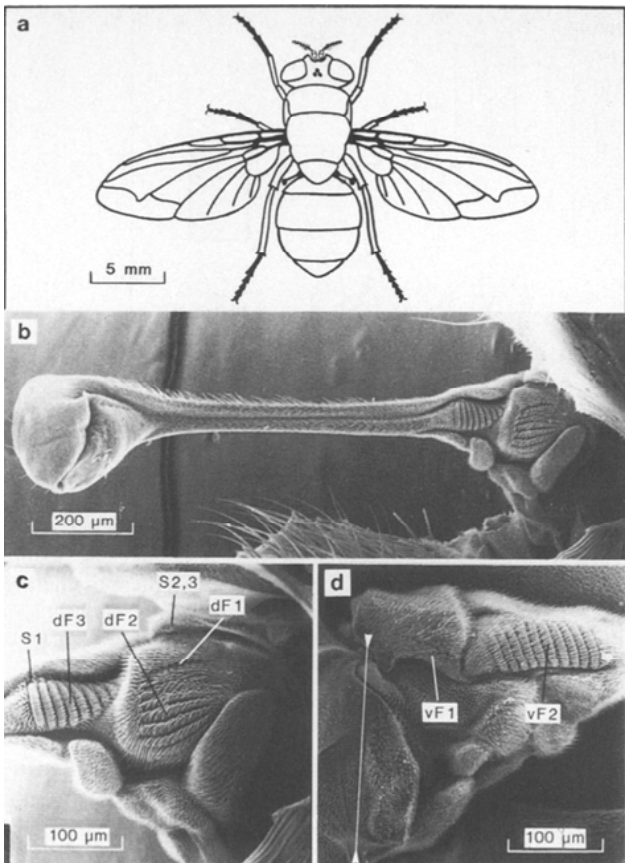

Figure 2-1. General morphology of the haltere on *Calliphora*. Taken from Hengstenberg [3].

> halteres have about the same number of mechanoreceptors, but the type distribution is significantly different.

In the assessment of Pringle, the campaniform sensilla are typically elongated and are sensitive to compression in the elongated direction [31]. Pringle later gave a detailed description of the sensors on haltere [14]. In addition to campaniform sensilla, the halteres have chordotonal organs that act as stretch sensors, sensitive in tension. Pringle determined that the campaniforms of the dorsal basal field (dF2) along with the large chordotonal organ are oriented at roughly 45 degrees relative to the haltere stalk, making them preferential for measuring bending strains. However, Hengstenberg [3] reported, based on the experimental studies of Thurm et al. [32] and Stedtler [33], that the different fields do have preferred directions of sensitivity, but the directions are not always as expected. The ventral scapal field (vF2) responds in the rostral-ventral direction, the

dorsal scapal field (dF3) responds in the rostral-dorsal direction, and both the basal field (dF2) and the Hicks' papilla (vF1) respond in the caudal direction. The implication is that all of these fields are to some degree sensitive to haltere out of plane deflection typical of Coriolis force. The implications of the potential sensitivity of these other fields to body rate induced forces are not yet clear.

Zill [34], while studying the cochroach, *Periplenata*, demonstrated that the campaniform sensilla are actually sensitive to tension along the long axis of the cap of the sensilla. This is in direct opposition to the deduction of Pringle [31]. Note, however, that Pringle was very careful to explain in his paper that his reasoning was based on circumstantial evidence. In the work described in this dissertation, the assumption that the campaniforms respond in tension is applied to the models of the sensory field.

Dickinson's manuscript on the encoding properties of wing campaniforms suggests with caution that the wing campaniforms could not function efficiently as magnitude detectors [35]. He suggests that the campaniforms will saturate at low power and remain nearly constant with increasing stimulus strength. Beyond a certain threshold the campaniform neurone will record only one event during each wingbeat, therefore acting as a "one-shot" detector. Increases in stimulus strength are assumed to recruit more campaniform neurones as opposed to increasing the output of an individual neurone. Other insects such as locusts having much slower wing beat frequencies have campaniforms that are similar but do act as magnitude detectors, firing cyclic bursts of action potentials during each cycle whose frequency depends on magnitude of wing torsion. Since the halteres have evolutionary traceability to the wings, the campaniforms on the halteres are probably also one-shot detectors firing once per cycle and recruiting more sensilla as the strain increases.

Elson, working on the locust (*Schistocerca gregaria*) hind wing sensilla, determined that supination or twisting of the wing caused a clear response, with the involved sensilla spiking at raised frequency [36], [37]. Increasing the amplitude of supination raised the

rate of spiking in a static sense and increased spike size through progressively recruiting additional sensilla. The velocity of twisting appeared to have little impact. The results imply that, as a group, the campaniform sensilla give a directionally-sensitive measure of the magnitude, but not the rate of change, of wing deformations. Elson reported, in agreement with Zill [34] that directional sensitivity is associated with the elliptical shape of the cuticular cap of the sensillum, compression perpendicular to, or tension in parallel to, the longitudinal axis of the cap excite the sensillum. The sensillum on the locust wing were shown to respond to dorsal or anterior bending of the wing and to axial stretching, consistent with the receptors location. The sensilla were ventral and posterior on the wing vein and the orientation was more nearly longitudinal than transverse relative to the vein.

As stated previously, little has been determined by the cited authors with regard to the way that the angular rates are encoded by the fields of sensors in the haltere base. An area that is particularly lacking in the literature is the role of the chordotonal organs, if they have one, in the encoding of angular rates.

2.3 Neural Pathways

For a fly to distinguish between pitch and roll (or any other two components of angular rate in the plane containing the two mid-stroke positions of the halteres), the haltere stroke planes must not be coincident and there must be some form of bilateral combination of signals from the two halteres. As described in Chapter 3 there are a number of ways to do this that do not involve contralateral transmission of nervous response, but whether or not contralateral pathways exist has continued to be of interest to researchers in order to understand how the wings and head are controlled.

Pringle measured the response of the haltere nerve to a variety of stimulus at the haltere, distinguishing the responses due to in-plane and lateral forces on the haltere [14]. It was not until later that investigators traced the pathways through the thoracic ganglion. Sandeman and Markl [18] produced Figure 2-2 which shows the result of preparations of cobalt choride after infiltration through the haltere nerve. The result showed that the

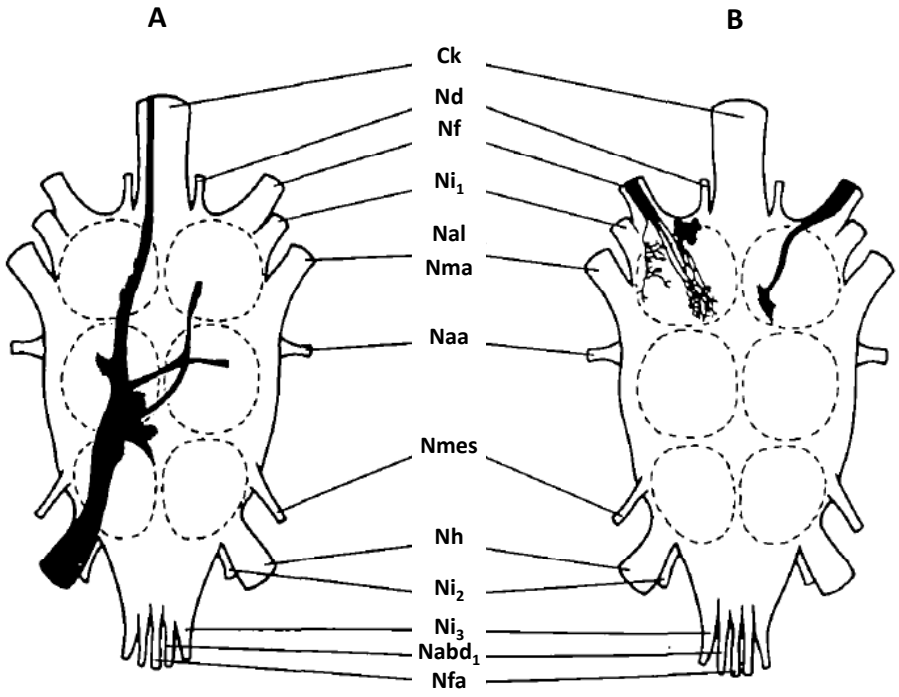

Figure 2-2. Diagram taken from Sandeman and Markl (1980). The central projections of the haltere nerve (A), neck motoneurones and prosternal organ sensilla (B). Ck, neck connectives; Nd, dorsal prothoracic nerve; Nf, frontal prothoracic nerve; Ni_1, Ni_2, Ni_3, pro-, meso- and metathoracic leg nerves; NaI, Nma, Naa wing nerves; Nmes, lateral mesothoracic nerve; Nh, haltere nerves; $Nabd_1$, Nfa, abdominal nerves (terminology anglicized from Vater, 1962).

haltere extends through the ganglion to the brain which can be at least partially explained given Chan's [26] finding of visual inputs into two of the haltere control muscles. The nerve is also shown to project into neuropiles on both the ipsi- and contralateral sides of the ganglion. While stimulating the halteres, Sandeman and Markl recorded only ipsilateral response in the wing nerves. Similar measurements in the neck nerves showed both ipsi- and contralateral responses from a single haltere with the larger response being on the ipsilateral side [18].

The central projection of the haltere fields is not particular to a specific field in general, according to Chan and Dickinson based on studies of *Calliphora vicina* [1]. The projection in some instances is common to multiple sensor fields as well as the serially

homologous fields on the radial vein of the wing. While the specific cellular targets of the haltere sensory cells were not determined, the afferents of dF2 were observed to make contact with at least one wing steering motoneuron (mnb1) that is known to be important in turning maneuvers. Projections from different regions of the same field were shown to vary. The mid-row sensilla of the most anterior and posterior rows of dF2 were observed to project contralaterally. At the mid-mesothorax, the afferents of dF2 in particular were seen to terminate in a calyx-like structure that surrounds an ascending neurite of mnb1.

Fayazzudin and Dickinson [28] showed a connection between dF2 and mnb1. To demonstrate this, the different fields of campaniforms were systematically disabled. Only dF2 was seen to have a significant impact on the b1 motor neuron. The compound potential was observe to include a fast electrical response with a synaptic latency of ˜200 microseconds and a slow chemical component which drops off at frequencies above 10 Hz. The b1 muscle has typically been shown to respond within 3-4 msec [38]. The wing stroke period for the insect being studied was 6-7 msec. The b1 muscle has been shown by a number of authors to fire a single spike during a narrow phase band during each wing stroke [27], [39], [40]. This acts tonically to reconfigure the wing hinge and through small changes in the phasing of the signal the wing downstroke trajectory is modified. Advances in phase were shown to increase the stroke amplitude and cause the adduction (pull closer to the body) of the wing during downstroke. Fayazzudin and Dickinson also note that mnb1 receives phasic inputs from wing campaniforms and these are critical to their model of overall control of the b1 muscle.

2.4 Wing and Neck Mechanosensory Control Observations

Typically wing control has been described in terms of a number of distinct responses, beat frequency, wing twist (pronation and supination), wing outboard angle (abduction and adduction), stroke amplitude, and wing deformation. In his definitive book, “Insect Flight,” Pringle describes a wing trajectory which indicates that the downstroke is associated more with lift generation and the upstroke is more tightly associated with

thrust [16]. The head is free to move in three angular degrees of freedom, approximately +/- 20 degrees in pitch and yaw in *Calliphora* and +/- 90 degrees in roll [20]. Both the wings and the head are controlled through a number of inputs besides the perception of egomotion with the halteres, e.g., visual, wind speed, wing loading, proprioception. In fact, Hengstenberg describes 8 distinct inputs to head roll control, including 4 distinct visual cues along with self motion, wing load, gravity, and head posture [22]. Many researchers have studied insect motor control, and this section is only intended to give a general overview of functions associated with haltere mechanosensory function.

2.4.1 Wing Compensatory Response

As mentioned previously, Pringle recognized that "beyond doubt" the halteres affect a reflex response in all three rotational axes [16]. His conclusion was based on the work of both Hollick [41] and Faust [17]. Pringle documented that blinding had a significant but not total effect on the reaction to a roll disturbance. Blinding had little effect on the reflex response to rotations around yaw and pitch. The reflex responses were specifically described in terms of pronation and supination of the wings during downstroke and upstroke. Extirpation of the halteres eliminated the reactions, indicating the reactions were predominantly mediated by the haltere. Pringle proposed that the near normal flight of a fly with a single haltere was adequately explained by the fact that roll rate measurement is greatly supplemented by visual measurement and yaw rate is redundantly measured by both halteres. The absence of distinct pitch rate measurement from the halteres was not sufficient to destabilize the fly.

Heide published a comprehensive report on wing motor control [27]. This report is referenced extensively in part due to the description of a phasic signal that impacts the basalar wing control muscle (B1) even in quiescent flight. Heide summarized, "In non-rotating flies haltere afferences are involved in the timing of output impulses supplying steering muscles. In addition, in rotating flies haltere afferences gate the output to steering muscles." A number of observations from this document that may be significant to the

haltere's mode of influence on the flight control process. In the cited report, Heide noted that although the steering muscles mainly have a "tonic" effect on the wings they are, nonetheless, muscles that contract rather fast. The muscles were shown to respond slight even to stimulation as fast as the wing beat frequency. He concluded that the phasing of the steering muscle spikes may be important to fine steering control because of the ability to respond so quickly. Experiments on blinded flies on a rotating turntable showed that the muscles M.III1 fire during yaw turns toward the ipsilateral side, indicating the fly attempts to compensate for the rotation. The muscles M.I1 are activated during turns to the contralateral side. Further, it was found that bending the antennae back as if in a strong head wind resulted in increased activation of the muscles. This increase in nerve spike seems to be accompanied by a decrease in wingbeat amplitude. With ablated halteres the described responses disappear.

Dickinson documented experiments with the purpose of characterizing the haltere mediated changes in stroke amplitude and frequency induced by imposed body rotation in *Drosophila* [42]. This test setup, like that of Hengstenberg, was able to rotate the visual field with the fly in order to isolate haltere induced responses. When pitched forward (head down), the flies increased both the stroke frequency and stroke amplitude of their two wings. Backward pitching motion elicited a decrease in amplitude and frequency. During functional rolls to the left and right, the flies increased the stroke amplitude of the wing on the side of the body that was rotating downward, and decreased the amplitude of the wing on the side that was rotating upward. In contrast to the pitch response, there was little modulation of stroke frequency during functional roll. One result of haltere ablation was that it significantly increased the background stroke frequency of the fly in the absence of any rotational stimuli. Ablation of one haltere only partially inhibited the equilibrium reflexes. While both the pitch and roll responses of the wing ipsilateral to the ablated haltere were diminished by 65%, the response of the contralateral wing was not significantly different from that of unablated control.

Balint and Dickinson found that, by correlating b1 and b2 spike occurrences with cycle-to-cycle changes in downstroke deviation, these two muscles could account for a large proportion of the observed variation in wing trajectory during visually induced steering reactions [43]. However, complex interactions between the steering muscles were seen to influence stroke parameters. For example, although b1 and b2 in summation contribute to downstroke deviation, in cases where neither were active there was still significant variation in deviation, probably due to the antagonistic b3 muscle. They speculated that reconfiguration of the wing hinge is involved in changing the "mode" of the wing stroke. These differences in mechanical advantage may explain the non-linear relationship between muscle activation and wing kinematics. In summary, they found that the role of any single muscle cannot be considered in temporal or spatial isolation either from its prior activity or from the action of other steering muscles.

Balint and Dickinson identified three independently controlled features of the wingbeat trajectory – downstroke deviation, dorsal amplitude and mode. Modulation of each of these kinematic features corresponded to both activity in a distinct steering muscle group and a distinct manipulation of the aerodynamic force vector [44]. Results suggest that it is the ability to manipulate the coupling among aerodynamically relevant kinematic parameters, rather than the ability to control these parameters independently, that allows *Calliphora vicina* the flexibility of control observed in previous measurements of its directional force and moment output. It was found that the basalare muscles primarily controlled lift and roll by varying the downstroke force, the muscles of pteralae III and I controlled thrust and yaw by changing the upstroke force, and an unknown muscle group controlled lift and roll by varying the upstroke force inclination. Due to the dependence of moments on the instantaneous position of the wing, roll and yaw are most sensitive to forces at mid-stroke, whereas pitch is most sensitive to forces during stroke reversals. Although there is no evidence that flies can actively alter wing deformation,

especially during rotation when wing torsion is most pronounced [45], considerable wing deformation was observed through the duration of the upstroke.

Bender and Dickinson found that altering visual feedback had no significant effect on the dynamics of saccades, whereas increasing and decreasing the amount of haltere-mediated feedback through haltere modification decreased and increased saccade amplitude, respectively [46]. In other experiments, aerodynamic surface of the wings were altered such that the flies had to actively modify their wing-stroke kinematics to maintain straight flight on a magnetic tether. Flies exhibit such modification, but the control is compromised in the dark, indicating that the visual system does provide feedback for flight stability at lower angular velocities, to which the haltere system is less sensitive. Results suggest that the time course of the saccade is determined by a feed-forward motor program that is influenced, but not precisely structured, by mechanosensory feedback. Electrophysiological studies in rigidly tethered flies suggested that saccades are caused by changes in steering muscle activity, including a burst of action potentials in the second basalar muscle (b2) and a phase advance of the first basalar muscle (b1) [40]. The visual system has bandpass filter characteristics that largely suppress its response to rotations above 600°/s [21], [47]; however, the majority of the saccades Bender and Dickinson observed in the magnetically tethered preparation have peak velocities below this value, and experimental visual rotations were of a constant 500°/s [48].

2.4.2 Head Compensatory Response

Sandeman, as described earlier, experimentally stimulated halteres finding that if a rapid enough forward acceleration were applied to the haltere, the head would reflexively respond in a compensatory manner [19]. This was accompanied by differential "feathering" (supination or pronation) of the wings so a net yaw torque would be generated. Removal of the halteres eliminated both the head and wing responses. Additionally, Sandeman and Markl showed that the neck muscles phasically respond after a latency of only 2.5 to 3 msec and can follow the haltere stimulation up to a frequency of 200 Hz [18].

Measurements from the mesothoracic wing nerve showed two large units which respond with the same latency as the neck response.

Roland Hengstenberg focused primarily on roll compensation in his experimental investigations [3], [20]. The earlier of these manuscripts [20] gave a good summary of overall head response: *Calliphora erythrocephala* has the capability to actively control head position about all three body axes. Pitch and yaw turns are small (20°), while roll turns can be up to 90°. Flies produce compensatory head response while walking and flying, but not while stationary. Head responses have a latency of ˜5ms and can produce angular velocities of up to 1000°/s. The head compensation tends to undercompensate for disturbances. Simultaneously the body also compensates for disturbances. Hengstenberg proposed that the head and body likely work in concert to bring visual rate disturbances down to acceptable levels [3].

Hengstenberg found that mechanosensory roll control of the head in *Calliphora* depends on whether the insect is walking or flying [3]. When walking, the head orientation is influenced by gravity perception coming from mechanoreceptors in the legs. In flight *Calliphora* does not directly make use of gravity to control head orientation. When flying, mechanoreception influences control of only fast rotations. Virtually no mechanoreceptive response could be found at angular velocities below 50°/s. Above 50°/s the response increases to a maximum at approximately 1500°/s. Passive attitude stabilization and visual means of control are required to maintain an upright flight attitude and head orientation. A difference in aerodynamical load of the two wings, probably measured by sensilla at the wing base, also elicits a transient head roll partly compensating a banked attitude. Flies with one haltere removed could distinguish the direction of roll motion. It was earlier shown by Nalbach and Hengstenberg that using only one haltere, *Calliphora* can distinguish yaw from pitch, but not roll from pitch [25].

Nalbach and Hengstenberg studied the three-dimensional nature of compensatory reactions of the head to angular rate stimulus [25]. They observed that a fly responds

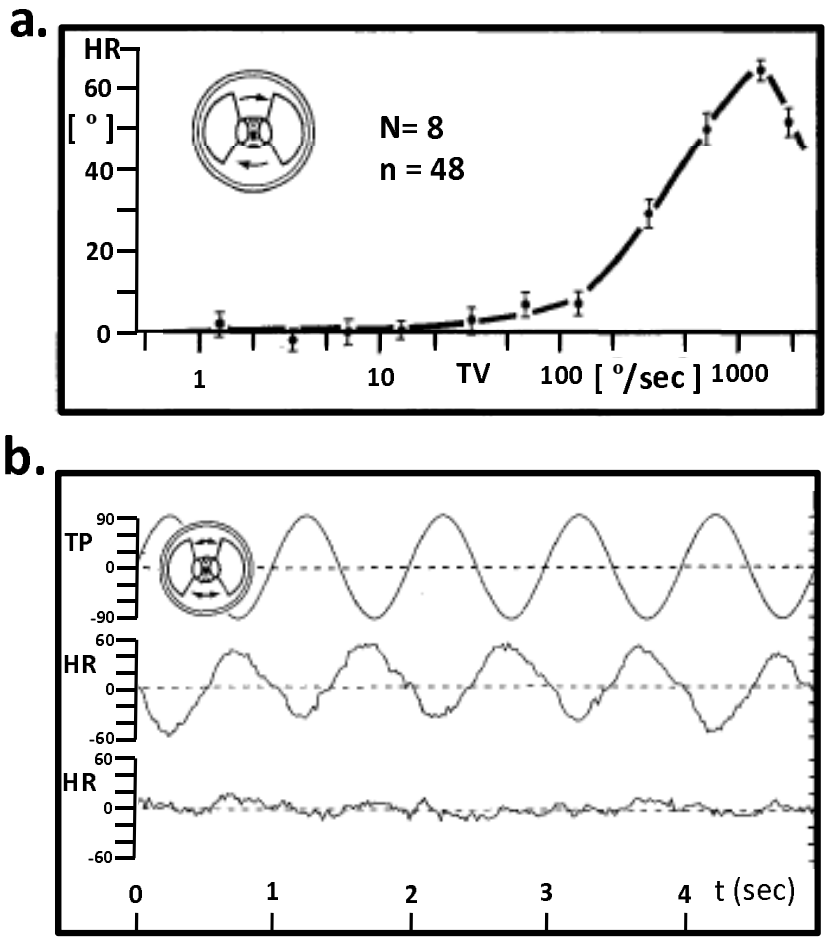

Figure 2-3. Figures from Hengstenberg (1988). a.) Magnitude of the reflexive roll response of the head in response to a input body roll rate. Direction was opposite direction of roll rate. b.) roll response with (middle) and without (bottom) halteres relative to the input body rate (top).

to a negative body roll disturbance with a positive roll and a negative body pitch results in a positive head pitch. However, in yaw there is a coupled reaction. A positive body yaw results in a negative head yaw that is accompanied by a positive head roll. Similarly, a positive head yaw reaction is accompanied by a negative head roll. The researchers simultaneously measured other body responses. Head yaw or roll reactions were accompanied by an asymmetry in wing beat amplitudes such that a compensatory

response would result. Both wing beat amplitude and frequency were found to increase synchronously. Head pitch reactions were accompanied by bilateral symmetrical variations of the lower turning point of the wing stroke and vertical abdomen movements. Changes in wing beat amplitude was found to be due to change in the lower forward extent of the stroke, creating a positive pitch moment when a negative disturbance was sensed.

CHAPTER 3
HALTERE KINEMATICS AND DYNAMICS

3.1 Introduction

The halteres of Diptera (Figure 3-1) are well established as organs necessary for flight stabilization. The mechanism by which the stabilization occurs was debated between the 18th and the first half of the 20th century, with some arguing that the haltere was a "stimulant" for flight motor function, others claiming the haltere functioned as an inertial balancing system, and still others claiming the halteres were a gyroscopic sensory mechanism [5], [13]. However, the work of Pringle provided a firm basis for viewing the haltere as a gyroscopic sensor, optimized for sensitivity to Coriolis forces [14]. The Coriolis force occurs when an object with mass and a finite velocity is constrained to move in a fixed path within a reference frame that is rotating. The Coriolis force is proportional to the reference frame rotation rate, so if through an appropriate strain sensor the force is measured, then a signal is available for rate damping in a stabilizing control loop. Pringle initially did not recognize the ability of the mechanical configuration of the halteres to distinguish between pitch (transverse axis) and roll (longitudinal axis) rotations and therefore assumed the use of the halteres was limited to yaw (vertical axis) rotations. This position was later recanted based on the findings of Faust that demonstrated stabilizing wing reflexes associated with pitch, yaw and roll in *Calliphora* [16], [17]. It was not until much later that Nalbach reviewed in detail the significance of all forces acting on the halteres and elaborated on the potential benefits of non-orthogonality of the haltere pair [23], [24]. A number of authors have demonstrated the compensatory reactions of the head and wings to independent components of the body rate vector, thereby demonstrating the role of halteres in both image stabilization and attitude control [17], [18], [20], [42], [46]. Heide performed extensive research associated with the haltere phase tuning of the first basalar motor neuron (mnb1) in control of wing kinematics [27].

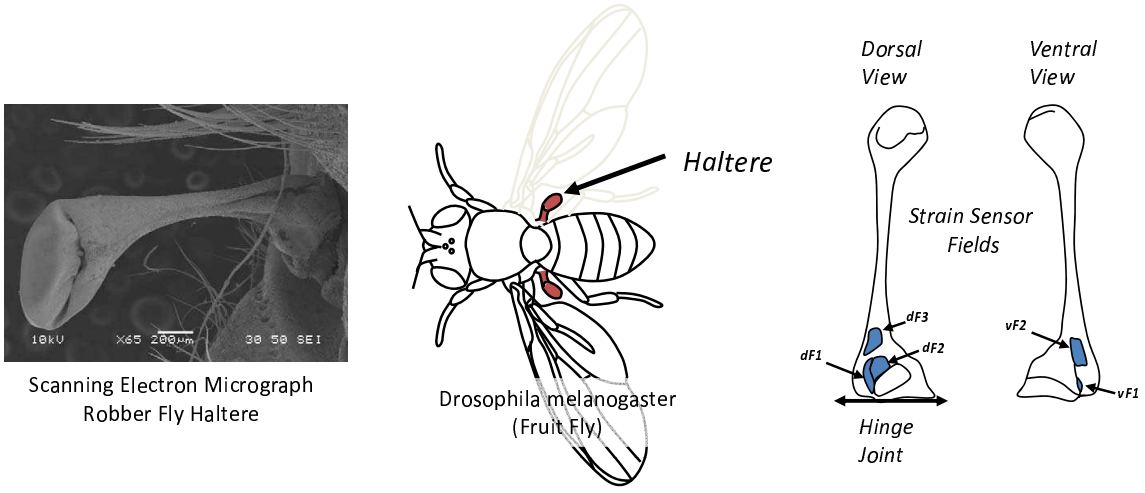

Figure 3-1. Characteristic locations of the halteres and their strain sensors. Fields of campaniform (# of sensilla): dF1: dorsal 'Hicks papillae' (17), dF2: dorsal basal plate (100) , dF3: dorsal scapal plate (110), vF1: ventral 'Hicks papillae' (10), vF2: ventral scapal plate (100). Not shown are the large and small chordotonal organs.

This was followed by a number of related studies of flight motor control, e.g., Tu and Dickinson [49], [50].

Pringle and Nalbach both recognized that each haltere, due to its large amplitude motion, is sensitive to two orthogonal rate components in its plane of motion, and, further, describe the distinct impacts of the vertical and horizontal rate components on the haltere [14], [23]. The vertical rate component, Ω_x in Figure 3-2, generates a force with twice the frequency content of the horizontal component. This knowledge has been the basis for the acceptance, with incomplete understanding, of the apparent ability of flies to distinguish between body rate components. Given the haltere specific rate components, variations of bilateral summing and differencing allow construction of signals proportional to components of the body rate vector in any body-fixed direction. Studies have demonstrated the location and activation of both ipsilateral and contralateral neural pathways between the halteres and the muscles of the wing and neck [18], [28], [51]. Further studies have demonstrated visual pathways to the halteres allowing speculation of

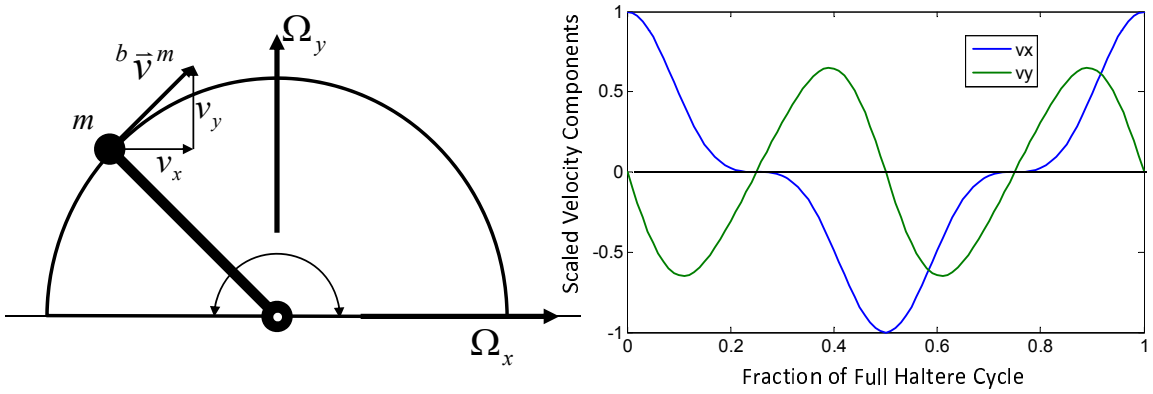

Figure 3-2. As the haltere beats back and forth the velocity component perpendicular to Ω_x changes sign at twice the frequency as the component perpendicular to Ω_y. This results in a Coriolis force with two distinct frequency components.

a feedforward process that introduces virtual rate "errors" into the control loop through the manipulation of a complex of muscles at the base of the haltere [26].

The objective of the current research is to use the techniques of engineering mechanics to analyze the haltere and thereby establish the fundamental quantities required for and mathematical limitations associated with reconstruction of body rate components. The only viable mechanism documented so far for decoupling of the two haltere rate components has been frequency demodulation [4]. In contrast to frequency demodulation, the methods of this chapter demonstrate the potential to use strain and strain rate encoded by the mechanoreceptors at the base of the haltere to measure the same two rate components. This measurement is possible due to the natural decoupling of the rate components at the center of the haltere stroke and the approximately linear nature of the governing equation of motion. An error analysis is also provided that illustrates how relative errors inherent in the measurement of all three body rate components can be inferred due to the nonlinearities in the equations of motion. These results have implications to interpretation of past experimental results and understanding of sensory structures associated with the halteres.

3.2 Methods

Previous work on haltere mediated reflexes describes the physical geometry of the fruit fly, *Drosophila melanogaster* [42]. This description of the geometry (Figure 3-3) is used as a starting point for the haltere analysis in this chapter. The predominant characteristics of the biological system used in the current development are the amplitude of the haltere stroke and the configuration of the halteres with respect to the mid-sagittal and transverse planes of the fly body. The halteres on *Drosophila* oscillate in a plane that is tilted back roughly thirty degrees toward the mid-sagittal plane. The line that defines the intersection of the haltere stroke plane with the sagittal plane is rotated toward the head by approximately twenty degrees so that at the top of its stroke the tip of the haltere is in a more anterior position than at the bottom of the stroke as shown in Figure 3-3. However, since the line of intersection of the haltere planes is, for convenience, used to define the body yaw axis $\hat{x}_3$, the value of this angle is arbitrary. For the purpose of this study the intersection of the haltere planes is assumed to be fixed relative to the body. The wing beat frequency, which was nominally 215 Hz in the data reported by Dickinson for *Drosophila*, varies significantly both within and between species [42]. For the sake of analytical convenience, a value of 200 Hz was used in simulations where general effects of out-of-plane stiffness and damping impact on the trajectory were simulated.

The equations of motion developed in this study are non-dimensional and describe the system in terms of its natural frequency and damping coefficient. The component of the haltere motion in the primary plane of oscillation is assumed to be deterministic and purely harmonic as observed in the body reference frame, oscillating through a range of +/-ninety degrees. Damping of out-of-plane motion is assumed to be proportional to the angular rate of the out-of-plane motion and the stiffness proportional to out-of-plane displacement. The source of stiffness is not specified, whether it is due to the resiliency of the haltere stalk or the joint and its associated musculature. The haltere model for out-of-plane motion can be considered as an equivalent mass at the radius of gyration of

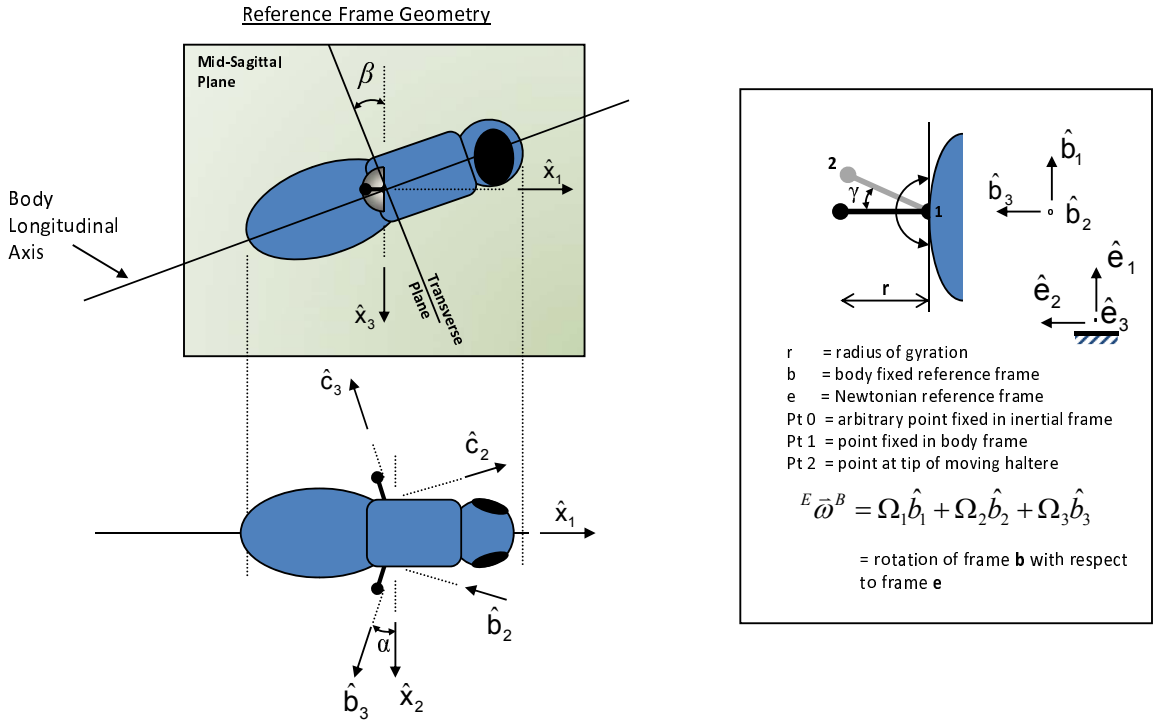

Figure 3-3. Reference frame definitions for the halteres, b and c, and frame x which defines the roll (x_1), pitch (x_2) and yaw (x_3) axis. The angle beta is arbitrary with this definition of reference frames.

the haltere on a rigid massless structure with a torsional spring and damper at the base. The actual dynamics and control of the haltere may be much more complex and is an area of ongoing research. Chan describes eight direct control muscles at the base of the haltere similar to the muscles at the base of the wing [26]. These muscles could possibly fine tune the kinematics of the haltere.

The equations of motion are generated without any small angle assumptions for the purpose of simulating the haltere trajectory under the influence of constant inertial body rates. Transients are not considered in this phase of the research and only the haltere response under the ideal conditions of constant angular rate were examined to draw preliminary conclusions about the fundamental limitations of the haltere or haltere pair. This steady-state assumption is equivalent to assuming that the body rates have

a significantly longer period than the period of haltere oscillation and any associated transients. Time varying rate components are used in the analysis in Chapter 4.

Finally, the component of angular rotation of the haltere in its primary plane is assumed to be sinusoidal. That is, the angular position γ of the haltere in its primary plane of motion is assumed to be

$$\gamma = \frac{\pi}{2}\sin(\omega t),$$

where ω is the constant beat frequency of the haltere. The actual profile has been observed to be closer to a saw-tooth pattern having a flatter angular velocity profile for the majority of the stroke and a quicker turn around at the ends [23]. The sinusoidal model provides an analytically simpler form that can be used to develop valid conclusions due to the similar symmetry of motion with respect to the center of the stroke.

3.3 Results

3.3.1 Kinematic Assessment

Insight regarding the forces acting in the out-of-plane direction can be examined by first assuming no out-of-plane haltere deflection. The right half of Figure 3-3 shows the right haltere and reference frame directions associated with the haltere and inertial space. In the following sections, hatted variables represent unit vectors that describe orthogonal directions for the required reference frames. Left superscripts describe which reference frame the vector quantity is observed within. Right superscripts identify the point or reference frame the quantity characterizes. Nomenclature is summarized in Table 3-1.

The body angular rate vector relative to the inertial frame, ${}^e\vec{\omega}^b = {}^e\ \vec{\omega}^x$, is represented in the right haltere reference frame as

$${}^e\vec{\omega}^b = \Omega_1\hat{b}_1 + \Omega_2\hat{b}_2 + \Omega_3\hat{b}_3. \tag{3–1}$$

Table 3-1. Notation associated with kinematic and dynamic expressions.

Symbol	Definition
γ	: haltere stroke angle
θ	: out of plane deflection angle
${}^a\vec{\omega}^b$	: angular rate vector of reference frame "b" with respect to frame "a"
${}^a\vec{\alpha}^b$	: angular acceleration of reference frame "b" with respect to frame "a"
Ω_i	: angular rate components in the haltere reference frame
W_i	: angular rate components in the body reference frame
$\vec{P}_{12}$	: position vector from point 1 to point 2
${}^e\vec{v}^1$	: velocity vector of point 1 with respect to frame "e"
${}^e\vec{a}^1$	: acceleration vector of point 1 with respect to frame "e"
ζ	: critical damping ratio for out-of-plane motion
ω_n	: haltere out-of-plane natural frequency
ω_h	: haltere in-plane oscillation frequency
$\hat{b}_i$	: unit vectors defining the "b" reference frame
r	: haltere radius of gyration

In (3–1), Ω_i, are the angular velocity components and $\hat{b}_i$ are the body fixed unit vectors as shown in Figure 3-3. The position, velocity and acceleration of a point mass at the radius of gyration of the haltere are found through successive differentiation to be

$$\vec{P}_{02} = \vec{P}_{01} + \vec{P}_{12} \tag{3–2}$$

$${}^e\vec{v}^2 = {}^e\vec{v}^1 + {}^b\vec{v}^2 + {}^e\vec{\omega}^b \times \vec{P}_{12} \tag{3–3}$$

$${}^e\vec{a}^2 = {}^e\vec{a}^1 + {}^b\vec{a}^2 + 2({}^e\vec{\omega}^b \times {}^b\vec{v}^2) + {}^e\vec{\omega}^b \times ({}^e\vec{\omega}^b \times \vec{P}_{12}) + {}^e\vec{\alpha}^b \times \vec{P}_{12}. \tag{3–4}$$

In these expressions, 0, 1, and 2 refer to an arbitrary point fixed in inertial space, a point at the base of the haltere, and a point at the radius of gyration of the haltere, respectively. The first acceleration term, ${}^e\vec{a}^1$, which is the acceleration of the base of the haltere with respect to the inertial frame is assumed to be small. The second term, ${}^b\vec{a}^2$ which represents acceleration of the haltere mass as observed from the body, is entirely in the plane of the haltere. Nalbach showed that these primary accelerations in the plane-of-motion are much higher than contributions associated with the body angular rates, and therefore, useful information pertaining to the body rates is unlikely to be

ascertained from in-plane force measurements [23]. The last term, ${}^e\overrightarrow{\alpha}^b \times \vec{P}_{12}$, which involves the angular acceleration of the body, was also shown by Nalbach to be a factor of 5 or more less than the third (Coriolis) term for sinusoidal body oscillations under 50 Hz. The remaining two terms after taking the appropriate vector products are

$$\begin{aligned} 2({}^e\overrightarrow{\omega}^b \times^b \overrightarrow{v}^2) &= 2r\dot{\gamma}[-\Omega_2 \sin(\gamma)\hat{b}_1 \qquad (3\text{–}5) \\ &\quad +(\Omega_1 \sin(\gamma) + \Omega_3 \cos(\gamma))\hat{b}_2 - \Omega_2 \cos(\gamma)\hat{b}_3] \\ {}^e\overrightarrow{\omega}^b \times ({}^e\overrightarrow{\omega}^b \times \vec{P}_{12}) &= r[(-\Omega_2^2 \sin(\gamma) - \Omega_3^2 \sin(\gamma) + \Omega_1\Omega_2 \cos(\gamma))\hat{b}_1 \qquad (3\text{–}6) \\ &\quad +(\Omega_1\Omega_2 \sin(\gamma) + \Omega_2\Omega_3 \cos(\gamma))\hat{b}_2 + \\ &\quad (\Omega_1\Omega_3 \sin(\gamma) - \Omega_1^2 \cos(\gamma) - \Omega_2^2 \cos(\gamma))\hat{b}_3]. \end{aligned}$$

The expression in (3–5) is the Coriolis term which generates out-of-plane ($\hat{b}_2$) force components associated with the in-plane body rates. These components are proportional to $2\dot{\gamma}\Omega_1$ and $2\dot{\gamma}\Omega_3$. The other components represent an in-plane acceleration directed along the stalk of the haltere proportional to Ω_2. The expression in (3–6) describing the centripetal accelerations, also generates out-of-plane forces on the haltere proportional to $\Omega_1\Omega_2$ and $\Omega_2\Omega_3$. The relative magnitudes of $\dot{\gamma}$ and Ω_2 will determine the significance of these centripetal terms. Errors introduced by these terms are quantified subsequently.
If the centripetal terms are small, the out-of-plane force on the haltere should be predominantly due to the Coriolis term and therefore will be associated with the body rate components that are in the primary plane of the haltere motion. An assumption of (3–5) and (3–6) is that the haltere is infinitely rigid and does not deflect out-of-plane. This assumption is the basis for the previous kinematic analysis of the haltere by Pringle and Nalbach and is useful for developing intuition regarding the predominant forces that impact the problem. In the following section, this assumption is eliminated to simulate the out-of-plane motion, or equivalently the strains resulting from that motion.

If the halteres are assumed to measure forces associated with the Coriolis accelerations, the measured signals should be proportional to the in-plane body rate components, Ω_1 and Ω_3 , as shown in (3–5). If two halteres that are initially in a common plane are rotated out of the plane by an angle α as shown in Figure 3-3, then all three components of the body inertial rate vector can be reconstructed. The body rate vector represented in the body-fixed roll, pitch, yaw frame is

$$ {}^e\vec{\omega}^x = W_1\hat{x}_1 + W_2\hat{x}_2 + W_3\hat{x}_3, \tag{3–7} $$

where (W_1, W_2, W_3) are the body roll, pitch, and yaw rates, respectively.

The relationships between the components of the body rate vector represented in the body roll, pitch, yaw frame and the components represented in the right haltere frame $\hat{b}$ and the left haltere frame $\hat{c}$ are

$$ \begin{aligned} {}^e\vec{\omega}^x &= \Omega_{b1}\hat{b}_1 + \Omega_{b2}\hat{b}_2 + \Omega_{b3}\hat{b}_3 \qquad (3–8) \\ &= \Omega_{c1}\hat{c}_1 + \Omega_{c2}\hat{c}_2 + \Omega_{c3}\hat{c}_3 \end{aligned} $$

$$ W_1 = -\frac{\Omega_{b3} + \Omega_{c3}}{2\sin(\alpha)} \tag{3–9} $$

$$ W_2 = \frac{\Omega_{b3} - \Omega_{c3}}{2\cos(\alpha)} \tag{3–10} $$

$$ W_3 = -\frac{\Omega_{b1} + \Omega_{c1}}{2} = -\Omega_{b1} = -\Omega_{c1}. \tag{3–11} $$

The importance of these transformations is that they allow a direct calculation of rate components along the body roll, pitch, and yaw axes, W_1, W_2, and W_3, given the two rate components that are measurable in each of the haltere reference frames. The research on halteres by Pringle did not recognize the ability of the insect physiology to combine the output of two halteres and thereby distinguish between pitch and roll components of the body rate vector [14]. Pringle initially assumed that the halteres

represented a redundant means of measuring yaw rate. Later experimental results by Faust demonstrated the ability of flies to react independently to each of the body rates [17]. Nalbach also published an article that experimentally demonstrated the bilateral combination of haltere measurements in *Calliphora* [24]. Therefore, within the neural architecture of dipteran insects there may be a basic representation of (3–9)-(3–11), although this does not rule out fusion of measurements from other sensors that support inertial stabilization.

3.3.2 Dynamics Equation Allowing for Out-of-Plane Motion

For the purpose of simulating the dynamics of the haltere, out-of-plane motion is considered. With the out-of-plane deflection angle defined as θ, summing moments associated with damping, stiffness, and inertial forces around the base of the haltere results in the following expression:

$$\begin{aligned}\ddot{\theta} + 2\zeta\omega_n\dot{\theta} + \omega_n^2\theta \;=\; & \dot{\Omega}_3\sin(\gamma) - \dot{\Omega}_1\cos(\gamma) - \dot{\gamma}^2\cos(\theta)\sin(\theta) \\ & +2\dot{\gamma}[(\Omega_3\cos(\gamma) + \Omega_1\sin(\gamma))\cos^2(\theta) - \Omega_2\cos(\theta)\sin(\theta)] \\ & +(\Omega_3^2\cos^2(\gamma) + \Omega_1^2\sin^2(\gamma) - \Omega_2^2)\cos(\theta)\sin(\theta) \\ & +(\Omega_2\Omega_3\cos(\gamma) + \Omega_1\Omega_2\sin(\gamma))\cos(2\theta) \\ & +2\Omega_1\Omega_3\cos(\theta)\sin(\theta)\cos(\gamma)\sin(\gamma).\end{aligned} \tag{3–12}$$

In (3–12), ζ is the damping ratio, and ω_n is the natural frequency that characterizes the out-of-plane stiffness and mass characteristics of the haltere. In this form, the haltere can be simulated by varying the out-of-plane natural frequency relative to the haltere beat frequency as well as varying the haltere damping characteristics. Again, the haltere stroke angle is assumed to vary with a simple characteristic motion $\gamma = \sin(\omega_h t)$, with the angular frequency of the haltere, $\omega_h = 200\ Hz$. The derivation of (3–12) is described in the appendix.

The relationship describing the single axis sensitivity of a micro-electro-mechanical (MEMS) vibrating structure gyroscope can be found through simplification of this expression [52]. For the case where both θ and γ are much less than 1, damping is small, $\omega_n^2 >> A^2\omega_h^2$, and $\omega_n^2 >> \omega_h^2$, (3–12) reduces to

$$\ddot{\theta} + \omega_n\theta = 2\Omega_3\dot{\gamma} = 2\Omega_3 A\omega_h \cos(\omega_h t).$$

The forced solution of this equation,

$$\theta = 2\Omega_3 A\omega_h \cos(\omega_h t)/\omega_n^2,$$

is the solution for the out-of-plane displacement of the MEMS gyro mechanism.

3.3.3 Haltere Trajectory Simulations

Simulations of the developed equation of motion were executed for a variety of cases with variations in the damping ratio and out-of-plane stiffness. The intent was to determine the characteristics of the displacement trajectories and the impact of nonlinear coupling of out-of-plane rate components into the in-plane component measurements. All simulations were executed with constant body rates. For the purpose of generating the plots, the haltere motion was initiated with no out-of-plane displacement and the haltere was allowed to transiently respond to the forces resulting from input body rates. The simulation was executed for 40 oscillations, with the last 20 used for making the plots. Because the haltere reaches a steady state trajectory, the 20 oscillations overlap, appearing as one closed loop. The only cases in which the haltere did not reach steady state were when the out-of-plane natural frequency was significantly less than the haltere oscillation frequency, or for low damping. These plots are not shown since they represent very large out-of-plane motion for the assumed model, which would not be representative of the biological system.

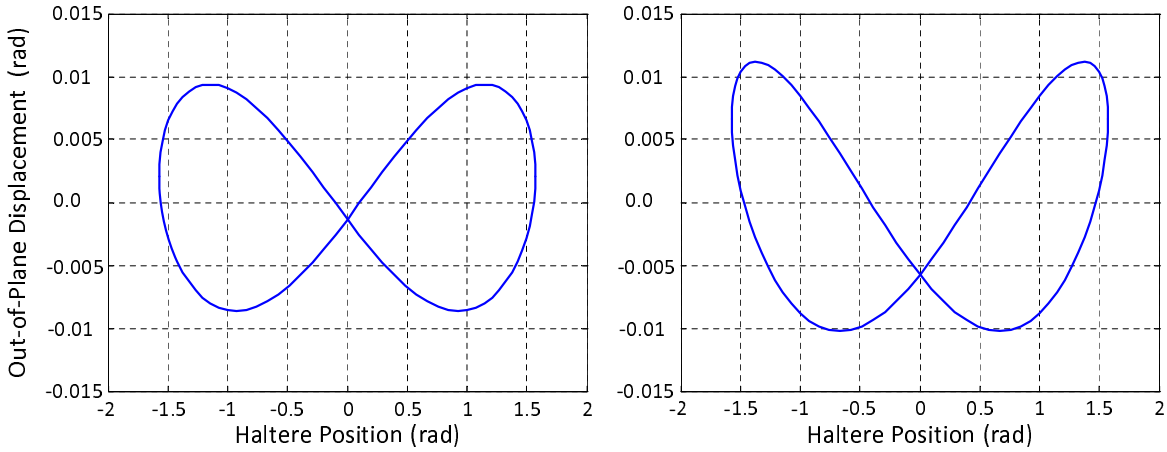

Figure 3-4. Haltere trajectories for $\omega_n = 200\ Hz$ (left) and $\omega_n = 400\ Hz$ (right). Haltere beat frequency, $\omega_h = 200\ Hz$. Input conditions Ω_1=10 rad/s, Ω_2=Ω_3=0 and ζ=0.1.

3.3.3.1 Out-of-Plane Stiffness Variations

Figure 3-4 and Figure 3-5 show the trajectories associated with a haltere out-of-plane natural frequency equal to and double the beat frequency of 200 Hz, respectively. The plots show out-of-plane displacement in radians as the ordinate, plotted against the stroke angle of the haltere as the abscissa. A haltere stroke angle of 0 has the haltere at the center of the stroke. The Ω_1 input generates the expected frequency doubled signal as the haltere sweeps through a semi-circular arc causing the velocity component perpendicular to Ω_1 to change sign twice, therefore the Coriolis force changes sign twice. The haltere velocity perpendicular to Ω_3 only changes sign once, giving no frequency doubling effect. The angular displacements peak at approximately half a degree for the conditions shown. When the natural frequency is significantly below 200 Hz, the out-of-plane motion is driven to very large angles and never reaches a steady state pattern.

3.3.3.2 Damping Variations

Examples of damping variations are shown in Figure 3-6 for the case of $\omega_n = 200\ Hz$ and input body rates of $\Omega_1 = \Omega_3 = 10\ rad/s$. These plots demonstrate the significant impact that damping variations, whether passively or actively induced, can have on the

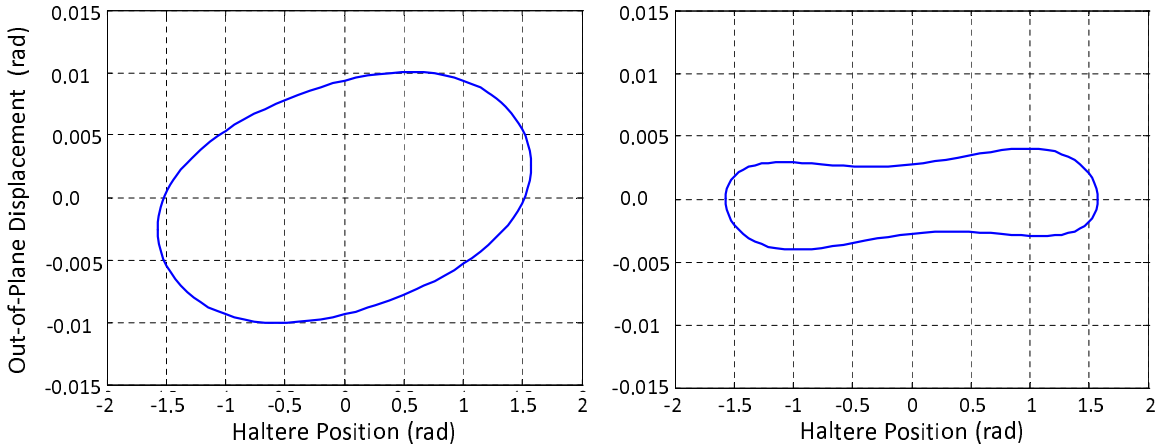

Figure 3-5. Haltere trajectories for $\omega_n = 200\ Hz$ (left) and $\omega_n = 400\ Hz$ (right). Haltere beat frequency, $\omega_h = 200\ Hz$. Input conditions Ω_3=10 rad/s, Ω_1=Ω_2=0 and ζ=0.1.

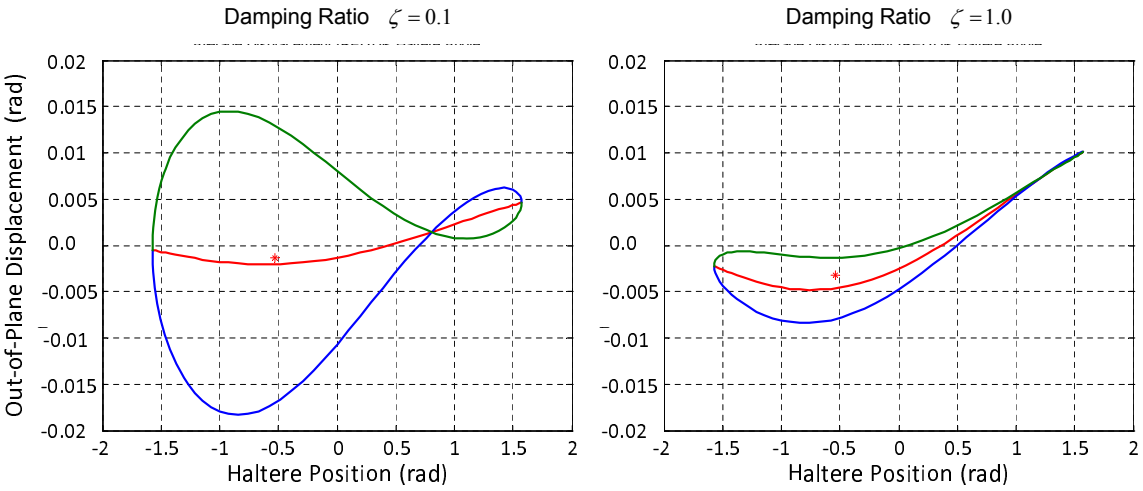

Figure 3-6. Haltere trajectories with damping ratios at 10% of critical (left) and 100% critical (right) for body rate inputs of $\Omega_1 = \Omega_3$=10 rad/s. Plots are bisected by the average displacement curve as a function of haltere position.

haltere trajectory. At low damping levels, $\zeta \approx 0.01$, the trajectory never reached steady state within the forty oscillation (0.2 second) simulation time (data not shown).

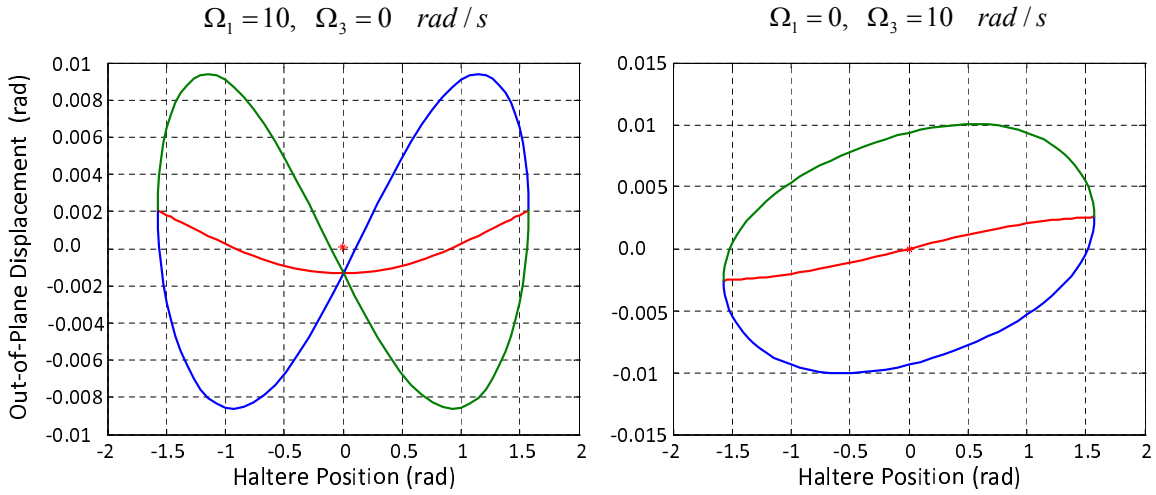

Figure 3-7. Haltere trajectories for $\Omega_1 = 10$ rad/s (left) and $\Omega_3 = 10$ rad/s (right) with the average displacement plotted as a function of stroke angle.

3.3.4 Average Haltere Position

The haltere displacement averaged with respect to haltere stroke angle is also shown in Figure 3-6. However, when the average displacement is plotted separately for the two rate components as in Figure 3-7, an interesting characteristic emerges that may provide insight into a possible mechanism by which the body rates are decoupled by the insect.

Figure 3-7 demonstrates a natural decoupling of the body rate components at the center of the haltere stroke. At $\gamma = 0$, the averaged magnitude of the response driven by Ω_3 is zero and the averaged slope of the response driven by Ω_1 is zero. If the governing differential equation (3–12) that describes the motion of the haltere is approximately linear, then the final trajectory of the haltere would simply be the superposition of the response of the two plots shown. Also, each of these plots would scale in proportion to the magnitude of the associated body rate since the Coriolis forces driving the motion are proportional to the respective body rates. Therefore, by measuring the slope and the magnitude of the response near the peak of the haltere trajectory, and having tuned in the appropriate proportionality constants, the body rate components in the plane of

the haltere motion could be directly obtained. These observations suggest the following hypotheses:

1. A system with halteres invokes a response proportional to the magnitude of the averaged strain at the center of the haltere stroke and takes advantage of the approximate linearity of the haltere dynamics to estimate Ω_1 (i.e. Ω_1 is proportional to the averaged magnitude of the strain at the middle of the stroke).

2. A system with halteres invokes a response proportional to the magnitude of the averaged strain rate at the center of the haltere stroke and takes advantage of the approximate linearity of the haltere dynamics to estimate Ω_3 (i.e. Ω_3 is proportional to the averaged magnitude of the strain rate at the middle of the stroke).

Note that the term strain rate can refer to two quantities that are proportionally related at the center of the haltere stroke. Because the angular acceleration of the stroke is approximately zero at the middle of the stroke, the strain rate is proportional to the spatial derivative of strain (ε) with respect haltere position (γ). That is,

$$\frac{d\varepsilon}{dt} = \frac{d\varepsilon}{d\gamma}\frac{d\gamma}{dt} = Const \cdot sgn(\frac{d\gamma}{dt})\frac{d\varepsilon}{d\gamma}.$$

Measurements by Pringle gave indication that the nerve afferents at the end of the stroke may be overwhelmed by signals associated with haltere motion reversal [14]. This would support the supposition that the sensory response of the haltere toward the middle of the stroke is of primary use by insects. The proposed method of determining the body rates is more direct than that patented by Wu and Wood [4]. In their patent, the fundamental frequency doubling is taken advantage of through a demodulation scheme to separate the two signals and determine the driving forces. The method proposed here may be directly realizable using discrete measurements, although it remains to be proven that the fields of strain mechanoreceptors (campaniform sensilla) existing at the base of the haltere encode quantities proportional to both strain and strain rate.

The described mechanism for measuring the body rates requires three characteristics of (3–12).

1. Linearity

2. Minimal dependence on the out-of-plane body rate Ω_2

3. Two independent forcing functions proportional to the in-plane body rate components Ω_1 and Ω_3

If these characteristics are met, the response to the two in-plane body rate components is uncoupled and the two independent responses are linearly proportional to the magnitudes of the respective body rates. By making various approximations associated with small displacement angles and the magnitudes of the various coupling terms, (3–12) can be reduced to a form that expresses the desired characteristics,

$$\ddot{\theta} + 2\zeta\omega_n\dot{\theta} + (\omega_n^2 + \dot{\gamma}^2)\theta = 2\dot{\gamma}\Omega_3\cos(\gamma) + 2\dot{\gamma}\Omega_1\sin(\gamma). \tag{3–13}$$

If $\dot{\gamma}^2$ is further assumed to be small compared to ω_n^2 then a second form that satisfies the desired characteristics can be found,

$$\ddot{\theta} + 2\zeta\omega_n\dot{\theta} + \omega_n^2\theta = 2\dot{\gamma}\Omega_3\cos(\gamma) + 2\dot{\gamma}\Omega_1\sin(\gamma). \tag{3–14}$$

The second form, shown in (3–14), is intuitive since it is a simple spring-mass-damper driven by Coriolis forces.

An open question is whether either (3–13) or (3–14) are a valid approximation of the full non-linear equation. Comparative simulations were performed between (3–12), (3–13) and (3–14). The closeness of the two darker curves in Figure 3-8 demonstrate that the first form of the linear approximations in (3–13) is an accurate representation of the haltere response, unlike the results from (3–14) which are plotted in the lighter color. Since (3–13) is a good approximation, the natural decoupling of the trajectories is assumed to be a generally valid assumption.

3.3.5 Analysis of Errors Due to Non-Linearity

An error analysis was performed to demonstrate the limitations the non-linear and out-of-plane cross-coupling terms imposed on the linear approximation of (3–13). Simulations were executed over a full range of pitch and yaw body rates (i.e., $-20 \leq$

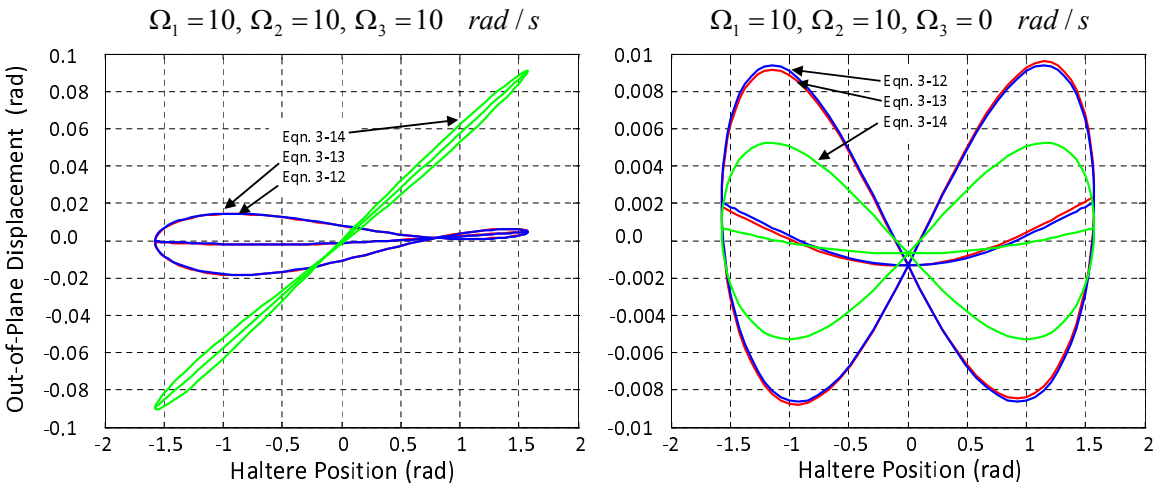

Figure 3-8. Comparison of the linear simplifications represented by Eq. 3–13 (red) and Eq. 3–14 (green) with the non-linear Eq. 3–12 (blue). Results are shown for two cases, $W = (W_1, W_2, W_3) = (10, 10, 10)$ on the left and $W = (10, 10, 0)$ on the right.

$W_2 \leq 20$ *and* $-20 \leq W_3 \leq 20$). Although Schilstra described a maximum angular rate of 2000 deg/s (34 rad/s) for *Calliphora vicina*, measurements included intentional saccadic maneuvers [53]. The lower rate used in these simulations (20 rad/s) is considered a sufficient maximum for rate errors incurred during typical stabilized flight. These rates were transformed into the reference frames for each of the halteres and then the dynamics for the haltere were simulated using the full nonlinear model in (3–12). Using best estimates of the strain rate and strain magnitude proportionality constants (i.e., constants found to give near zero error for an idealized linear model) the body rates in the haltere frames were estimated. The estimates from the two halteres were then combined using (3–9)-(3–11) to reconstruct an estimate for the roll, pitch and yaw rates in the body frame. Each plot represents errors associated with 1681 combinations (41*41) of yaw and pitch rate for a fixed roll rate. The error is the difference between the exact input body rates and the estimated body rates as demonstrated in Figure 3-9.

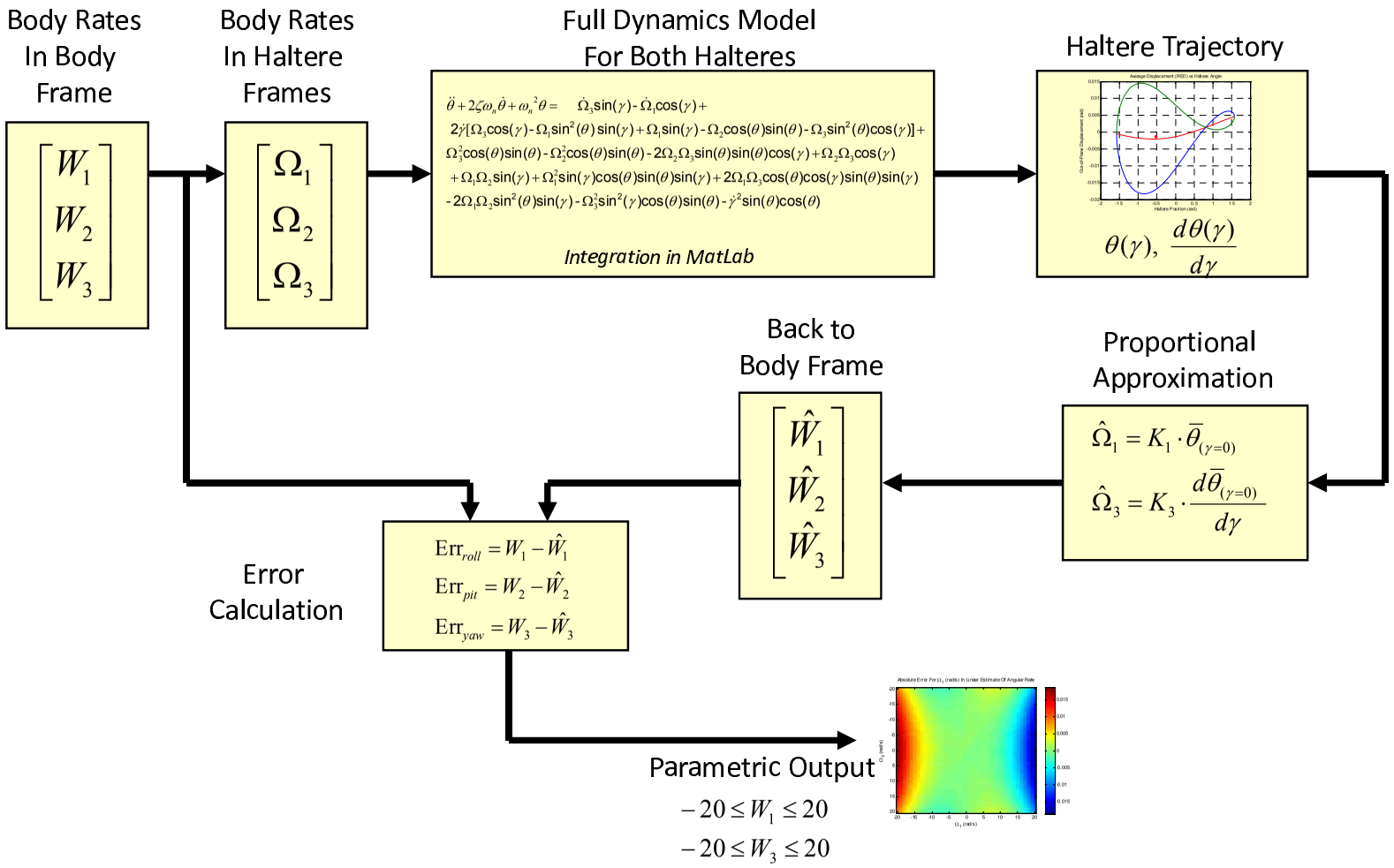

Figure 3-9. The Error Analysis compared the true rate components along the roll, pitch, and yaw body axis with those reconstructed using the proportional assumptions described in the text. Results are reported as absolute error in rad/s.

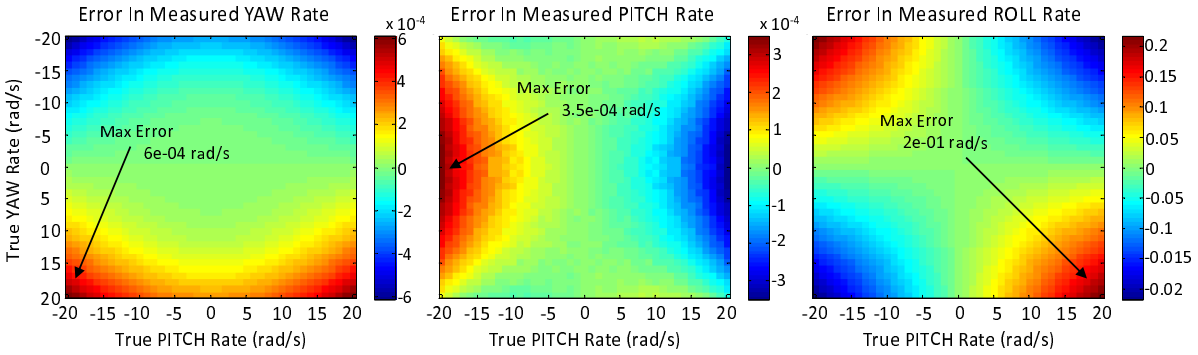

Figure 3-10. Error in estimates of rate components along the body Yaw, Pitch, and Roll axes for case Roll Rate =0. Conditions vary over a range of -20 to 20 rad/s for the true yaw and pitch rates. The color indicates the level of error as indicated on the color bar to the right of each plot.

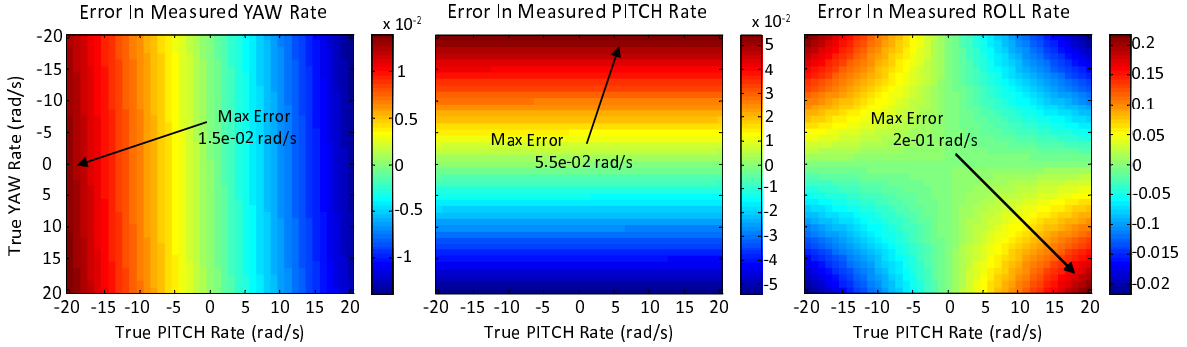

Figure 3-11. Error in estimates of rate components along the body Yaw, Pitch, and Roll axes for case Roll Rate =5 rad/s. Conditions vary over a range of -20 to 20 rad/s for the true yaw and pitch rates.

Figure 3-10 depicts the absolute errors for the pitch, yaw, and roll components of the body rates for the case of critical damping ($\zeta = 1$) and 400 Hz out-of-plane natural frequency. Figure 3-11 shows the errors for the case where the body roll rate is 5 rad/s.

The change in characteristics shown in Figure 3-11 can be explained by examining the governing equation of motion (3–12). The terms involving Ω_2, which is the out-of-plane rate component and the component most closely aligned with the body roll axis, are

summarized below after assuming a small out-of-plane displacement angle, θ

$$-2\dot{\gamma}\Omega_2\theta + \Omega_2^2\theta + \Omega_2\Omega_3\cos(\gamma) + \Omega_1\Omega_2\sin(\gamma). \tag{3–15}$$

Since θ is small, the last two terms in (3–15) will dominate. Note that $\cos(\gamma)$ will always be positive for all stroke angles, γ, and will be symmetric around $\gamma = 0$. Therefore, the term involving $\cos(\gamma)$ will influence the magnitude of the out-of-plane displacement at $\gamma = 0$ (i.e., the term will influence the yaw error). The term is also proportional to Ω_3, which is closely aligned with the body pitch axis. Therefore, roll coupling will introduce error in the yaw rate estimate that is proportional to the pitch rate. This linear relationship between yaw rate estimation error and pitch rate is exactly what is depicted in the left hand plot in Figure 3-11. Similar arguments, accounting for the influence of the $\sin(\gamma)$ function on the slope of the haltere out-of-plane motion at $\gamma = 0$ and the proportionality of pitch rate estimation error to the body yaw rate, Ω_2, can be made to explain the second plot in Figure 3-11. The similarity of the third plots in Figure 3-10 and Figure 3-11 indicate that the errors from the two halteres cancel, leaving the roll estimate error unaffected by roll rate.

3.4 Discussion

The intent of this chapter was to complement previous studies of halteres by performing a more rigorous analysis of mechanical response, establishing the potential mechanisms and inherent limitations for reconstruction of a complete body inertial rate vector (e.g., pitch, yaw and roll rate). In summary, a derivation of the kinematic and dynamic relationships is provided, allowing for simulation of out-of-plane displacement trajectories of the haltere. In reviewing these trajectories, a natural decoupling of the two in-plane inertial rate components is apparent. This is the most significant result of the current research. The vertical and lateral components of rate were, respectively, found to be proportional to the time averaged amplitude and time averaged slope of the trajectory at the center of the haltere stroke. When the dynamics were simplified, an

approximate linear form was found, thereby allowing the observation of decoupling of the rate components to be held as a general conclusion. Through coordinate transformation, the mathematical relations allowing for bilateral combination of the haltere-measured rates to construct signals proportional to the conventional body pitch, yaw, and roll rate components were summarized.

Simulations were constructed based on the assumed ability to measure averaged trajectory amplitude and slope, or equivalently strain and strain rate, at the center of the haltere stroke. These simulations quantify the error associated with the assumed linearity and associated rate decoupling. Simulations were executed over a wide range of pitch and yaw rate (-20 to 20 rad/s) and were presented for two roll rate cases (0 and 5 rad/s).

3.4.1 Mechanoreceptive Encoding

The question remains as to how the haltere mechanoreceptors provide rate component information to the insect motor control functions in a way that is compatible with the mathematical constructs described. Ideally, the insect could discretely sample strain and strain rate signals at the center of the haltere stroke, average these values over time, and thereby perfectly decouple the two inertial rate components in the plane of the haltere motion. The subsequent discussion will suggest ways in which the proposed decoupling mechanism may be consistent with the insect sensory and neuronal anatomy.

The haltere sensor structure is composed of a finite number of campaniform sensilla distributed in fields at the base of the haltere [30], [31]. The homologs to the haltere sensilla on the forewings are thought to individually be poor magnitude detectors due to their rapid saturation and high frequency functionality [35]. Unlike campaniform sensilla on locust wings that operate at lower beat frequencies and provide cyclic action potentials whose spike frequency likely does correlate well with strain magnitude [36], the campaniform sensilla on *Calliphora* wings are thought to fire phasically, perhaps once per stroke cycle at saturation [35].

Fayyazuddin and Dickinson documented research that characterized the afferents transmitted from the basal plate sensilla (dF2) and attempted to rule out the other campaniform fields in ipsilateral control of the wing muscles [28], [51]. Their conclusion was that dF2 was primarily responsible for steering motor control associated with mnb1 and that the connection consisted of both a fast monosynaptic electrical component and a slow chemical component. These studies did not report any attempt to distinguish between strain and strain rate as parameters for which there may be distinct proportional sensitivity. Additional studies are required to measure bilateral signal combination and the potential role of the sensilla of the chordotonal organ in the haltere which Pringle estimated were oriented preferentially to measure bending shear [14].

The basal field (dF2) is composed of roughly one hundred spatially distributed campaniform sensilla [30]. Assuming dF2 is primarily responsible for Coriolis sensing, the proposed hypothesis requires that the torque motor distinguishes between strain rate and magnitude of strain activating the sensor field. For example, as has been proposed for the insect wing [35], if the magnitude of strain is encoded through enlistment of increased numbers of sensilla within dF2, the compound extracellular potential would increase with strain magnitude. Similarly, strain rate might be encoded in the timing of the dF2 response, if the increased strain rate affected phasing of the response. Pringle reported proportionality of the temporal phasing of the spikes, believed to be coming from the basal field and large chordotonal organs, to the magnitude of yaw rate [14]. Fayyazuddin and Dickinson also demonstrated the impact of phasing of the signal from the haltere on wing muscle response, causing both adduction/abduction and amplitude variation in wing kinematics [51]. The monosynaptic connection between the halteres and mnb1 is sufficiently fast to synchronously transmit phasing information [51].

3.4.2 Mechanoreceptive Averaging Modality

The mechanism proposed for rate decoupling requires averaging of strain parameters on the upstroke and downstroke of the haltere. Averaging, as well as the bilateral

combinations described by (3–9)-(3–11), can be accomplished through a number of mechanisms. In addition to direct signal summation, low pass filtering resulting from tonic response may also provide a signal proportional to the average. A third possibility is to obtain the end effect of a difference or summation of drive signals through application of opposing drive motor pairs. For example, commanding an increased wing stroke amplitude on one side and independently commanding a decrease on the other side effectively provides the bilateral summation of the two commands in the form of a roll moment.

For pitch rate as defined in this chapter, the downstroke and the upstroke response is simultaneously expressed by the opposing halteres due to the bilateral symmetry of the sensor fields and the anti-symmetry of the Coriolis forces (see Figure 3-12 and Figure 3-13). Therefore, the strain magnitude from the upstroke of the two halteres could be simultaneously encoded and combined to generate a stabilizing torque proportional to pitch rate. Bilateral processing is not required in the case of the yaw rate component due to the bilateral symmetry of the halteres (Figure 3-13). Either haltere can provide a signal proportional to yaw rate by averaging the upstroke and downstroke strain magnitude of that haltere. Fayyazuddin and Dickinson showed both a phasic and a tonic component between the halteres and mnb1 [28]. The tonic response was sufficiently slow to effectively average a signal at the wing beat frequency. Unambiguously responding to roll rate errors would require bilateral summation of the averaged strain rate response from both halteres. Assuming some means of encoding strain rate, roll correction could be accomplished by ipsilaterally transmitting the signal through a signal path or muscle associated with wing stroke amplitude that is sufficiently tonic to average the signal. The combined effect of the two wings would then bilaterally combine to create the correcting roll torque.

Simulation results indicate that the rate decoupling mechanism described is fairly insensitive to the details of the encoding scheme. For example, when continuous, modeled strain and strain rate signals are passed through a weak low pass filter and then bilaterally combined according to (3–9)-(3–11), the mean signals track the true rate components well.

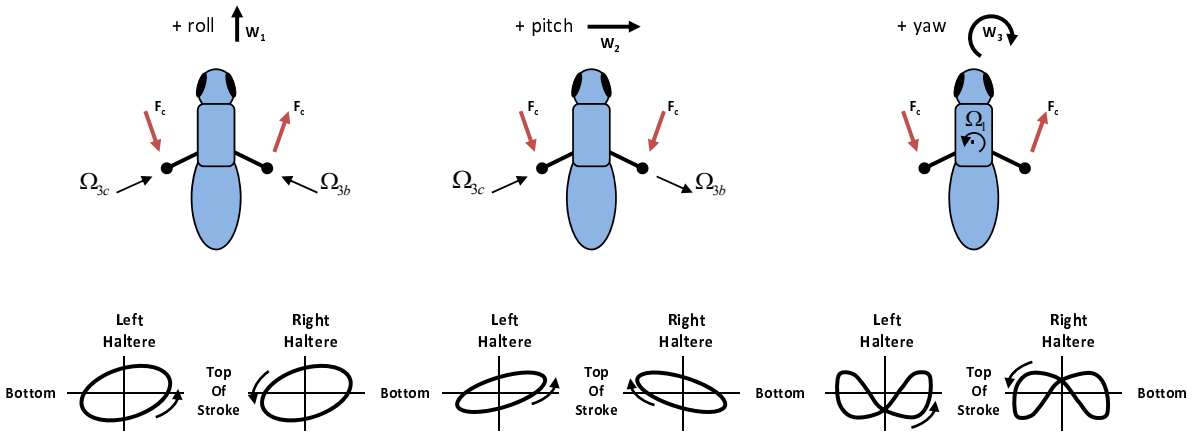

Figure 3-12. The Coriolis force induced by pitch rate has bilateral symmetry, but yaw and roll have antisymmetric forces. As a result, summing left and right haltere response allows direct determination of pitch rate without pre-averaging.

	Left Haltere	Right Haltere	Sum/2	Dif/2
Upstroke	$(m_r+m_p-m_y)*\gamma+(-b_r-b_p-b_y)$	$(-m_r+m_p+m_y)*\gamma+(b_r-b_p+b_y)$	$m_p*\gamma-b_p$	$(m_r-m_y)*\gamma+(-b_r-b_y)$
Downstroke	$(m_r+m_p+m_y)*\gamma+(b_r+b_p-b_y)$	$(-m_r+m_p-m_y)*\gamma+(-b_r+b_p+b_y)$	$m_p*\gamma+b_p$	$(m_r+m_y)*\gamma+(b_r-b_y)$
Average	$(m_r+m_p)*\gamma-b_y$	$(-m_r+m_p)*\gamma+b_y$	$m_p*\gamma$	$m_r*\gamma-b_y$

Figure 3-13. Linear approximations of the strain at the center of the haltere stroke. (m_r, m_p, m_y) represent the magnitudes of the roll, pitch and yaw rate of change of strain with respect to stroke angle. (b_r, b_p, b_y) represent the magnitudes of the roll, pitch and yaw strain with respect to stroke angle. The unilateral and bilateral processing required to decouple the components is clearly seen by summing and differencing the right and left haltere responses.

This indicates that encoding precisely at the center of the haltere stroke is not critical. The results of Chapter 4 demonstrate the feasibility of encoding and reconstructing the full body rate vector using only discreet compressive strain magnitude measurements to describe the symmetric and antisymmetric aspects of the haltere trajectory. These results indicate that while direct encoding of strain rate would represent a useful submodality of the dF2 field, it is not necessary. Chapter 4 will develop and document a more detailed model of the mechanoreceptor physiology and the torque motor steering control mechanisms in order to further establish the proposed model as a biologically plausible mechanosensory mechanism.

The reported simulation results assume a constant angular rate and therefore isolate the impact of Coriolis forces from body angular acceleration. For the case of low angular acceleration, the results imply the potential to distinguish the components of the body rate vector. Some authors have entertained the possibility that halteres are primarily angular acceleration sensors used for stabilization after extreme saccadic maneuvers [18], [19]. In contradiction, Hengstenberg et al. later demonstrated a direct correlation between angular rate magnitude and compensatory response [20]. The mechanics dictate that both yaw rate and yaw acceleration will cause the halteres to respond with a strain magnitude at the center of the stroke. These two effects will be indistinguishable and a stabilizing response to one will also be a stabilizing response to the other. Similarly, roll and pitch accelerations will increase the average strain rate in a way that provides negative feedback consistent with the Coriolis forces. The role of the halteres during saccades needs to be further investigated given the ability of flies to generate large angular maneuvers in the span of a few wingbeats [53]. Assuming similar amplitudes, as the period of a maneuver approaches the period of haltere motion, the impact of angular acceleration and Coriolis force will approach the same order of magnitude. While the model generated in this report (3–12) includes the body acceleration terms, it was outside the scope of this chapter to fully evaluate the impact of all possible kinematic scenarios on flight stability.

CHAPTER 4
RECONCILING THE PHYSICS WITH THE PHYSIOLOGY

4.1 Introduction:

The halteres of Diptera have been described since the 1930's as vibrating mechanosensors that are sensitive to Coriolis forces [13], [54]. Coriolis forces are the forces induced by velocity of a mass, the haltere mass in the present case, constrained to move in a rotating body reference frame [14], [23]. The kinematic description that leads to Coriolis sensitivity was initially documented by Pringle [14] and Nalbach [23]. Chapter 3 took the kinematic assessment a step further by providing a more complete simulation of the dynamics of the haltere. The dynamic simulation of the haltere motion led to discovery that to within a very good approximation the response of the haltere to the two rate components in the primary plane of haltere oscillation is decoupled at the center of the stroke. The average magnitude and rate of change of the haltere out-of-plane displacement at the center of the stroke are individually proportional to the two rate components. The third rate component, perpendicular to the primary plane of haltere motion, does not have a first order impact on out-of-plane deflection. The out-of-plane component introduces non-linear coupling errors into the process of measuring the other two rate components as was quantified in Chapter 3.

While the described dynamic assessment provided a firm mathematical basis for the ability of two halteres to capture and reconstruct three orthogonal components of a fly's inertial angular rate, it stopped short of reconciling the kinematics and dynamics with what is understood about the sensory physiology of the insect. That reconciliation is the intent of this chapter. In the assessment of Hengstenberg, while progress has been made in understanding the projections of the haltere sensilla, our biggest deficit in understanding of the haltere is how the stimulation of the haltere is encoded by the sensilla [3]. The afferent pathways of the haltere have been mapped out through histological analysis using dye fills of the haltere projections [1], [18]. These studies showed both strong ipsilateral

and weak contralateral projections. The projections of the haltere have been demonstrated to strongly mediate control of both the head and the wings in numerous studies [3], [20], [42]. The temporal accuracy of the afferents in the haltere nerve have been observed to maintain a tight phase relationship within the wing beat cycle [27], [51]. More recently, Fox and Daniels have shown with single fiber measurements that individual sensilla have a linear response out to frequencies more than double the haltere beat frequency [2]. As shown in Chapter 3, this is significant since the yaw component of body rate results in a Coriolis force that, due to the large amplitude kinematics of haltere motion, has a frequency at twice that of the haltere beat frequency.

The sensilla of the halteres have been inferred, from characterization of homologous campaniform sensilla on the wings, to respond individually in very simple fashion [35]. Unlike the sensilla on the wings of locusts, which respond with a slowly decaying series of spikes whose spike frequency increases as stimulus magnitude increases [36], [37], the sensilla on the halteres of higher dipterans are thought to only release a single action potential spike once or twice during a single period of oscillation [35]. As higher strains are introduced, more sensilla are enlisted due to their spatial distribution and the associated spatial variation of the strain field. Therefore, the equivalence to a sensor with a large dynamic range is ensured by having a sufficiently large number of identical sensilla distributed uniformly over a region where the strain response has a sufficient gradient. Some analogies to this form of fractionated enlistment of simple sensors can be found in the chordotonal organ in the legs of locusts [55] and the spindle controlled response of the muscles in vertebrates [56]. This appears to be a widespread control strategy in natural systems where large numbers of simple highly integrated sensors are used as opposed to few highly refined complex sensors.

The intent of this chapter is to demonstrate, using analytical models derived from current understanding of haltere physiology, the reconstruction of an arbitrary body rate vector. This chapter builds upon the previous dynamic modeling of the haltere in Chapter

3 to establish the feasibility of constructing the signals required for stabilizing control of insect dynamics using only a single field of unidirectional binary strain sensors. This modeled field is intended to be functionally representative of the dorsal basal campaniform field, dF2, on the base of the haltere [30]. This demonstration will thereby shed light on what is the largest deficit in understanding the function of halteres, the encoding of the inertial rates by the sensory fields of the haltere and the associated decoding of the rates in the form of reflexive control response by the wing control structures.

4.2 Methods and Experimental Procedures

4.2.1 Dynamics Model

The results provided in this chapter are based on analytical experimentation using a first principles model of the dynamics of the haltere. The model, as described in Chapter 3, assumes that in addition to the forces associated with inertia there are damping and stiffness forces limiting the out-of-plane motion (θ) of the haltere. Similar to Chapter 3, the dynamics equation is integrated in Matlab^{TM} under the influence of the haltere beating motion (γ) and the body roll, pitch and yaw rate (W_1, W_2, W_3) time history as expressed in the haltere reference frame ($\Omega_1, \Omega_2, \Omega_3$). See (3–12) from Chapter 3.

The in-plane motion of the haltere, gamma, was modeled in two forms, the first being a simple sinusoid with an amplitude of 90 degrees.

$$\gamma = A\sin(\omega_h t) \tag{4–1}$$

The second form was meant to approximate the measured stroke characteristics which are known to be more accurately represented by a triangle wave with much more uniform angular velocity during the most of the stroke [23]. The first few terms of a series representation were used,

$$\gamma = A\tfrac{8}{\pi^2}[\sin(\omega_h t) - \tfrac{1}{9}\sin(3\omega_h t) + \tfrac{1}{25}\sin(5\omega_h t) - \tfrac{1}{49}\sin(7\omega_h t)] \cdot 1.0531. \tag{4–2}$$

The frequency of the haltere stroke, ω_h, was chosen to be 200 Hz, maintaining traceability to Drosophila [42].

The relationships between the body rate components expressed in the body frame and the body rate components measured by the two halteres are the same as those used in Chapter 3,

$$W_1 = -\frac{\Omega_{b3} + \Omega_{c3}}{2\sin(\alpha)} \tag{4–3}$$

$$W_2 = \frac{\Omega_{b3} - \Omega_{c3}}{2\cos(\alpha)} \tag{4–4}$$

$$W_3 = -\frac{\Omega_{b1} + \Omega_{c1}}{2} = -\Omega_{b1} = -\Omega_{c1}. \tag{4–5}$$

In (4–3)-(4–5), the subscripts b1 and b3 represent the vertical and horizontal rate components in the plane of the right haltere. Similarly, subscripts c1 and c3 represent the vertical and horizontal rate components in the plane of the left haltere. The angle alpha defines the relationship of the haltere beating plane relative to a line perpendicular to the medial plane. For the current simulation, the haltere beating planes were folded back 30 degrees relative to the described perpendicular.

4.2.2 Campaniform Model

A field of 110 campaniform sensilla were modeled based on the number associated with the dorsal basal field by Gnatzy et al. [30]. The campaniform sensilla are assumed to fractionate the range of haltere displacement as a natural consequence of their spatial distribution over the base of the haltere. Each sensillum was modeled as if firing a unit impulse when the strain at its location reaches a strain threshold which was common for all sensilla in dF2. However, each sensillum will fire at a unique haltere deflection level due to the spatial distribution of strain over the base of the haltere. The deflection levels at which the individual sensilla respond were evenly distributed between haltere displacements of 0 and 0.001 radians. For an alternative representation, these

thresholds could be distributed to approximate the stochastic distribution of the sensillum characteristics and the specific structural characteristics of the haltere base. Due to the probable large variation within and among species, this level of detail was not considered fruitful for the purpose of this investigation.

The sensilla were assumed to respond only in tension and only during increasing tensile motion [34]. According to the morphological studies of Pringle this should occur during posterior bending of the haltere [14]. As the haltere passes through the tensile threshold during relaxation of the tensile load, reactivation was not allowed. The sensilla were modeled to fire as many times during the cycle as they passed through the threshold in the forward direction. Compressive loading associated with negative haltere displacement had no impact.

4.2.3 Modeling Process

A simulation experiment involved defining the roll, pitch, and yaw time history of the insect and then integrating the haltere responses to create the physical haltere trajectories under the influence of the dynamic rate loading. The time history was then processed with the model of the dF2 field. At each integration time step (5.0e-05 sec) the number of campaniform firings was recorded. This firing data for each haltere oscillation period contained the only data used to reconstruct the body rate disturbances. The specific algorithm required is described in the Results section of this chapter. The algorithm was applied in spreadsheet form to review in detail the results of the rate reconstruction process. The modeling process is demonstrated in Figure 4-1.

4.3 Results

4.3.1 Test Case Description

Although many cases were executed to verify the robustness of the encoding scheme, the results provided here as an example will focus on a case that combines roll, pitch and

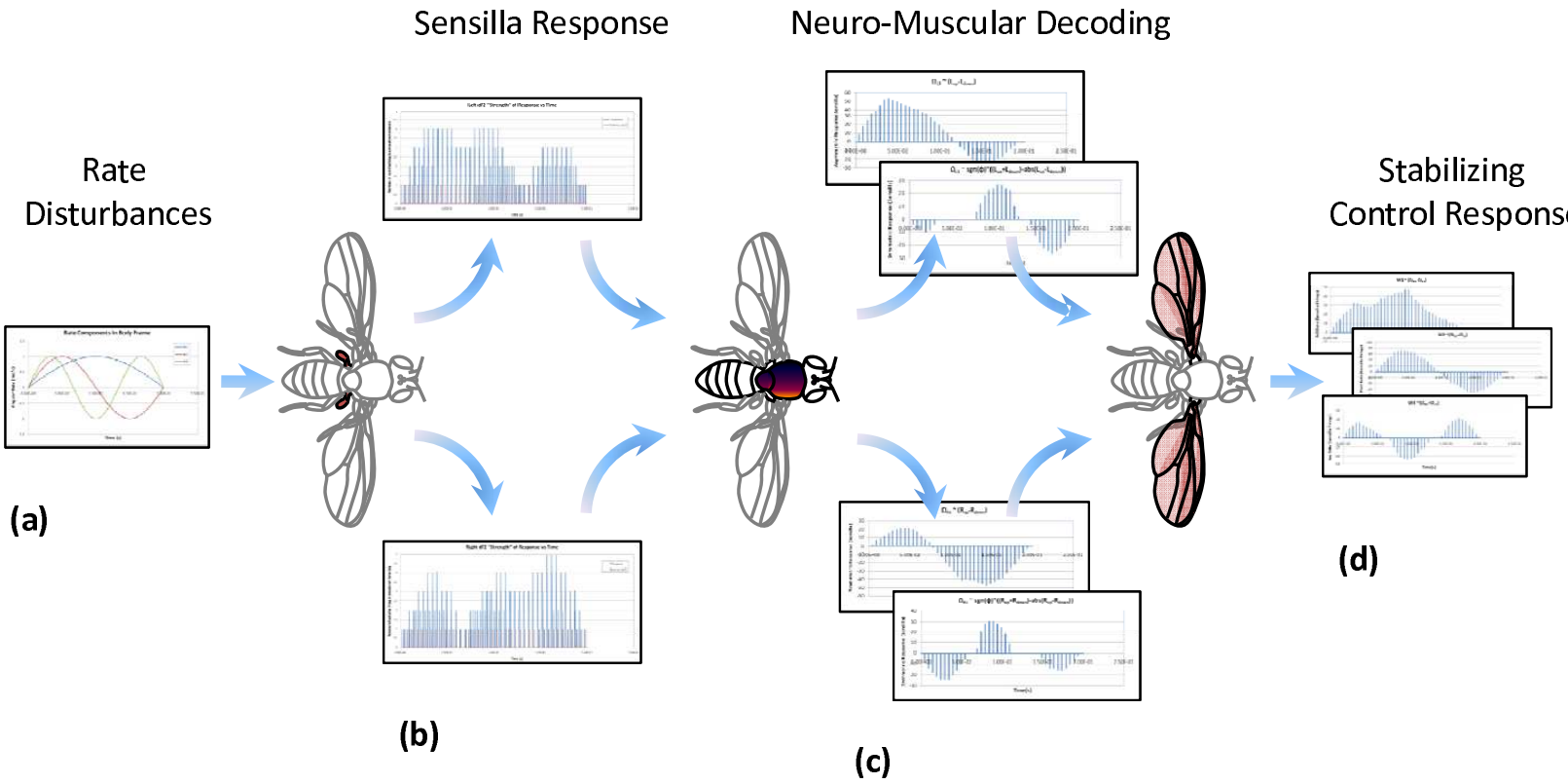

Figure 4-1. Functional processes are modeled to demonstrate the encoding and decoding of haltere sensory response. (a) Angular rate disturbances induce Coriolis forces that cause strain in the haltere base. (b) Compressive strains are recorded by 110 binary sensilla distributed over the haltere base. (c) Physical processes represent simple summation and differencing that decouple the orthogonal rate components in the form of wing forces. (d) Bilateral summation of the forces results in stabilizing reactions to pitch, yaw and roll rate disturbances.

yaw rates of disparate frequency.

$$\begin{aligned} Roll &\implies W_1 = 1.0\sin(5\pi t) \\ Pitch &\implies W_2 = 1.0\sin(10\pi t) \\ Yaw &\implies W_3 = 1.0\sin(15\pi t) \end{aligned}$$

Figure 4-2 shows the relationship between the rate components expressed in the conventional body fixed reference frame and two body fixed frames oriented preferentially in the planes of the right and left halteres. The trajectories of the simulated halteres are shown in Figure 4-3 with one oscillation period emboldened to aid in interpretation of the motion. Figure 4-4 shows the simulated extracellular potential (cumulative campaniform response) in relation to the haltere motion. The evenly spaced red lines in Figure 4-4 represent the point in time when the haltere is at the lower end of the stroke. Either one or two composite spikes are seen per cycle.

4.3.2 Campaniform Response Decoding Algorithm

Chapter 3 identified measurement of the average slope of the trajectory (strain) at the center of the stroke and the average displacement magnitude at the center of the stroke as sufficient to decouple the vertical and horizontal in-plane rate components. An interpretation of this result is that the vertical (yaw) rate component causes a symmetric haltere averaged response and the horizontal rate component causes an antisymmetric averaged response with respect to the mid-point of the stroke. For example, Figure 4-5 demonstrates trajectories for vertical and horizontal rate components individually. Any means that allows for measurement of the relative level of symmetry and asymmetry from the composite trajectory should be sufficient to obtain a stabilizing control signal. The slope could possibly be approximated through direct measurement of averaged strain rate at the center of the stroke or through differencing of strain magnitudes measured on both sides of the stroke center.

In the algorithm attempted, the period of oscillation is divided into two halves and the integrated campaniform response during each half is considered. These halves

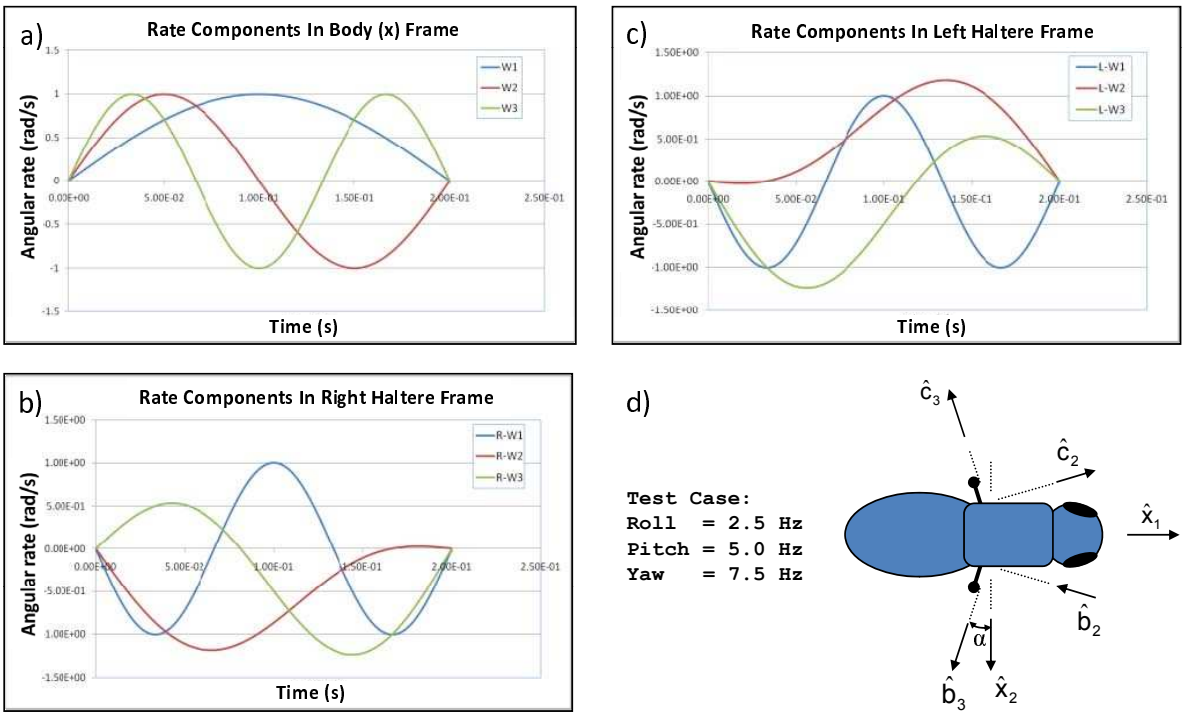

Figure 4-2. The simulation process takes the inertial rate vector defined in the body frame and recasts it into the haltere frames. Figure d) defines the reference frames and the frequency of rate variation for the open-loop test case. The first three figures represent a) the rate components in the body frame, b) the rate components in a reference frame attached to the right haltere, and c) the rate components in the frame attached to the left haltere.

correspond to the up-stroke and down-stroke of the haltere. The two composite campaniform responses are then differenced, providing an approximation of the asymmetry or average slope of the trajectory. The sign of this difference is indicative of the sign of the horizontal rate component. The average or summation of the two composite responses after removing the antisymmetric response is representative of the symmetric (yaw) component of the response. Determining the sign of the yaw component is more problematic than in the other case due to the frequency doubled nature of the haltere trajectory. However, nature has provided a rather unique solution. If the emboldened part of the top Figure 4-5b is studied closely and compared to the bottom where the sign of the rate has been reversed, it can be seen that the center of the campaniform responses on the two

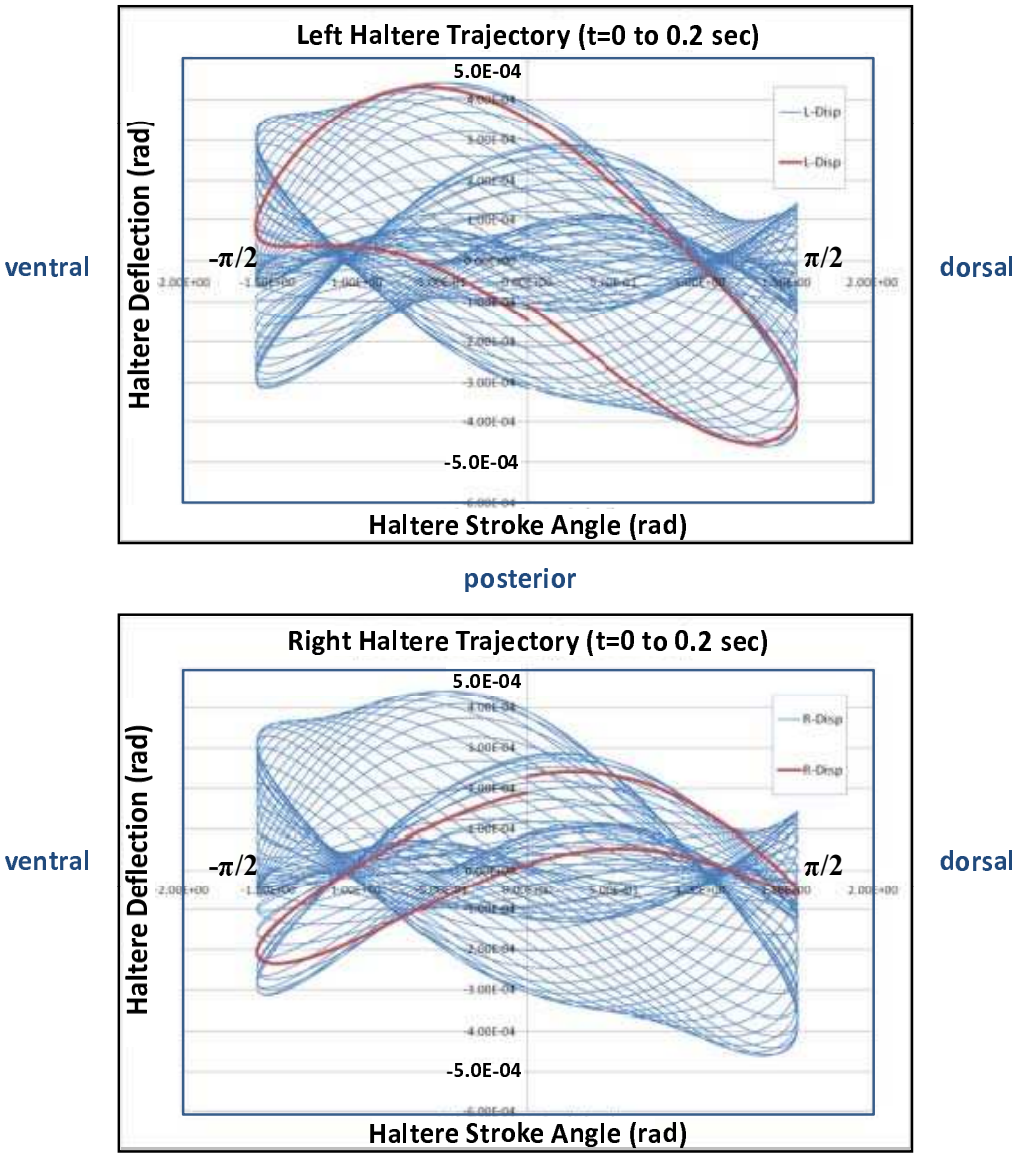

Figure 4-3. The dynamics expression, Equation (1), is solved individually for each haltere. The resulting trajectories are represented for the left and right halteres over 0.2 seconds or 40 haltere oscillations.

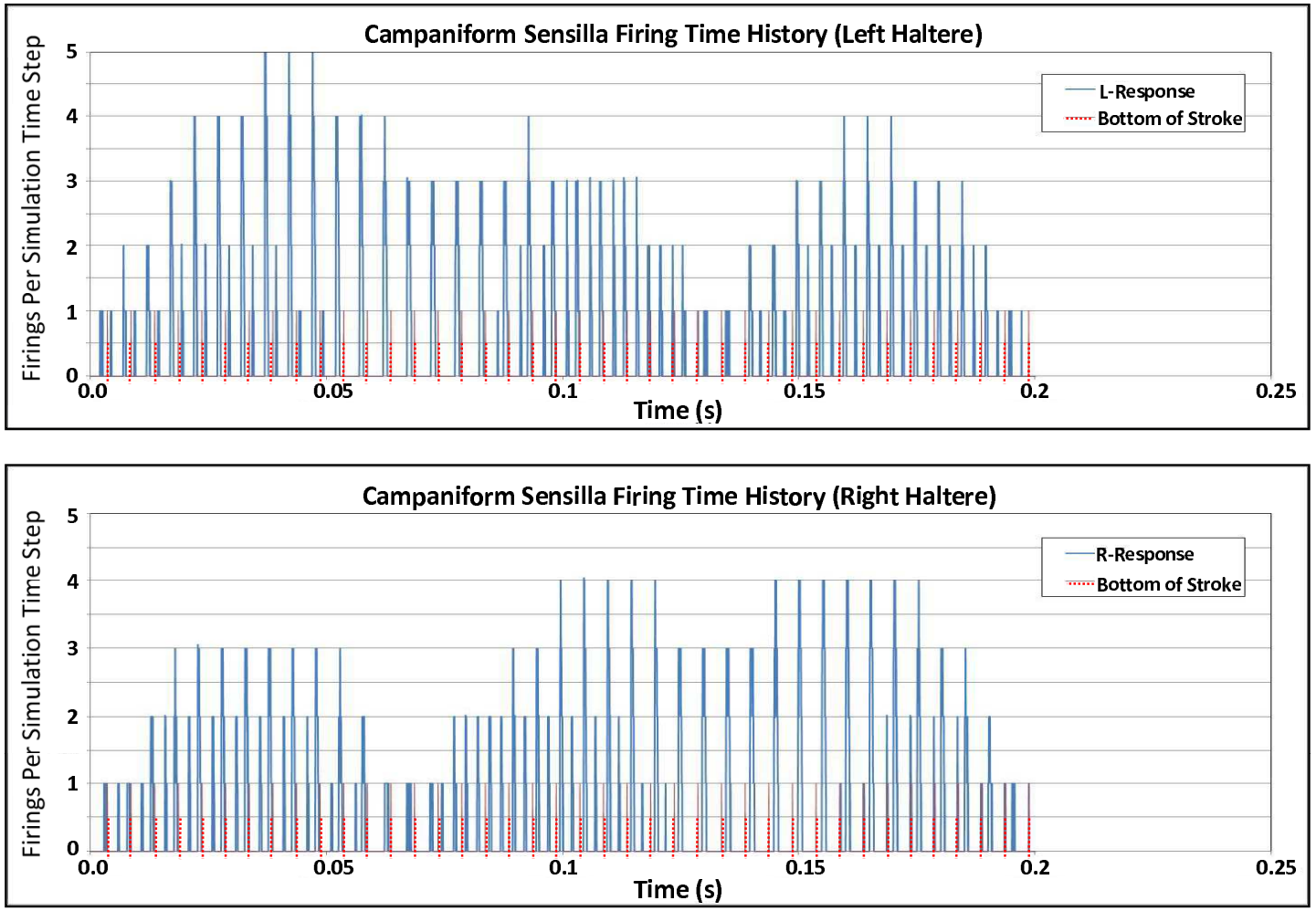

Figure 4-4. The sensilla responses are summed at each integration time step to represent the net motor control afferent response. The short evenly spaced marks show the bottoms of the haltere stroke as a timing reference. The current model predicts the compound response of the sensilla to appear as one or two bursts of sensilla spikes that show a distinct phase shift depending on the sign of the yaw stimulus.

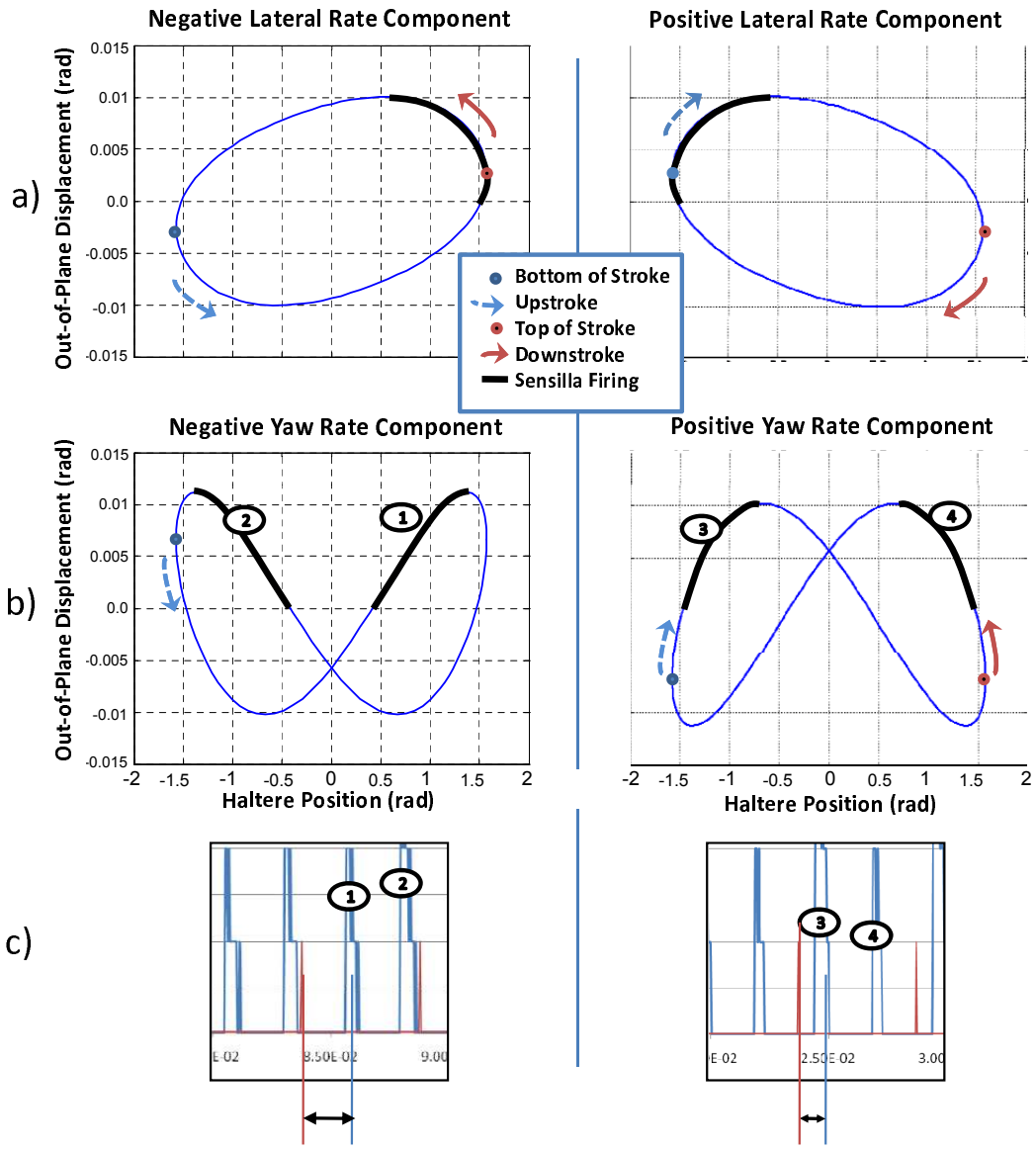

Figure 4-5. The response of the modeled campaniform sensilla (CS) always occurs on the same half of the displacement plane. a) Haltere response to only a lateral rate component. Whether the CS response occurs on the downstroke or upstroke determines the sign of the lateral rate. The difference between upstroke and downstroke CS response is related to the magnitude of the rate. b) Haltere response to only a yaw rate component. The sign of the yaw rate component must be determined by phase information since upstroke and downstroke have similar CS responses. c) Correlation of phase change of the composite response with sign of yaw rate becomes apparent if response is plotted versus time.

curves are distinctly shifted in phase. This shift is roughly constant and to large degree independent of the magnitude of the yaw motion. For the described algorithm this shift in phase of the centroid of the composite spike was used as an indicator of the sign of the yaw component. The described algorithm is summarized mathematically below:

$$\Omega_3 = R_{up} - R_{down} \tag{4–6}$$

$$\Omega_1 = sgn(\psi)(R_{up} + R_{down} - abs(\Omega_3)). \tag{4–7}$$

In these expressions, the variables are defined as follows:

$\Omega_1 =$ yaw rate component,

$\Omega_3 =$ lateral rate component,

$R_{up} =$ cumulative upstroke campaniform field response,

$R_{down} =$ cumulative downstroke campaniform field response,

$sgn(\psi) =$ sign of the yaw rate component as determined by the relative phase of the campaniform field response.

4.3.3 Algorithm Application

The result of the described algorithm is demonstrated in Figure 4-6, showing approximations of the two measurable rate components in the right haltere reference frame. Figure 4-7 shows the reconstruction of the roll, pitch and yaw body rates from these haltere measurements according to (4–3), (4–4) and (4–5). Figure 4-8 shows the same result using the triangular waveform of (4–2).

4.4 Discussion

4.4.1 Significance of Findings

The results documented in Chapter 4 demonstrate that a single unidirectional sensing modality (strain magnitude) on a pair of halteres is sufficient to encode the three orthogonal body rates. With the proposed model, a single haltere can encode the two rate components in the plane of haltere oscillation. Due to the non-coplanar geometry

a)

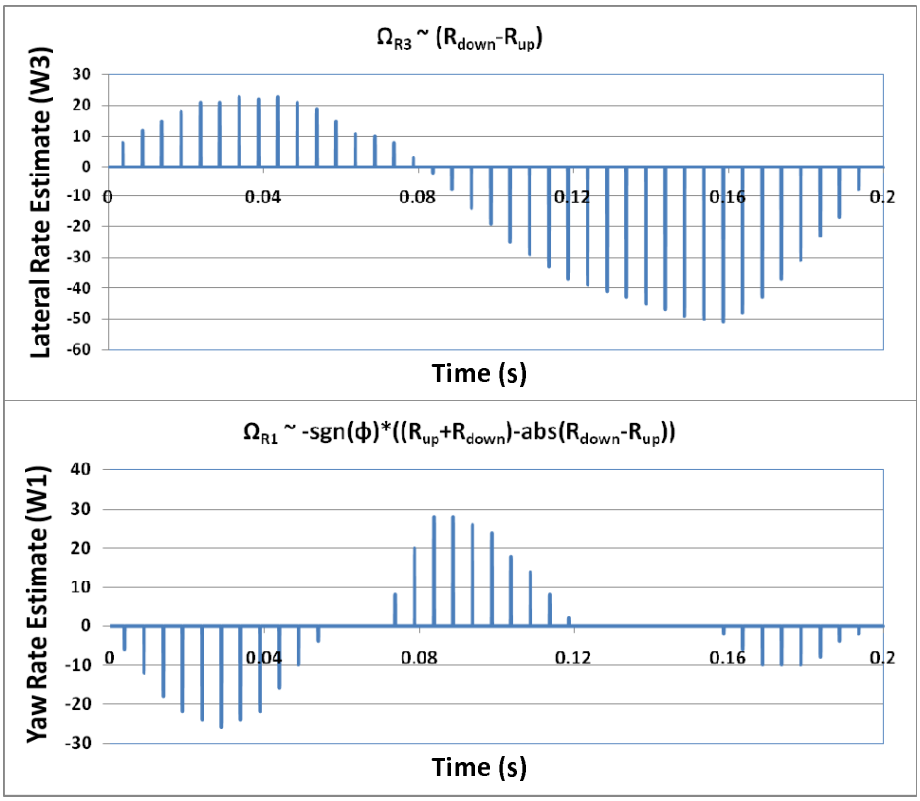

b)

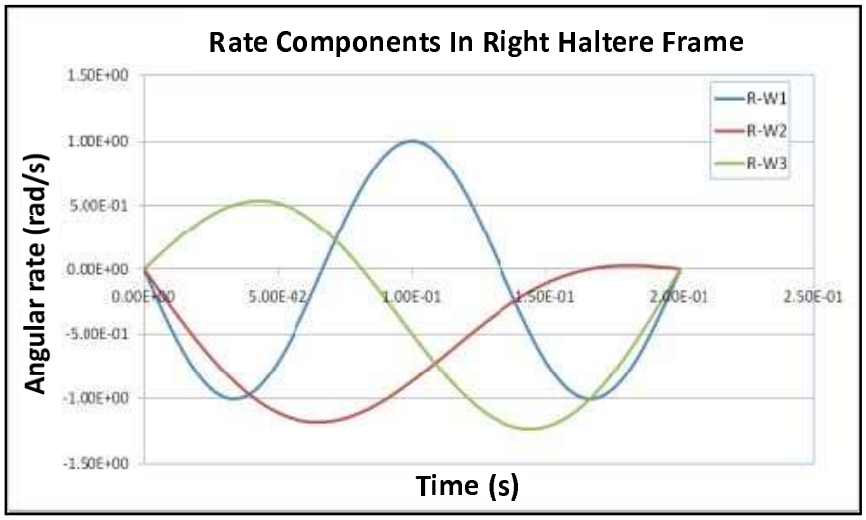

Figure 4-6. Application of the mathematical operations described by (4–6)-(4–7) result in signals whose magnitude roughly represents the two orthogonal rate components influencing out-of-plane displacement of the right haltere. a) Rate components resulting from decoding the unidirectional campaniform responses. b) True rate components for comparison with the decoded approximations.

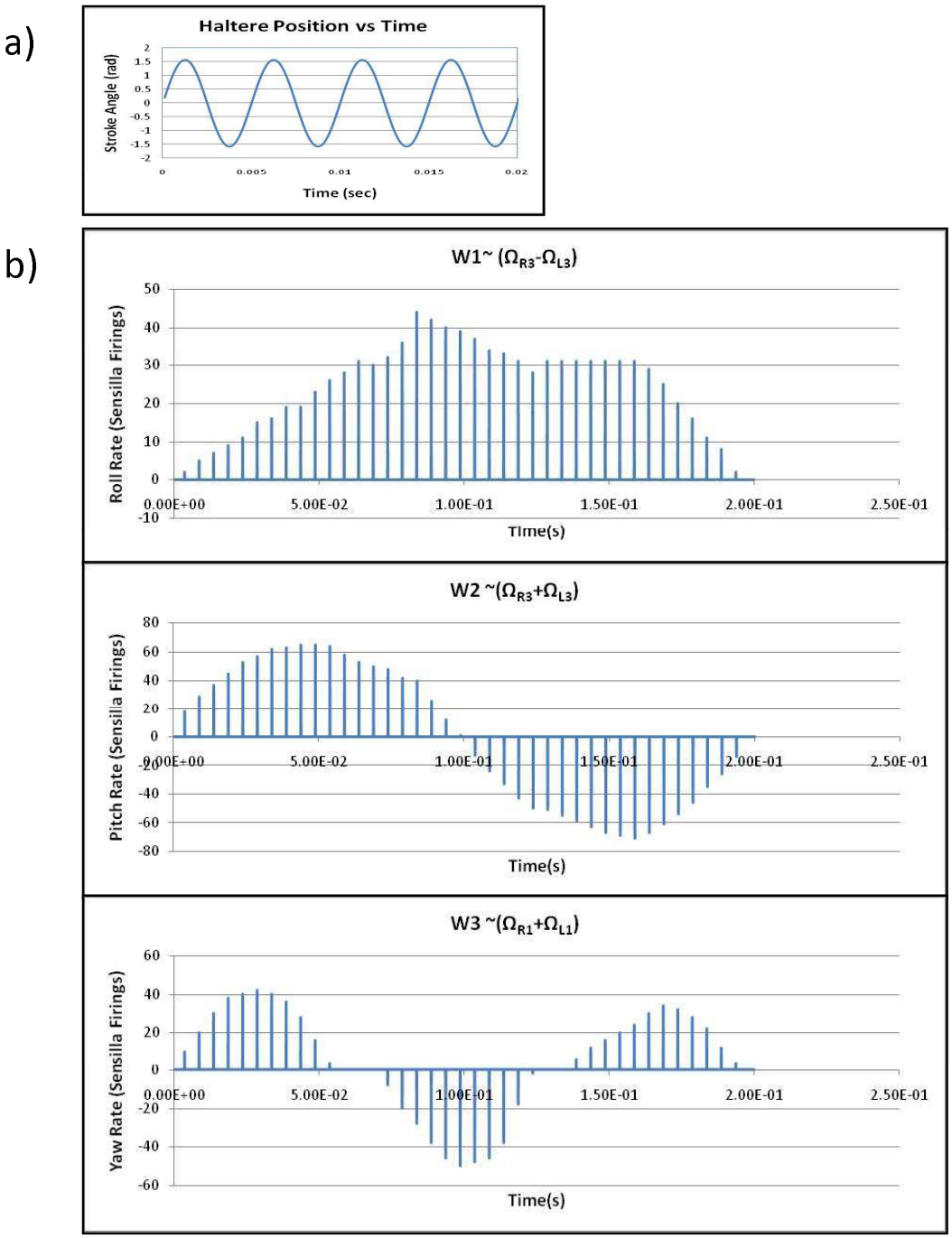

Figure 4-7. Unilateral response of the wings to haltere afferents results in forces that when combined according to the constructs of (4–3)-(4–5) provide net torques proportional to original disturbances. a) Sinusoidal time history of haltere stroke angle. b) Decoded signals proportional to rate components in the right and left haltere reference frames.

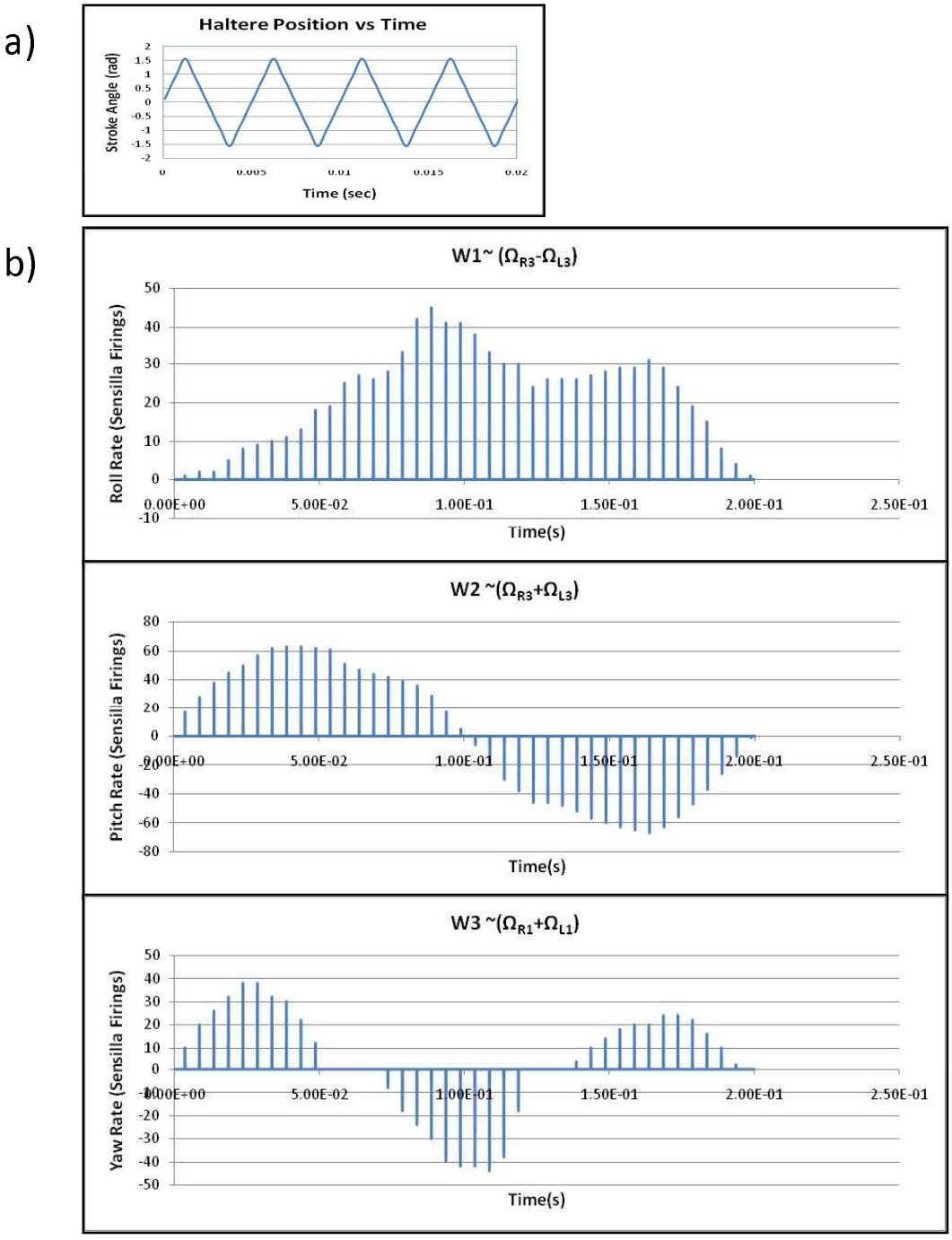

Figure 4-8. Haltere derived rate estimates under the influence of a more realistic "saw-tooth" motion profile. a) Triangular or saw-tooth time history of haltere stroke angle. b) Decoded signals proportional to rate components in the right and left haltere reference frames.

of the two haltere oscillation planes, the combined influence of two halteres can mediate stabilizing control of the three orthogonal components of an arbitrary rate disturbance. Further, the results indicate that with only an ipsilateral influence over wing kinematics, simple summation and differencing of wing forces (4–3)-(4–5) will result in net torques that are proportional to the pitch, yaw and roll rate disturbances.

The proposed model satisfies the observed constraint that the campaniform sensilla from dF2 are primarily responsible for encoding rate disturbances [1], [18], [28]. As shown in Chapter 3, decoupling of the rate components depends on measurement of signals proportional to the averaged slope of haltere displacement and the averaged magnitude of haltere displacement near the center of the stroke. However, analogous to a finite difference approximation of a derivative, if the ability to difference strain magnitudes is allowed, direct measurement of the averaged slope of the haltere trajectory, or the related quantity – strain rate, is not required. The proposed model has no fundamental need for additional input by other campaniform fields or by the chordotonal organ of the haltere base for rate stabilization. Additionally, the encoding of the rates by dF2 could be as simple as a binary response at a fixed threshold. As the work of investigators such as Fox and Daniel progresses, more complicated models encompassing the dynamic response characteristics and statistical variations in sensilla response can be incorporated [2]. The current results demonstrate that the sensilla only have to react in the most rudimentary way to encode sufficient information to reconstruct stabilizing signals. This does not in any way preclude the necessity for fusion of information from other sensor modalities to explain the complex behaviors, such as target pursuit, of the living organism.

4.4.2 Directional and Temporal Sensitivity of Campaniform Encoding

One of the most fundamental hurdles that the proposed model overcomes is the enforcement of the constraint that the campaniform sensilla respond only to unidirectional stimulus. Detailed descriptions of the histology and morphology of the campaniform sensilla have been provided by a number of authors [29], [30], [57], [58]. Pringle concluded

through self-proclaimed circumstantial morphological and behavioral evidence that the campaniform sensilla on the legs of Periplaneta are sensitive to a unidirectional strain field in which compression exists along the longitudinal axis of the campaniform cap [31]. In his comprehensive paper on halteres, Pringle reiterated his conclusions about campaniform directional sensitivity and suggested based on their morphology that the pertinent sensilla should only respond during forward bending of the halteres [14]. Sandeman and Markl appeared to confirm this prediction when they observed that they could only measure an afferent response during forward acceleration of the haltere end knob [18]. Later experiments on *Periplaneta* by Zill et al. established conclusively that the campaniforms on *Periplaneta* were not sensitive to compressive strain parallel to the long axis of the campaniform cap but instead to tensile strain [34], [59], [60]. The demonstrated model conforms to that finding, i.e., a strain field with a tensile component parallel to the long axis of the cap causes a campaniform response. A possible explanation of the Sandeman results [18] would be that the applied forward force against the haltere shaft resulted in inertial forces that caused the haltere to actually bend backward as if influenced by Coriolis forces causing backward bending. The simulation results provided in this chapter establish that haltere displacement measurements, encoded by unidirectional sensors that fractionate the range with simple threshold induced responses, are sufficient to encode inertial angular rates. This result would have been qualitatively the same regardless of the assumed orientation of the sensors.

The most recent measurements of haltere afferents have been measured on single fibers in close proximity to the haltere base [2]. These measurements demonstrated that on Holorusia the afferent response accurately tracks the haltere response linearly well above twice the oscillation frequency of the halteres. This corresponds well with the requirements of the current results. The timing of the response of the modeled campaniforms depends primarily on the trajectory of the haltere displacement which under certain combinations of angular rate might be quite complicated. The separation

of consecutive responses from a given sensillum could in general be much less than half the period of oscillation. This implies a requirement for sensilla to respond at higher than twice the frequency of haltere oscillation. For a higher frequency typical of Drosophila, 200 Hz, the ability of a sensillum to respond, recover, and respond in a time span of less than 2.5 msec is indicated.

4.4.3 Phase Sensitivity of Campaniform Afferents

The proposed model incorporates the phase of the initial composite dF2 response to determine the sign of the yaw rate component. A correlation between signal phase and haltere response has been documented by a number of authors. Pringle hypothesized that the large chordotonal organ acted as a timing reference and that the sign of the yaw rotation was determined by whether the response from the basal plate was before or after the chordotonal response [14]. Pringle also speculated that yaw rotation magnitude correlates with both the timing of the sensilla burst and the number of sensilla enlisted in the response. The timing reference used in the current model to determine the sign of yaw rate is based on a fixed point in the phase of the oscillation and not on a dedicated sensory response. Heide observed a strong phase locking effect between the ipsilateral haltere and the motor neuron of the first basalar muscle (MNB1) and weak phase locking between the contralateral haltere and MNB1 [27]. Heide also correlated phase of potential spikes in MNB1 with wing amplitude [27]. An asymmetric change in wing beat amplitude at a fixed frequency would be expected to cause differential thrust, thereby inducing a torque. Fayyazuddin and Dickinson demonstrated in Calliphora that the haltere afferents were tightly controlled in phase [28]. In their model, under nominal conditions wing afferents entrain the firing phase of B1. When the insect rotates, the phase of the haltere afferent shifts sufficiently to entrain MNB1, transiently phase locking and thereby shifting the firing of the B1 muscle [51]. The importance of phase in control of the B1 steering muscle is consistent with the analytical finding that dF2 firing phase has a direct influence

on control of yaw rotational disturbances. Although it has not been demonstrated experimentally, a correlation between phase and sign of the yaw rate is a logical extension.

4.4.4 Physiological Implications of Afferent Decoding

While "encoding" of rotational rates by the dF2 campaniform field in the haltere afferent could, as illustrated by the described model, be quite straightforward, the "decoding" of the afferents in order to generate decoupled stabilizing torques is likely much more sophisticated. The signs and the magnitudes of the rates must be preserved in the influence of the steering muscles. The control implementation must effect a coordinate transformation so that the non-orthogonal rate components from the two haltere frames combine to independently represent torques associated with orthogonal body rotations. This requires reconciliation of the insect physiology with the simple mathematical constructs of (4–6)-(4–7) and (4–3)-(4–5). As previously described, this process can be broken into two steps, the first being ipsilateral control of wing steering muscles to generate torques representative of (4–6)-(4–7) and, the second, a simple summation of torques in conformity with (4–3)-(4–5). The expressions in (4–6)-(4–7) require:

1. Summation of upstroke and down stroke composite response of the campaniform field.
2. Differencing the upstroke and downstroke composite response.
3. Phase sensitivity of the composite response to determine the sign of the yaw motion.
4. Differencing of 1) and the magnitude of 2).

Assuming the existence of such muscular and neurological constructs, signals proportional to the two in-plane rate components are available. These must then manifest in the form of (4–3)-(4–5). For example, a scheme could be postulated using independent control of supination/pronation and amplitude states of the two wings and a common abduction angle to allow for five degrees of freedom controlling all but the residual lateral force component (personal observation).

Numerous means of summation and differencing of upstroke and downstroke afferents can be postulated, involving antagonistic muscle pairs or competing inhibitory and excitatory influences. The fact that the haltere oscillation has generally been observed to have a fixed phase relationship with the wing is likely necessary to establish a stable reflexive response. Similarly, the common frequency between the wings and halteres could be postulated to be necessary to fulfill the need for summation and differencing of the upstroke and downstroke afferents expressed by the haltere. For example, a supination increase on the upstroke along with the same supination increase on the downstroke would have an additive effect as required by (4–7). However, a force increasing the amplitude on the upstroke and the same force applied on the downstroke could conceivably have an antagonistic effect, fulfilling the requirement for differencing in (4–6). Any number of physiological solutions to the problem of afferent decoding could be postulated given the limited experimental evidence. It is likely that different levels of evolutionary refinement may have resulted in a range of implementation variations among species.

4.4.5 General Observations

The resulting estimates of angular rate from the campaniform response show significant deviations from the true angular rate components as demonstrated in Figures 4-6, 4-7 and 4-8. This is due to the complex patterns of motion induced by combinations of pitch, yaw and roll rates. Intuitively, (3–12) can induce quite complex motion under the influence of non-linear rate coupling terms, angular accelerations, and the predominant Coriolis accelerations. Careful inspection of the campaniform response in Figure 4-4 shows areas where only a single burst of sensilla potentials occurs instead of the more common occurrence of one on the upstroke and one on the downstroke. The simplistic model employed requires a spike on downstroke to determine the sign of the yaw rate estimate. If there is not an estimate then the default value for the yaw rate is zero. Figure 4-6 clearly shows during periods when only a single spike occurs during the oscillation, the estimate for yaw rate goes to zero. This is analogous to the response of the motor neuron for the

B1 muscle staying phase locked to the phasic wing campaniform response unless the signal from the haltere falls within the appropriate phase band [51]. A more sophisticated algorithm or a band limited response of the individual sensilla might mediate this effect to some extent. One observation apparent in Figures 4-7 and 4-8 is that the gaps in response are minimized in the combined result of two halteres. When a single composite spike is limiting the estimate from one haltere, in general the same is not occurring at the other haltere which has a significantly different orientation than the first. Therefore these errors are mitigated to some extent in the summation of the reflexive responses mediated by two halteres.

The current model has demonstrated the feasibility of encoding and reconstructing a stabilizing response to arbitrary disturbances using a field of unidirectional, binary strain sensors at the base of the haltere. The model however is limited by the rudimentary representation of the sensilla and limited understanding of how the campaniform afferents are decoded by the wing steering mechanisms. Future work will attempt to provide more realistic band limitations on the sensilla and include a representation of the haltere model in a 6 degree of freedom flight model. The flight simulation environment will allow for investigation of reflexive responses to pattern generated maneuvers and the fusion of other sensor modalities into the flight control structure.

CHAPTER 5
6DOF CONTROL REALIZATION WITH HALTERE FEEDBACK

5.1 Introduction

Chapter 3 provided the mathematical basis for the ability of halteres to decouple the two rate components in the stroke plane of the haltere. Chapter 4 demonstrated a functional model for rate encoding compatible with known constraints associated with haltere sensory physiology. The conclusion of the analysis in these earlier chapters was that a single field of roughly one-hundred campaniform sensilla, acting as binary threshold sensors, can encode both the magnitude and the rate of the two angular rate components in the plane of haltere oscillation. The output of two halteres can be combined, either through bilateral afferent combination or through bilateral force summation, to reconstruct a resultant proportional to the full angular rate vector of the insect body. Chapter 4 only demonstrated rate encoding in one time-varying test case, without feedback to an attitude control loop. The intent of this chapter is to demonstrate the ability of the derived haltere model to provide necessary control stability in a much more rigorous and dynamic environment. That environment includes full 6 degree-of-freedom (6DOF) controlled motion in a scenario that involves competing objectives: target acquisition, egress toward target, obstacle avoidance, and target homing. Whereas the example of Chapter 4 included sinusoidal body rate components of different frequencies, the simulations of this chapter are driven by responses to non-linear activation functions and are only limited by the attitude control bandwidths assumed for the simulated insect, *Calliphora vicina*.

Numerous authors have studied the kinematic characteristics of fly wing motion and the resulting dynamic motion of flies [16], [61]–[65]. The flight of insects has been of particular interest to the scientific community because of the statements by early researchers that it was “impossible” for insects to fly based on the application of conventional aerodynamic understanding. This was true due to the fact that steady state aerodynamic models are inadequate to predict the forces on fly’s wings. Insects are now

understood to be able to provide sufficient lift for their bodies by dynamic amplification resulting from processes such as vortex entrainment at the ends of the wing stroke [66]. The casual observer conventionally thinks of articulated wings in insects moving vertically as is typical in birds. However, in animals that fly slowly or hover, such as hummingbirds and many insects, the wings move predominantly back and forth in an almost horizontal plane, generating thrust sufficient to lift the weight of the body. In some ways this is similar to the flight of a helicopter, generating mainly upward thrust and moving forward by tilting the plane of its oscillating wings forward. Unlike helicopters which gain some stability from the angular momentum maintained by the rotating components, the angular momentum of the two wings of insects nearly cancels. Insects of the order Diptera augment flight stability using rate feedback from the halteres to provide active damping to their attitude control.

No fewer than 18 pairs of synchronous control muscles fine tune the trajectory of the wings [64]. In addition, two opposing sets of large muscles in the thorax are asynchronously driven into a state of stretch activated oscillation to power flight [61]. While complete understanding of the mechanical processes associated with insect flight is not yet available, some theorize that energy is conserved to some extent by storing it cyclically in the muscles as in springs, adding power as necessary to replace the energy lost in the generation of aerodynamic power [67]. Some control muscles are thought to impart phasic forces on the wing during the stroke cycle, and the effect is thought to be tonic in others, providing continuous tension to influence parameters such as wing abduction angle or the degree of pronation [64].

A tight control loop is known to exist between the halteres and the wings, with signal transport sufficiently accurate to preserve phase information associated with the response of the halteres [28], [51]. The wings are known to be sensitive to the phase of the campaniform responses from the basal field (dF2) in particular. While the halteres provide rate stabilization, strongly supplementing any rotational aerodynamic damping,

the insects visual system provides a source of accurate steering commands and possibly rate information from optic flow sensitivity. The information from the eyes is known to be of somewhat limited utility in rate stabilization at high frequencies due to the factor of ten (roughly) longer latency inherent in the transport of the photonic information through the visual processes and interneurons. In addition, the eyes are to some extent isolated on the head from the very motion that the measurements would be trying to influence. The halteres on the other hand affect a significant body response from 50 -1500 deg/s. It has been demonstrated that blinded flies can still fly, while flies with ablated halteres have lost flight stability [3].

Obstruction avoidance is a significant technical hurdle for systems that intend to fly autonomously in complex environments. In addition to basic rate stabilization, the results described in this chapter are used to demonstrate synthesized behavioral response in the presence of randomly generated obstructions. Nature appears to handle this requirement well by using the optical measurements provided by the compound eyes to influence the flight trajectory [68]. Flies are well known for their saccadic maneuvers where they rapidly turn through a large angle (10 to 90 deg) in response to a blooming visual stimulus [53]. These maneuvers take their name from the motion of the mammalian eye which is continuously jumping from one point to another. In the case of the fly, these maneuvers take the form of a bank-to-turn, where the insect rolls its body in order to optimally apply forces and moments to reorient its body and velocity vector away from a looming object. To the extent possible without detailed simulation of aerodynamic response, saccade-like maneuvers are captured in the described simulation study.

5.2 6DOF Simulation Methods

The simulation of the flight dynamics consists of a standard 6DOF formulation [69]. The derivation of the thirteen first order differential equations is included in Appendix 2 for completeness. This formulation, which is based on quaternions, was chosen to eliminate singularities associated with integration of Euler angle derivatives. The representation

used is a direct simplification of that provided in Phillips. Torque components associated with rotating mechanical assemblies, thrust offsets relative to the center of gravity, and wind offsets were not required and therefore were eliminated. Although natural systems are composed of multiple bodies some of which are oscillating harmonically, e.g., wings and halteres, the net influence of the oscillating angular momentum of these components is currently assumed to be small. The thirteen governing equations are

$$\begin{Bmatrix} \dot{u} \\ \dot{v} \\ \dot{w} \end{Bmatrix} = g \begin{Bmatrix} 2(e_x e_z - e_y e_0) \\ 2(e_y e_z + e_x e_0) \\ e_z^2 + e_0^2 - e_x^2 - e_y^2 \end{Bmatrix} + \frac{g}{W} \begin{Bmatrix} F_{x_b} \\ F_{y_b} \\ F_{z_b} \end{Bmatrix} + \begin{Bmatrix} rv - qw \\ pw - ru \\ qu - pv \end{Bmatrix} \tag{5–1}$$

$$\begin{Bmatrix} \dot{p} \\ \dot{q} \\ \dot{r} \end{Bmatrix} = [I]^{-1} \begin{Bmatrix} T_x + (I_{yy_b} - I_{zz_b})qr + I_{yz_b}(q^2 - r^2) + I_{xz_b}pq - I_{xy_b}pr \\ T_y + (I_{zz_b} - I_{xx_b})pr + I_{xz_b}(r^2 - p^2) + I_{xy_b}qr - I_{yz_b}pq \\ T_z + (I_{xx_b} - I_{yy_b})pq + I_{xy_b}(p^2 - q^2) + I_{yz_b}pr - I_{xz_b}qr \end{Bmatrix} \tag{5–2}$$

$$\begin{Bmatrix} \dot{x}_f \\ \dot{y}_f \\ \dot{z}_f \end{Bmatrix} = \begin{Bmatrix} e_0 \\ e_x \\ e_y \\ e_z \end{Bmatrix} \otimes \left(\begin{Bmatrix} 0 \\ u \\ v \\ w \end{Bmatrix} \otimes \begin{Bmatrix} e_0 \\ -e_x \\ -e_y \\ -e_z \end{Bmatrix} \right) \tag{5–3}$$

$$\begin{Bmatrix} \dot{e}_0 \\ \dot{e}_x \\ \dot{e}_y \\ \dot{e}_z \end{Bmatrix} = \frac{1}{2} \begin{bmatrix} -e_x & -e_y & -e_z \\ e_0 & -e_z & e_y \\ e_z & e_0 & -e_x \\ -e_y & e_x & e_0 \end{bmatrix} \begin{Bmatrix} p \\ q \\ r \end{Bmatrix}. \tag{5–4}$$

In this formulation, (u, v, w) are the velocity components of the vehicle relative to the inertial frame expressed in the body frame, (p, q, r) are the rotation rate of the body relative to the inertial frame expressed in the body frame, (x, y, z) are the position coordinates in the inertial frame and (e_0, e_x, e_y, e_z) define the unit quaternion used to transform from body to inertial reference frames. Further, $\otimes$ represents quaternion multiplication, $(F_{x_b}, F_{y_b}, F_{z_b})$ represent the net forces acting on the body as represented

in the body frame, (T_x, T_y, T_z) represent the net torques around the center of mass as represented in the body frame, W/g is the mass of the vehicle, and $[I]$ is the inertia matrix in the body frame with respect to the center of mass. These equations are integrated by initializing with a 4th order Runga Kutta method and then immediately transitioning to a 4th order Adams-Bashforth-Adams-Moulton predictor-corrector method for increased efficiency [70].

5.2.1 Behavioral Decision Logic (Brain)

The brain of the simulated insect is modeled as a neural network, represented by a series of nonlinear activation functions the output of which are summed together with appropriate gains. Unlike a conventional neural network, the output of these activation functions are unit vectors that when combined together and normalized result in a desired navigation direction. This process is represented in the box entitled Optical and Olfactory Processing in Figure 5-1. The output navigation unit vector determines the In the case of control response to a measured error, e.g. altitude, the activation function is recast as a hyperbolic tangent with anti-symmetry around the desired value. In the case of altitude, the response can be thought of as a proportional gain on error providing a signal with scalable upper and lower limits between 1 and -1.

The inputs to the neural network are representative of olfactory and optical signals. The rate of growth of an object in the visual field can provide a stimulus for obstruction avoidance, taking into account both velocity toward an object and the range to the object. The angular rate of growth of the cylinderical obstructions is represented as $(\frac{V_{perp}}{R})$, where R is the range to the obstruction, and V_{perp} is the magnitude of the velocity component along the range vector. The direction to a desired target is also assumed to be measured both through optical and chemical means. The thresholds used are significantly different however. The activation threshold for olfactory measurement was picked to be a large number, 15 meters, while the activation threshold for optical measurement was set nominally at 1.5 meters. Implicit in both of these settings are assumptions with

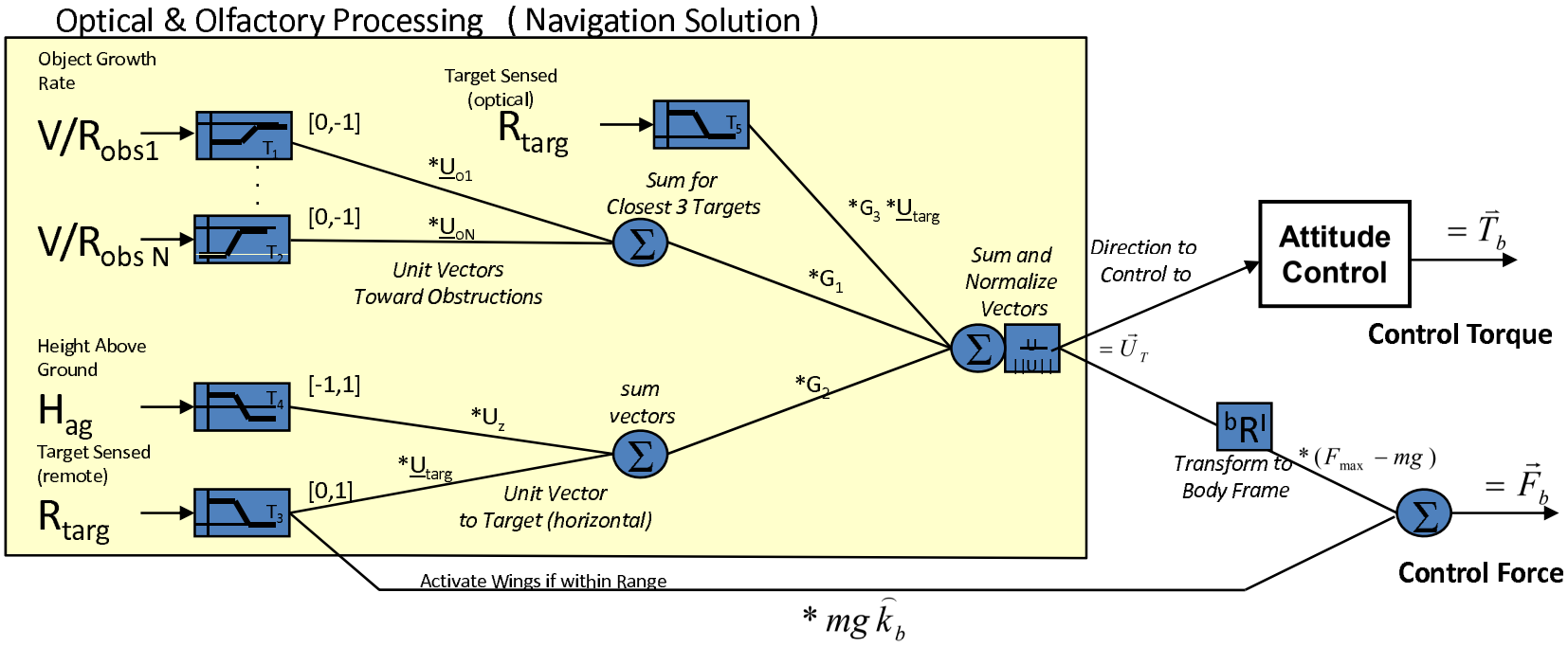

Figure 5-1. Non-linear response activation logic for the simulated insect. A navigation solution is determined by olfactory and optical inputs to non-linear activation functions. Errors between desired an actual body position and orientation determine control forces and torques.

respect to a decreasing ability to resolve target signatures with range. The premise for the simulation is that the insect will be initially at a location on the ground until the time that the olfactory signal rises above some threshold. The insect will then take flight and move toward the target. If successful in avoiding obstructions and approaching the target within the optical acquisition threshold, it will acquire the target optically and intercept the target. The final assumed input is an optical measurement of altitude. After taking off, the insect will be motivated to maintain a constant altitude within the limitations of the other competing objectives. For the purpose of this simulation, the target location and the current altitude are assumed to be known exactly.

5.2.1.1 Long Range Activation

The long range activation (σ_h) is represented by a simple sigmoid function (5–5) whose input is the difference between range-to-target and a preset activation range ($R_{t\,\mathrm{arg}} - R_{threshold}$). This response is equivalent to a thresholded activation caused by an acoustic or olfactory signal that is functionally dependent on range to the target. The offset for activation was arbitrarily chosen to be 15 meters. The threshold difference range is gained by G_{LR} to affect the sensitivity of the activation. The output of the activation function is multiplied by a unit vector, $\hat{u}_t$, pointing horizontally toward the target.

$$\begin{aligned} \sigma_h &= \frac{1}{1 + exp(G_{LR}(R_{t\,\mathrm{arg}} - R_{threshold}))} \\ \vec{u}_h &= \sigma_h \hat{u}_t \end{aligned} \tag{5–5}$$

5.2.1.2 Altitude Control

Altitude is controlled using a hyperbolic tangent (5–6) with an input offset to the desired flight altitude. The output, σ_{alt}, varies from -1 to 1 in a way that is opposite in sign to the altitude error in order to ellicit negative feedback control to the desired altitude. This response represents an approximately proportional control gain where the proportionality can be influenced by tuning the gain, G_{alt}. The output is multiplied by

a unit vector in the vertical direction ($\hat{u}_z$). The sum of the long range activation vector and the altitude control vector are normalized to obtain a long range navigation vector. This process, leading to the long range navigation vector, is represented in the following expressions.

$$\begin{aligned} \sigma_{alt} &= \frac{2}{1 + exp(G_{alt}(Z - Z_{desired}))} - 1 && (5\text{–}6) \\ \vec{u}_{alt} &= \sigma_{alt}\hat{u}_z \\ \hat{u}_{lr} &= \frac{\vec{u}_h + \vec{u}_{alt}}{\|\vec{u}_h + \vec{u}_{alt}\|_2} && (5\text{–}7) \end{aligned}$$

5.2.1.3 Obstruction Avoidance

The obstruction avoidance logic takes the difference between the rate of angular growth of the obstruction ($\frac{V_{perp}}{R_{obs}}$) and a threshold value ($K_{threshold}$) as an input to a sigmoid function (5–8). Angular growth rate of the obstruction is found by dividing the velocity component perpendicular to the obstruction by the range to the obstruction. The activation ranges from 0 to 1 as the threshold is passed. The sensitivity of the activation can be adjusted with the gain, G_{obs}. The value is multiplied times a horizontal unit vector ($\hat{r}_{obs}$) pointing away from the obstruction along the line-of-sight. The response to the closest three obstructions are added together so that an averaged response can be found when in close proximity to more than one obstruction.

$$\begin{aligned} \sigma_{obs} &= \frac{1}{1 + exp(-G_{obs}(\frac{V_{perp}}{R_{obs}} - K_{threshold}))} && (5\text{–}8) \\ \vec{u}_{obs} &= -\sigma_{obs}\hat{r}_{obs} && (5\text{–}9) \end{aligned}$$

5.2.1.4 Close Range Target Acquisition

As the fly approaches the target it passes a range threshold that simulates optical target acquisition. The activation function (σ_{sr}) rises from 0 to 1 as the threshold is

passed and is multiplied times a unit vector that is defined in such a way that it takes out LOS rate error. This is effectively a proportional navigation scheme , with a wide field-of-view sensor, could be implemented by keeping the target in the center of the optical flow field after accounting for body rotation rate. The unit vector required to take out the error is defined by first differencing the fly and target inertial velocities to obtain a relative velocity (5–10). The relative velocity is decomposed into components parallel to (5–11) and perpendicular to (5–12) the line-of-sight vector ($\hat{r}_{_{LOS}}$). A response proportional to the error is found by keeping the component of the relative velocity aligned with $\hat{r}_{_{LOS}}$ and changing the sign of the component perpendicular to the line-of-sight vector. After normalization this provides a unit vector use to command attitude control (5–13).

$$\Delta\vec{V} = \vec{V}_{fly} - \vec{V}_{tar} \tag{5–10}$$

$$\hat{r}_{_{LOS}} = \frac{\vec{P}_{tar} - \vec{P}_{fly}}{\left\|\vec{P}_{tar} - \vec{P}_{fly}\right\|_2}$$

$$\Delta\vec{V}_{parallel} = (\Delta\vec{V} \cdot \hat{r}_{_{LOS}})\hat{r}_{_{LOS}} \tag{5–11}$$

$$\Delta\vec{V}_{perp} = \Delta\vec{V} - \Delta\vec{V}_{parallel} \tag{5–12}$$

$$\hat{u}_{sr} = \sigma_{sr}\frac{\Delta\vec{V}_{parallel} - \Delta\vec{V}_{perp}}{\left\|\Delta\vec{V}_{parallel} - \Delta\vec{V}_{perp}\right\|_2} \tag{5–13}$$

5.2.1.5 Composite Control Vector

The final control vector is the normalization of the long range (5–7), obstruction avoidance (5–9), and close range (5–13) responses, where each response is gained using constant gains ($G_{_1}, G_{_2}, G_{_3}$)to establish the relative importance of the responses. Both the obstruction avoidance and close range target pursuit response are given a higher precedence through their gains than the long range flight control. This overwhelms the tendency to maintain altitude while in close proximity to the target.

Table 5-1. Nominal simulation parameters for the simulated insect.

Parameter	**Value**	**Units**
Species	Calliphora vicina	-
Mass	100	mg
Saccade Angle	< 50	deg
Saccade Duration	20-30 (3-4 wing beats)	ms
Max Angular Velocity	2000	deg/s
Max Angular Accel	1.2e05	deg/s/s
Roll Inertia	3.4e-10	kg m^2
Pitch Inertia	7.5e-10	kg m^2
Yaw Inertia	8.8e-10	kg/m^2
Max Horizontal Velocity (Cage)	1.2	m/s
Max Horizontal Velocity (Wind Tunnel)	2 to 3	m/s
Max Vertical Velocity (Cage)	0.8	m/s
Max Horizontal Acceleration	2	g
Max Vertical Acceleration	1	g

$$\hat{u}_{control} = \frac{G_1\vec{u}_{obs} + G_2\hat{u}_{lr} + G_3\hat{u}_{sr}}{\|G_1\vec{u}_{obs} + G_2\hat{u}_{lr} + G_3\hat{u}_{sr}\|_2} \tag{5–14}$$

5.2.2 Kinematic and Inertial Characteristics

The basic characteristics of the vehicle were derived from a dipteran species, *Calliphora vicina*, whose flight was characterized by Schilstra and van Hateren [53]. These parameters are summarized in Table 5-1. Observed wind tunnel maximum velocity (2 m/s) was used as opposed to the lower caged observation. The saccade, which is a rapid lateral change in flight direction, was not modeled explicitly, but was instead allowed to occur as an implicit part of the obstruction avoidance response.

5.2.3 Control Logic

The output of the decision logic is a direction to navigate toward. The output of the four activation inputs described are three unit vectors. These three competing navigation commands are weighted, combined and normalized to provide the final navigation direction, as described by (5–14). Errors with respect to this navigation vector are converted to a vector force and a torque commanded to orient the body. The resulting force acts in the presence of aerodynamic drag and gravity to push the fly toward

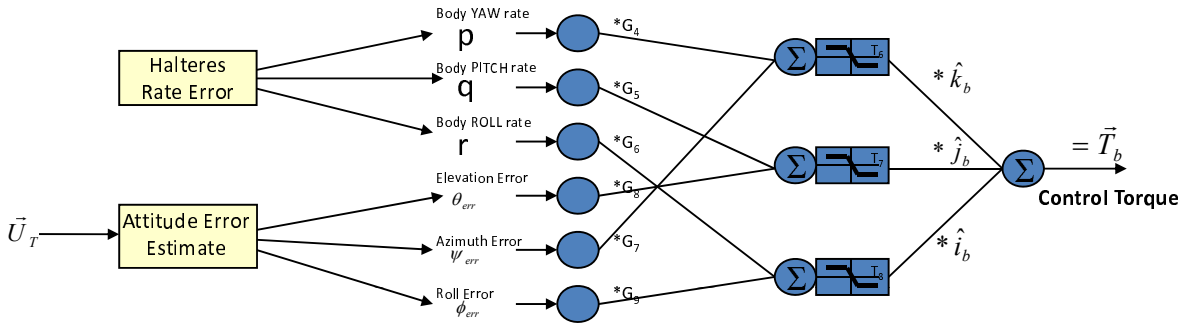

Figure 5-2. Attitude control logic is based on orientation errors with respect to the desired azimuth direction. Pitch and yaw errors are driven to zero. Control loop damping is proportional to the angular rates measured by the halteres.

the objective. Aerodynamic drag induced forces and torques are assumed to be quadratic functions acting parallel to the velocity and angular rate vectors, respectively.

The bottom of Figure 5-2 provides a depiction of the small error control logic. The logic represented is simply a proportional-derivative (PD) controller. If the azimuth error is below a user defined limit, then the three rotational degrees of freedom are controlled independently in proportion to the magnitude of the error in the orientation and the body rate. The body rates are assumed to be measured by the halteres and then gained and summed along with gained azimuth, elevation, and roll errors measured relative to the desired navigation direction. The overall objective of the simulation is to track along the navigation vector with a pitch and roll of zero and the commanded azimuth. To capture a reaction similar to the known saccadic response of insects, a simple bank-to-turn maneuver is also allowed. If the azimuth error is above the user defined limit, a bank-to-turn mode is entered. The simulated insect banks in proportion to the error up to a maximum bank angle and uses a combined pitch and yaw maneuver to reorient. To further simulate saccadic behavior, the insect maintains the flight path associated with the obstruction avoidance response for a short time, or until another obstruction causes a response, before resuming flight back toward the target. In both skid-to-turn and bank-to-turn modes the

proportional and derivative components are gained and sent through hyperbolic tangent functions that have been scaled to limit the maximum allowable torques.

Initial attitude control gains were chosen by treating each rotational axis independently as a 2nd order system. First, the maximum angular acceleration and moment of inertia determined the maximum achievable torque. Second, natural frequencies and damping ratios were selected. The natural frequency directly determined the proportional gain ($\omega_n^2 J$) and the combination of natural frequency and damping ratio determined the derivative gain ($2\zeta\omega_n J$). The parameters were chosen so that the maximum torque was balanced equally by control and aerodynamic damping torques at the maximum angular velocity.

The maximum linear forces were determined by the identified maximum linear accelerations and the mass of the vehicle. The maximum velocity was assumed limited by a drag force proportional to airspeed squared. A drag coefficient was therefore approximated as the ratio of maximum force to maximum velocity squared ($F_{\max}/V_{\max}^2$). Representative simulation parameters are summarized in Table 5-2.

5.2.4 Flight Environment

The simulated environment is a rectangular region 10 meters wide by 20 meters long with a upper boundary at 5 meters of altitude. If the vehicle leaves these boundaries the simulation is terminated. Within these boundaries a start point is identified on the ground and a target is identified. Obstructions can be placed anywhere within the boundaries. These obstructions are currently configured as cylindrical columns going from ground level to the upper boundary. A specific simulation configuration can be saved for re-execution or a new scenario can be randomly generated with varying numbers, sizes, and locations of cylinders. An example configuration is demonstrated in Figure 5-3.

5.3 Analysis Results

The analysis results are divided into four sections. The first two of these sections describe analysis completed to understand stability and control of an insect propelled and

Table 5-2. Example of derived simulation control parameters.

Derived Parameter	**Value**	**Units**
Max Force	0.002	N
Drag Coeff ($F_{\max}/V_{\max}^2$)	0.0005	N/(m/s)^2
Max Torque Roll	7.12e-07	N m
Max Torque Pitch	1.57e-06	N m
Max Torque Yaw	1.84e-06	N m
Natural Freq. Roll	5	Hz
Natural Freq. Pitch	5	Hz
Natural Freq. Yaw	5	Hz
Damping Coef Roll	0.5	-
Damping Coef Pitch	0.5	-
Damping Coef Yaw	0.5	-
Prop Gain Roll	3.36E-07	N m/rad
Prop Gain Pitch	7.40E-07	N m/rad
Prop Gain Yaw	8.69E-07	N m/rad
Rate Gain Roll	1.07E-08	N m/(rad/s)
Rate Gain Pitch	2.36E-08	N m/(rad/s)
Rate Gain Yaw	2.76E-08	N m/(rad/s)
Drag Coeff Roll	2.92E-10	N m/(rad/s)ˆ2
Drag Coeff Pitch	6.45E-10	N m/(rad/s)ˆ2
Drag Coeff Yaw	7.56E-10	N m/(rad/s)ˆ2

controlled by articulating wings. The motivation for these two sections is the limitation in force production fidelity provided in the 6DOF simulation. Ideal stroke averaged forces, equal to the commanded forces, are used by the simulation. Aerodynamic simulation of the complex unsteady flow associated with the wings was outside the scope of this effort. This simplification negates the need for a specific mechanism for control implementation and, therefore, implications of feedback pathways were ignored, whether ipsilateral or bilateral. To address these modeling limitations, separate analysis were performed for rate stabilization in the presence of cross-coupling and aerodynamic damping, and the implications of ipsilateral versus bilateral feedback.

The final two sections, 5.3.3 and 5.3.4, are associated with results from the 6DOF simulation. The control model in the 6DOF simulation assumes contralateral combination of the haltere output to obtain torques proportional to the angular rates. While ideally these torques could be applied exactly, some level of cross coupling will exist which will

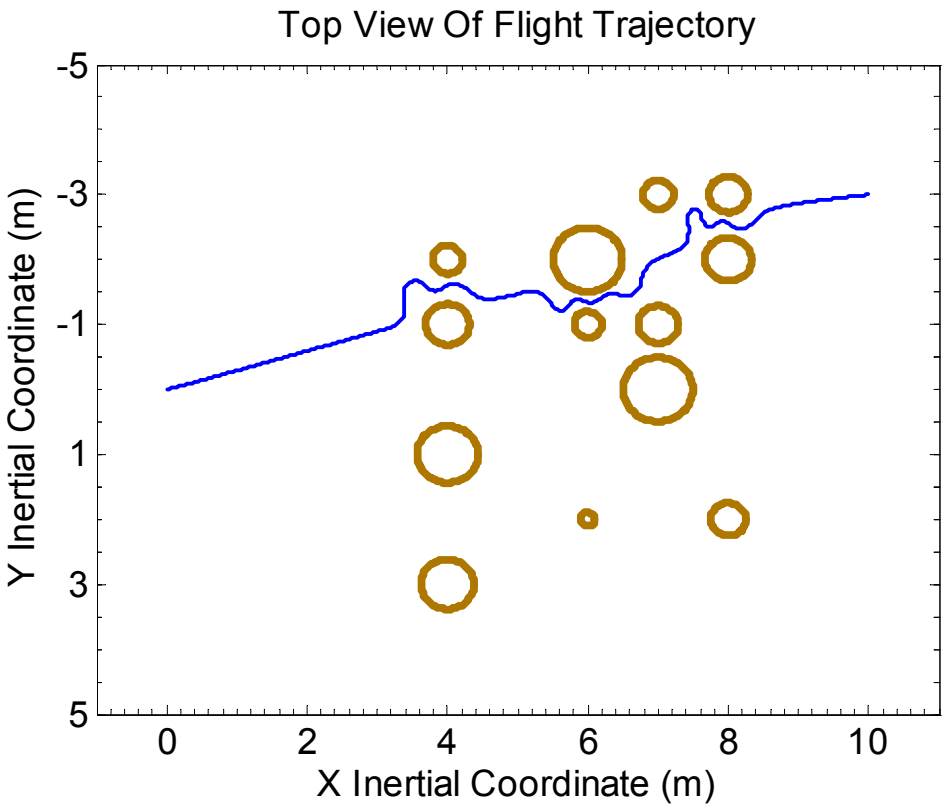

Figure 5-3. Nominal 6DOF test case shown from a top view perspective. Obstructions are place randomly in the form of vertical cylinders of randomly selected diameters. The flight path begins on the ground at the origin, with the target placed on the opposite end of the arena.

introduced torque disturbances that correlate with the desired control commands. The range of cross-coupling over which stability can be guaranteed is addressed in the first section. The next section addresses the issue of contralateral versus ipsilateral feedback. As described in the previous chapters, the literature indicates predominantly ipsilateral feedback to the flight control muscles. The implication of the non-orthogonality of the halteres and the control parameters chosen are demonstrated. The final two sections describe the results of the 6DOF simulation, demonstrating the ability of the halteres to track dynamic angular velocities using the encoding scheme described in Chapter 4 and the degree of fidelity at which saccades were replicated with respect to the measured data of Schlistra and Van Hateren [53].

5.3.1 Analysis of Torque Cross-Coupling on Insect Flight Stability

Insect 6DOF control requires kinematic manipulation of a number of wing parameters. For example, wing stroke amplitude can be used differentially to generate roll torque. Similarly, wing pronation can be used to induce a yaw torque and wing abduction can be used to control pitch. These control mechanisms can lead to varying levels of cross-coupling depending on the morphology described. For instance, wing pronation might cause a differential change in lift, resulting in a roll torque in addition to the desired yaw torque. To aid in understanding the degree of cross-coupling necessary to induce attitude instability, a bounding Lyapunov analysis was completed with and without aerodynamic rotational drag [71].

Euler equations for a rotating rigid body can be defined with respect to the principal axes as

$$\begin{aligned} J_1\dot{\omega}_1 &= (J_2 - J_3)\omega_2\omega_3 + u_1 \\ J_2\dot{\omega}_2 &= (J_3 - J_1)\omega_3\omega_1 + u_2 \\ J_3\dot{\omega}_3 &= (J_1 - J_2)\omega_1\omega_2 + u_3. \end{aligned} \tag{5–15}$$

In these expressions, ω_i, are the components of the angular velocity vector along the principal axes, u_i are the torque inputs applied about the principal axes, and J_i are the principal moments of inertia. The torque input can include both control terms, cross-coupling terms, and aerodynamic drag. To assess stability, a quadratic Lyapunov function is defined. The derivative of that function includes the dynamics equations defined by (5–15) and a torque input that includes control torques proportional to the state error ω. The characteristics of the Lyapunov function derivative determine the nature of the stability in the presence of cross-coupling and aerodynamic drag.

5.3.1.1 Stability Analysis with Proportional Control

A scalar positive definite Lyapunov function is defined along with its derivative as

$$V = \frac{1}{2}\omega^T J\omega, \text{ and} \tag{5–16}$$

$$\dot{V} = \omega^T J\dot{\omega} \tag{5–17}$$

In these expressions, J is a constant inertia matrix and ω is defined with respect to principal axes, therefore,

$$J = \begin{bmatrix} J_1 & 0 & 0 \\ 0 & J_2 & 0 \\ 0 & 0 & J_3 \end{bmatrix}. \tag{5–18}$$

Substitution of $J\dot{\omega}$ from (5–15) into the Lyapunov derivative gives

$$\begin{aligned} \dot{V} &= \omega^T \begin{bmatrix} (J_2 - J_3)\omega_2\omega_3 \\ (J_3 - J_1)\omega_3\omega_1 \\ (J_1 - J_2)\omega_1\omega_2 \end{bmatrix} + \omega^T u \\ &= \omega^T u. \end{aligned} \tag{5–19}$$

Defining u as proportional to ω gives

$$u = -K\omega = -\begin{bmatrix} k_1 & 0 & 0 \\ 0 & k_2 & 0 \\ 0 & 0 & k_3 \end{bmatrix} \omega, \tag{5–20}$$

which provides a negative definite result with no extraneous forces. Based on (5–16), (5–19) and (5–20), the following inequality can be developed:

$$\begin{aligned} \dot{V} &= -\omega^T K\omega \\ &\leq -k_{\min}\omega^T\omega \\ &\leq -\frac{2k_{\min}}{J_{\max}}V. \end{aligned} \tag{5–21}$$

A globally exponentially stable result can be developed from 5–16 and 5–21 as

$$\omega(t) \leq \omega(0) e^{-\frac{k_{\min}}{J_{\max}} t}.$$

5.3.1.2 Stability Analysis with Proportional Cross Coupling

Assuming the cross-coupling terms are to a first order linear, the applied control torque with cross coupling could be represented as

$$\begin{aligned} u &= -K\omega + C\omega \\ &= -\begin{bmatrix} k_1 & 0 & 0 \\ 0 & k_2 & 0 \\ 0 & 0 & k_3 \end{bmatrix} \omega + \begin{bmatrix} 0 & c_{12} & c_{13} \\ c_{21} & 0 & c_{23} \\ c_{31} & c_{32} & 0 \end{bmatrix} \omega, \end{aligned} \tag{5–22}$$

where, k_i are defined as real positive constants, and c_{ij} are defined as real constants that may be positive or negative. In this case, the Lyapunov derivative becomes

$$\begin{aligned} \dot{V} &= -\omega^T K\omega + \omega^T C\omega \\ &= -\omega^T (K - C)\omega. \end{aligned} \tag{5–23}$$

As long as $(K - C)$ is positive definite, then the solution is guaranteed to be exponentially stable. To be positive definite, the eigenvalues of $(K - C)$ must all be positive which is true only if all the leading principal minors are positive. Looking at the bounding case defined by the minimum control gain and the maximum cross coupling coefficient, where $k_i = k = k_{\min}$ and $c_{ij} = c = c_{\max}$, then

$$u = -\begin{bmatrix} k & 0 & 0 \\ 0 & k & 0 \\ 0 & 0 & k \end{bmatrix} \omega + \begin{bmatrix} 0 & c & c \\ c & 0 & c \\ c & c & 0 \end{bmatrix} \omega, \text{ and} \tag{5–24}$$

$$\dot{V} = -\omega^T \begin{bmatrix} k & -c & -c \\ -c & k & -c \\ -c & -c & k \end{bmatrix} \omega. \tag{5–25}$$

For $\dot{V}$ to be negative definite, then the gain and cross-coupling matrix must be positive definite, requiring

$$\begin{aligned} k &> 0 \\ k^2 - c^2 &> 0 \\ k^3 - 2c^3 + 3kc^2 &> 0. \end{aligned} \tag{5–26}$$

This first term is true by definition. The second term indicates that the magnitude of the minimum control gain must be greater than the maximum magnitude of the cross coupling terms. The third term can be represented in terms of a ratio of coupling coefficient to control gain as

$$1 - 2\left(\frac{c}{k}\right)^3 - 3\left(\frac{c}{k}\right)^2 > 0. \tag{5–27}$$

The plot in Figure 5-4 demonstrates that peak stability occurs when there is no cross-coupling and provides evidence that as long as the ratio of the largest magnitude cross coupling term to the minimum gain eigenvalue is less than 0.5, asymptotic stability should be obtainable.

5.3.1.3 Stability Analysis with Drag and Cross Coupling

The stability analysis is now extended to include rotational drag in addition to externally applied forces. The drag is assumed to be a torque in the opposite direction of the rate vector, but proportional to the magnitude squared of the rate vector. That is,

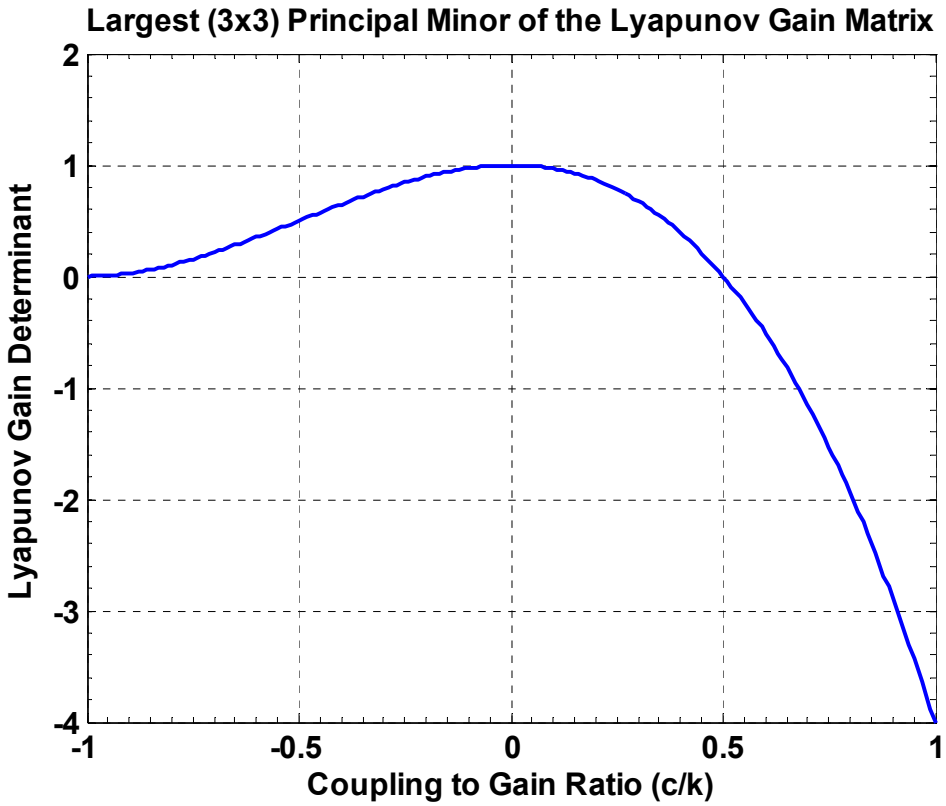

Figure 5-4. Plot demonstrating the range over which the Lyapunov derivative is negative definite. In the range where the principle minors of the gain matrix are all positive the Lyapunov derivative is negative definite.

$$\begin{aligned} angular \;\; drag &= -D\,|\omega|^2\,\frac{\omega}{|\omega|} \\ &= -D\,|\omega|\,\omega. \end{aligned} \tag{5–28}$$

Therefore, the forcing function impacting rotational dynamics can be defined as

$$u = -K\omega + C\omega - D\,|\omega|\,\omega, \tag{5–29}$$

where D is assumed to be a diagonal matrix of positive coefficients associated with each axis. The term $D\,|\omega|$ adds stability to the system. The constant positive diagonal terms of the K matrix are now supplemented with terms that are proportional to the magnitude

of ω. If a conservative, bounding definition of the drag coefficients is used, as defined by $d_i = d_{\min} = d$, then the applied torques and the associated Lyapunov derivative can be defined as

$$u = -\begin{bmatrix} k & 0 & 0 \\ 0 & k & 0 \\ 0 & 0 & k \end{bmatrix} \omega + \begin{bmatrix} 0 & c & c \\ c & 0 & c \\ c & c & 0 \end{bmatrix} \omega - \begin{bmatrix} d\,|\omega| & 0 & 0 \\ 0 & d\,|\omega| & 0 \\ 0 & 0 & d\,|\omega| \end{bmatrix} \omega, \text{ therefore} \quad (5\text{–}30)$$

$$\dot{V} = -\omega^T \begin{bmatrix} k + d\,|\omega| & -c & -c \\ -c & k + d\,|\omega| & -c \\ -c & -c & k + d\,|\omega| \end{bmatrix} \omega. \quad (5\text{–}31)$$

Following the same process as before, for $\dot{V}$ to be negative definite, then the gain and cross-coupling matrix must be positive definite requiring

$$\begin{aligned} k + d\,|\omega| &> 0 \\ (k + d\,|\omega|)^2 - c^2 &> 0 \\ (k + d\,|\omega|)^3 - 2c^3 + 3(k + d\,|\omega|)c^2 &> 0. \end{aligned} \quad (5\text{–}32)$$

This first term is true by definition. The second term indicates that the magnitude of the minimum control gain plus the minimum drag coefficient must be greater than the maximum magnitude of the cross coupling terms. The third term can be represented in terms of a ratio of coupling coefficient to control gain as

$$1 - 2\left(\frac{c}{k + d\,|\omega|}\right)^3 - 3\left(\frac{c}{k + d\,|\omega|}\right)^2 > 0. \quad (5\text{–}33)$$

A plot of this expression is not provided since it would be identical to that Figure 5-4, with the ordinate defined as $\left(\frac{c}{k+d|\omega|}\right)$ instead of $\left(\frac{c}{k}\right)$.

5.3.1.4 Stability Analysis Conclusion

The analysis provided is approximate, but reinforces intuitive understanding of the flight stability for a system with articulating wings. In a real system, controlled by kinematic variations of the wing stroke, significant coupling between axes is expected. Combinations of wing pronation/supination, stroke amplitude, and adduction/abduction might be used to generate torques around the pitch, yaw and roll axes. The above analysis demonstrates that within the validity of the assumptions, stability should remain exponential as long as the cross coupling terms are bounded and the magnitudes of the cross-coupling coefficients remain below approximately one half of the proportional control gains. The addition of viscous drag, proportional to the angular rate squared will only enhance stability. Relative to the constant control gains, the viscous gain will increase in proportion to the magnitude of the angular rate vector.

5.3.2 Contralateral Versus Ipsilateral Expression of Wing Control

In the previous section, the ability to generate torques around the center of gravity is assumed and the level of cross-coupling allowable, while still maintaining stability, was addressed. The relationship between measured rate errors generated by the halteres and the wing kinematic response that creates stabilizing torques was ignored. The mechanisms by which insects might generate control forces are investigated in this section in relation to the source of the feedback control signal, whether purely ipsilateral or a signal that represents a bilateral combination from both halteres. In a man-made system, bilateral combination of the haltere measurements can be assumed, so a rate vector in the body frame would be available to calculate differential control commands for the wings. In insects, experimental data indicates that haltere influence is predominantly ipsilateral. Both of these cases are investigated within the assumption that wing forces at a fixed mean center of pressure can be modulated independently by control of wing amplitude and pronation at a fixed stroke frequency. With these two forces, roll and yaw moments can be generated. Pitch moment is assumed to be generated in one of two ways, first by

controlling the abduction angle of the wing, thereby controlling the location of the center of pressure relative to the body center of gravity, and second, by generating a net twisting moment during the stroke.

Figure 5-5 shows the assumed wing stroke geometry. For simplicity the average center of pressure is assumed to exist in a plane that includes the center of gravity of the body. The net force generated by the wings acts through the center of pressure and is broken into two components that are independently controllable. The first is in the x-direction, possibly generated by wing pronation, and the second is in the z-direction, controlled with wing amplitude. Forces from the two wings in the y-direction are assumed to be in opposite directions with approximately equal force so that the net effect on the body is ineligible. The wing stroke and the abduction angle are defined to be in the xy-plane as if the insect were hovering.

5.3.2.1 Wing Kinematics with Contralateral Influence

Nomenclature.

Table 5-3 provides definitions of the symbols used in the described results. Note in reviewing the described results that the control gains, (K_x, K_y, K_z), η, L, w, and α_0 are all constants.

Control Force Derivation.

Contralateral feedback allows for combination of the output of the two halteres prior to control response. Due to the non-orthogonal orientation of the two halteres, the lateral rate components must be combined in a very specific manner to reconstruct pitch and roll body rates. For pitch, a differencing operation must be performed and, for roll, a summation. The required gains depend both the control gain and trigonometric functions of the angle that defines the haltere stroke plane. The contralateral availability of these measurements effectively implies the availability of the body rates (p, q, r) for direct use in generation of the control forces and abduction control deviation. Additionally, availability of the body rates allows for symmetric generation of control commands so that the desired

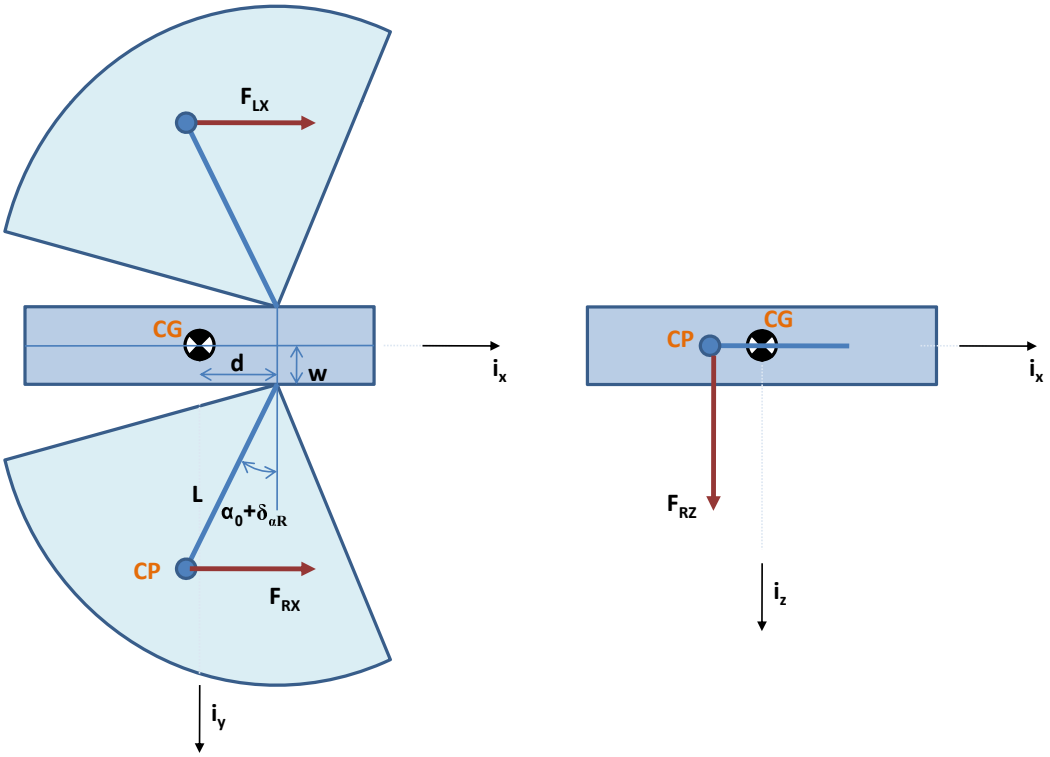

Figure 5-5. Diagram demonstrating the geometric configuration associated with wing kinematic analysis. Control parameters are the right and left forces in the x-direction (F_{Rx}, F_{Lx}), in the z-direction (F_{Rz}, F_{Lz}), and the abduction angle deviation $\delta_{\alpha R}, \delta_{\alpha L}$. The forces act through the average wing stroke center of pressure (CP) and torques are calculated with respect to the center of gravity (CG).

nominal forces are exactly maintained while achieving the necessary control torques. The result for the control commands as a function of body rate and wing geometry is

$$\delta_\alpha \approx \frac{-K_y q}{F_{zd} L \cos(\alpha_0)} \tag{5–34}$$

$$\Delta F_{Rz} = \frac{-K_x p}{2(w + L\cos(\alpha_0 + \delta_\alpha))} \tag{5–35}$$

$$\Delta F_{Rx} = \frac{K_z r}{2(w + L\cos(\alpha_0 + \delta_\alpha))} \tag{5–36}$$

$$\Delta F_{Lx} = -\Delta F_{Rx} \tag{5–37}$$

$$\Delta F_{Lz} = -\Delta F_{Rz}. \tag{5–38}$$

Table 5-3. Parameter definitions for wing kinematic control expressions.

Symbol	Definition
$\vec{T}_R, \vec{T}_L$	: right and left torques around the center of gravity (CG)
$\vec{R}_R, \vec{R}_L$	: position vectors from CG to the center of pressure (CP)
$\vec{F}_R, \vec{F}_L$	: right and left forces through the CP
p, q, r	: rate components in the body frame
F_{xd}, F_{yd}, F_{zd}	: desired nominal forces on the body
$\Delta F_{R\#}, \Delta F_{L\#}$	: difference between half desired body force and actual wing force
K_x, K_y, K_z	: control gains
η	: haltere stroke plane angle relative to lateral, (same as α from Chapter 3)
L, w	: hinge offsets relative to the center of gravity
$\alpha_0, \delta_{\alpha R}$	: nominal wing abduction angle and control deviation
Ω_{b1}, Ω_{b3}	: right haltere vertical and lateral measurements
Ω_{c1}, Ω_{c3}	: left haltere vertical and lateral measurements

The derivation of these expressions is included in Appendix C. Summation of the forces and torques around the center of gravity gives the result,

$$T_x = -K_x p \tag{5–39}$$

$$T_y = -K_y q \tag{5–40}$$

$$T_z = -K_z r \tag{5–41}$$

$$F_x = F_{xd} \tag{5–42}$$

$$F_y = 0 \tag{5–43}$$

$$F_z = F_{zd}. \tag{5–44}$$

In these expressions F_{xd} and F_{zd} are the forces obtained from the control logic described by Figure 5-1 and then applied in the body frame as if there was zero attitude error. The torques shown in (5–39)-(5–41) are the desired stabilizing response proportional to the rates expressed in the body frame. Since the control forces deviations associated with rate errors were required to be equal an opposite for the derivation of Section C.1,

equations (5–39)-(5–44) simply confirm the expected result. In the following two sections, where contralateral influence of the halteres is not assumed, the requirement for equal and opposite control force responses cannot be enforced.

5.3.2.2 Ipsilateral Haltere Influence with Abduction as a Control Parameter

The assumption of contralateral influence of the haltere measurements allowed for symmetry in the commanded control forces and identical abduction angles, which in turn resulted in simpler control formulation and no error in summed medial plane forces relative to the desired forces. The following results eliminate these simplifications, but still use abduction angle as a control parameter. This result, with only ipsilateral feedback, better matches what is understood about nature, with each haltere predominantly influencing the kinematics of the wing on its ipsilateral side.

The resulting expressions, as derived in Appendix C, for the control parameters are

$$\delta_{\alpha R} \approx \frac{C_1\Omega_{b3}}{C_2\Omega_{b3} - C_3F_{zd}} \tag{5–45}$$

$$\delta_{\alpha L} \approx \frac{C_1\Omega_{c3}}{C_2\Omega_{c3} + C_3F_{zd}} \tag{5–46}$$

$$\Delta F_{Rx} = -C_4\Omega_1 \tag{5–47}$$

$$\Delta F_{Lx} = C_4\Omega_1 \tag{5–48}$$

$$\Delta F_{Rz} = C_5\Omega_{b3} \tag{5–49}$$

$$\Delta F_{Lz} = -C_5\Omega_{c3}, \text{ where} \tag{5–50}$$

$$C1 = K_y \sin(\eta)(w + L\cos(\alpha_0)) \tag{5–51}$$

$$C2 = (K_y \sin(\eta)\sin(\alpha_0) - K_x\cos(\eta)\cos(\alpha_0))L \tag{5–52}$$

$$C3 = \sin(\eta)(w + L\cos(\alpha_0))\cos(\eta)\cos(\alpha_0)L \tag{5–53}$$

$$C4 = \frac{K_z}{2(w + L\cos(\alpha_0 + \delta_{\alpha R}))} \tag{5–54}$$

$$C5 = \frac{K_x}{2\sin(\eta)(w + L\cos(\alpha_0 + \delta_{\alpha R}))}. \quad (5\text{–}55)$$

Looking at one of the expressions for the control angle, two limiting cases can be evaluated. First, if the denominator term involving the lift force is large with respect to the term involving the lateral rate measurement then

$$\delta_{\alpha R} \approx \frac{-K_y \Omega_{b3}}{F_{zd}\cos(\eta) L\cos(\alpha_0)} = Const \cdot \frac{\Omega_{b3}}{F_{zd}}. \quad (5\text{–}56)$$

The control angle is proportional to the lateral rate measurement and inversely proportional to the lift force. In affect, this has already been assumed when $\delta_{\alpha R}$ was assumed to be a small angle. If the lift force were small then

$$\delta_{\alpha R} \approx \frac{K_y \sin(\eta)(w + L\cos(\alpha_0))}{K_x \cos(\eta) L\cos(\alpha_0)} = Const. \quad (5\text{–}57)$$

In this case the control angle becomes a constant, dependent on the haltere set back angle and the control gains. Since the haltere set back angle is not small, the situation where the control force is large relative to the lift force would contradict the small angle assumption.

Summing the forces and torques gives

$$F_x \approx F_{xd} \quad (5\text{–}58)$$

$$F_y \approx 0 \quad (5\text{–}59)$$

$$F_z = F_{zd} + \Delta F_{Rz} + \Delta F_{Lz} \quad (5\text{–}60)$$

$$T_x = -K_x p \quad (5\text{–}61)$$

$$T_y = -K_y q \quad (5\text{–}62)$$

$$T_z = -K_z r. \quad (5\text{–}63)$$

Unlike the case where contralateral feedback was allowed and symmetry of the control forces enforced, in this case the net force in the z-direction is not exactly the desired force. There are cases, for example, where the rate vector is unobservable by one of

the non-orthogonal halteres but observable by the other. This would result in a control response, ΔF_z, on one side only.

5.3.2.3 Ipsilateral Haltere Influence with Aerodynamic Wing Moment as a Control Parameter

The third case examined uses control over the average aerodynamic moment on the wing to induce pitch control. This would be implemented by rapid reversal of the wing stroke at the beginning or end of the stroke, forcing the wing to rotate against aerodynamic resistance. In this mode of operation the wing would maintain a constant abduction angle intended to maintain zero rotation during undisturbed flight.

The control parameters are derived in Appendix C. The expressions for control forces and moments are summarized here as

$$\Delta F_{Rz} = K_x \cdot \frac{\Omega_{b3}}{2\sin(\eta)(w + L\cos(\alpha_0))} \tag{5–64}$$

$$\Delta F_{Lz} = -K_x \cdot \frac{\Omega_{c3}}{2\sin(\eta)(w + L\cos(\alpha_0))} \tag{5–65}$$

$$M_R = -K_y \cdot \frac{\Omega_{b3}}{2\cos(\eta)} \tag{5–66}$$

$$M_L = K_y \cdot \frac{\Omega_{c3}}{2\cos(\eta)} \tag{5–67}$$

$$\Delta F_{Lx} = K_z \cdot \frac{\Omega_1}{2(w + L\cos(\alpha_0))} \tag{5–68}$$

$$\Delta F_{Rx} = -K_z \cdot \frac{\Omega_1}{2(w + L\cos(\alpha_0))}. \tag{5–69}$$

The summed forces and moments are the same as the previous case,

$$F_x \approx F_{xd} \tag{5–70}$$

$$F_y \approx 0 \tag{5–71}$$

$$F_z = F_{zd} + \Delta F_{Rz} + \Delta F_{Lz} \tag{5–72}$$

$$T_x = -K_x p \tag{5–73}$$

$$T_y = -K_y q \tag{5–74}$$

$$T_z = -K_z r. \tag{5–75}$$

Once again, the lack of contralateral influence eliminates the possibility of creating a symmetry constraint on the control forces to ensure the net force in the z-direction is equal to the desired force.

5.3.3 6DOF Results Comparing Haltere Measurements with Truth

The results of the previous section demonstrated that the net control torques can be equivalent with or without contralateral influence of the haltere output. The predominant difference between the two approaches is the net force in the z-direction, different from desired by the sum of the left and right z-forces. For the purpose of the presented 6DOF simulation results, the forces and torques on the insect were generated as if bilateral combination were allowed, as expressed in (5–39)-(5–44). Differences between actual and desired z-force which showed up in (5–58)-(5–63) and (5–70)-(5–75) were assumed to be small and based on the robustness demonstrated in the Lyapunov analysis, the implication to stability was assumed to be negligable. The haltere model consisted of a full non-linear representation of both halteres attached to the body of the fly such that the setback of the oscillation plane was at a fixed angle of 30 deg. The haltere oscillation frequency was 150 Hz, damping was assumed to be critical and the out-of-plane natural frequency was 300 Hz. Muscular response to the halteres was modeled as a first order response with a time constant equal to the oscillation period of the wings/halteres.

Figure 5-6 demonstrates the difference between the actual and measured body rates during the period between 2 to 4 seconds. This time period captures some of the most dynamic flight activity of the simulated insect. The measured body rates are found by taking the output of both halteres and, after decoding in accordance with (4–6) and (4–7), combining them in accordance with (4–3) through (4–5). These measured quantities are scaled using approximate calibration constants found by forcing the simulated insect to

move with known angular rates. The inaccuracy in this process can be thought of as uncertainty in the feedback control gains. The non-observability of small scale oscillations directly follows from the discrete sampling associated with placement of the approximately 100 sensilla in the dF2 field on the halteres. Figure 5-7 demonstrates the quantization effects and resulting motion during the initial pitch transient in the flight. Less than critical damping at the lower rates allows for the oscillation at the attitude loop natural frequency observed in Figure 5-7.

The halteres effectively provide an inner rate stabilization loop, damping the dynamics associated with tracking the navigation and end-game target homing solution. The active damping associated with the halteres is supplemented by passive aerodynamic damping proportional to the square of the angular rate. In the simulation, these damping components were calibrated to equally contribute to a damping torque, at the experimentally determined maximum angular velocity, that equaled the maximum torque achievable by the wings. This equivalence at the maximum angular rate requires that, due to its quadratic nature, the passive damping component provides an increasing lower proportion of the damping force at lower angular velocities. Figure 5-8 demonstrates the relative proportions of the damping forces.

A test case was executed with only the assumed level of aerodynamic damping to demonstrate the significance of loss of active rate feedback. Figure 5-10 represents the translational and attitude time history, both with and without rate damping. The results demonstrate both a markedly different trajectory resulting from the timing of the non-linear obstruction avoidance responses and the "noisier" attitude dynamics resulting from an underdamped response of the attitude loop.

5.3.4 6DOF Obstruction Avoidance and Saccade-Like Maneuvers

To investigate the ability to replicate saccade-like behavior using the simple constructs embodied in the 6DOF simulation, a rudimentary bank-to-turn reaction was implemented. Since the desired, averaged effect of aerodynamic forces is assumed

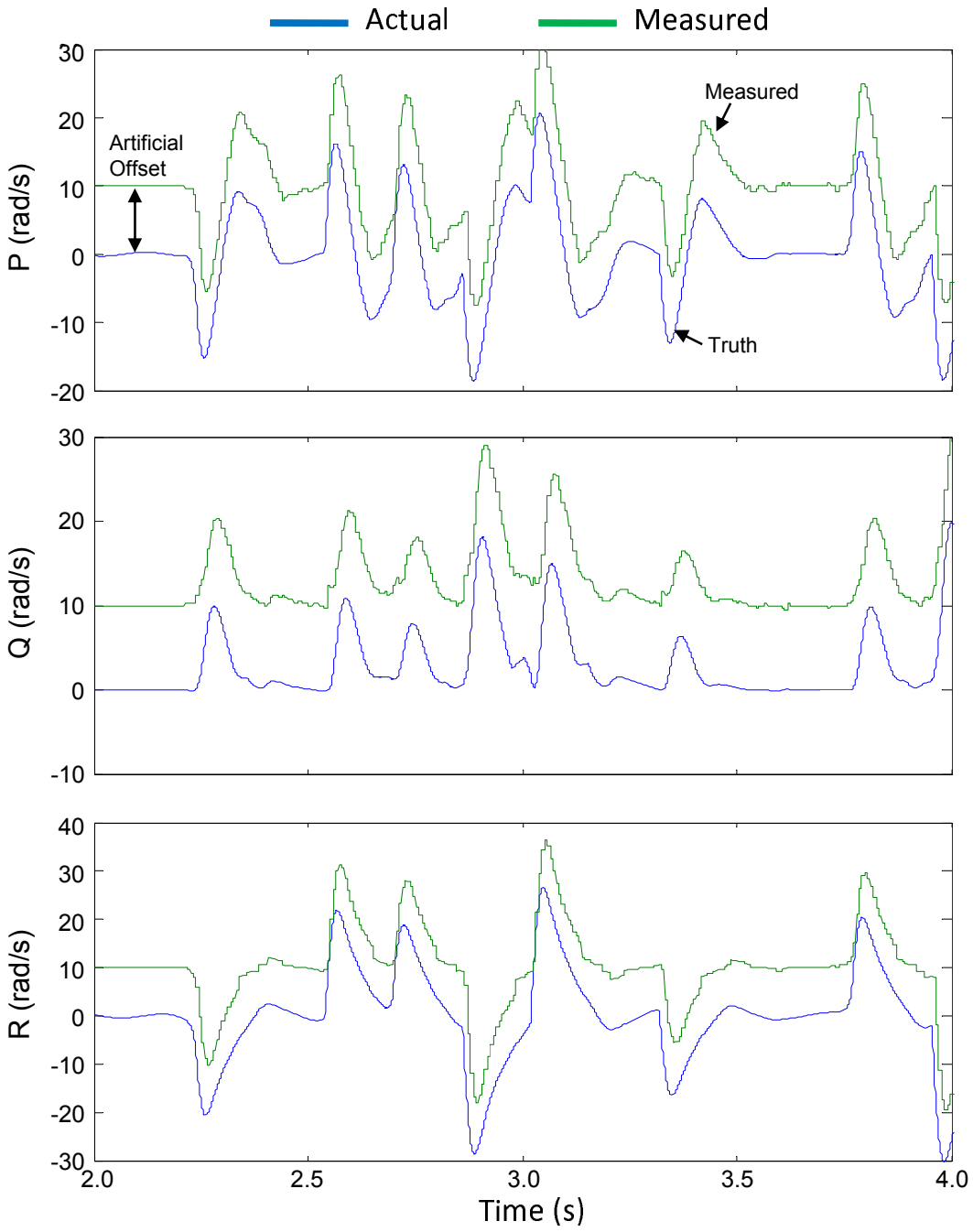

Figure 5-6. Angular velocity component time history with respect to the body roll, pitch, and yaw axes (x,y,z). These are commonly referred to as p, q, and r, respectively. The curves derived from haltere measurements are artificially offset by 10 rad/s. The true values appear more continuous, while the values derived from haltere measurements show artifacts of sensilla quantization, cross-coupling, and haltere dynamic limitations.

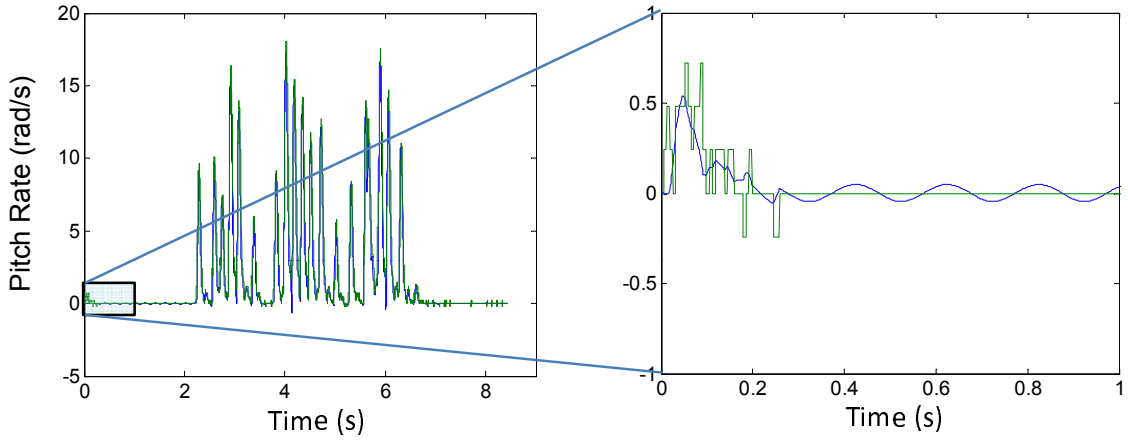

Figure 5-7. Expanded view of true pitch rate and modeled haltere estimate of the pitch rate. The initial transient occurs due to a step change in state error at the beginning of the simulation.The expanded plot on the right demonstrates haltere errors due to both dynamics and encoding. Limited measurement resolution results in unobservable rate dynamics.

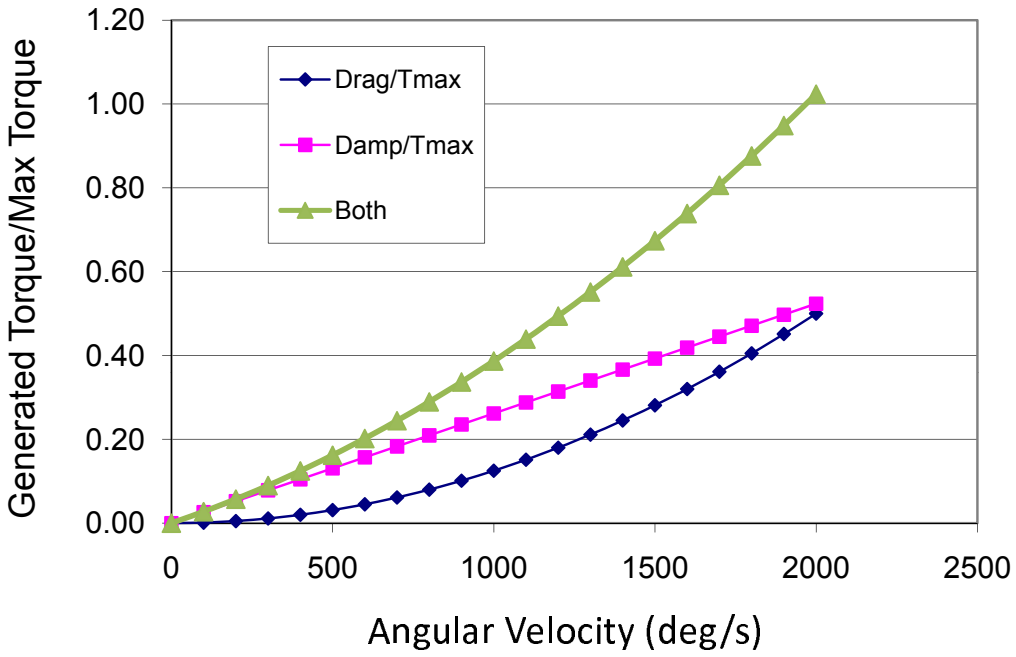

Figure 5-8. The relationship between stabilizing torque and angular velocity. By design the combination of passive and active damping torques equal the maximum acheivable wing torque at 2000 deg/s, constraining the vehicle to remain below that level.

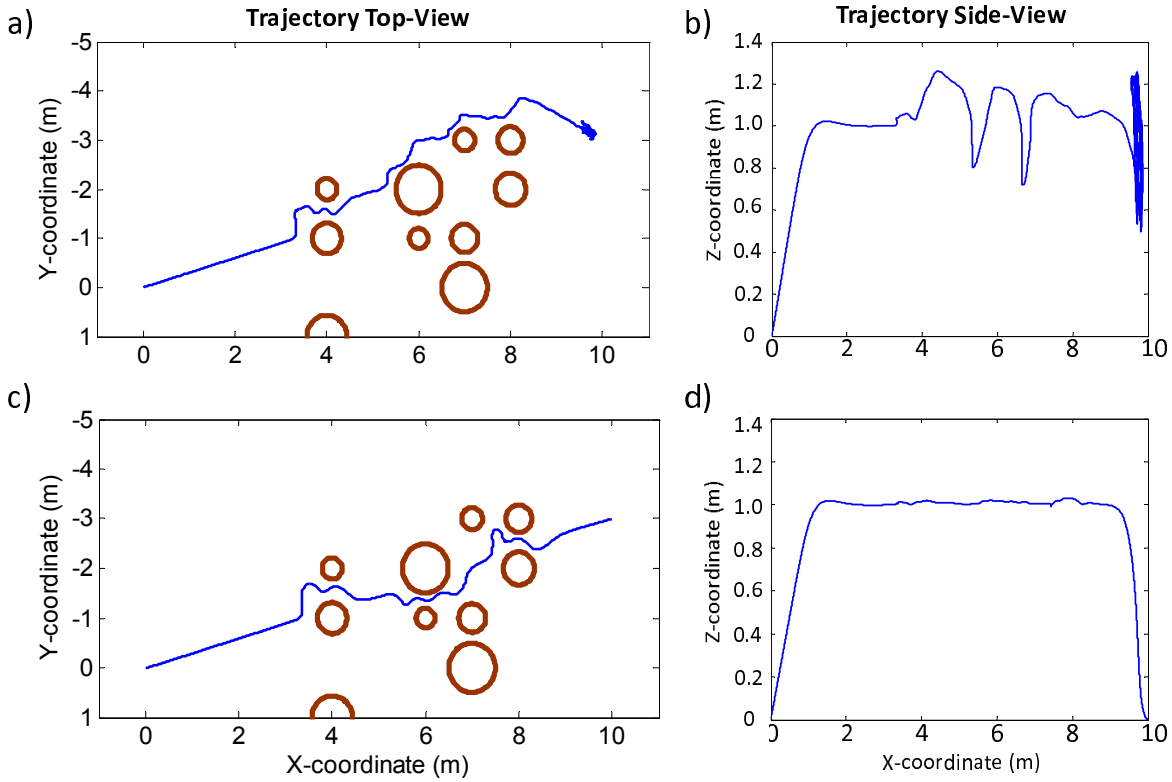

Figure 5-9. Comparison of flight paths with and without haltere feedback. Inset plots show the altitude. The plot on top shows the trajectory with only passive aerodynamic damping. The plot on the bottom shows the trajectory with both active and passive rate stabilization.

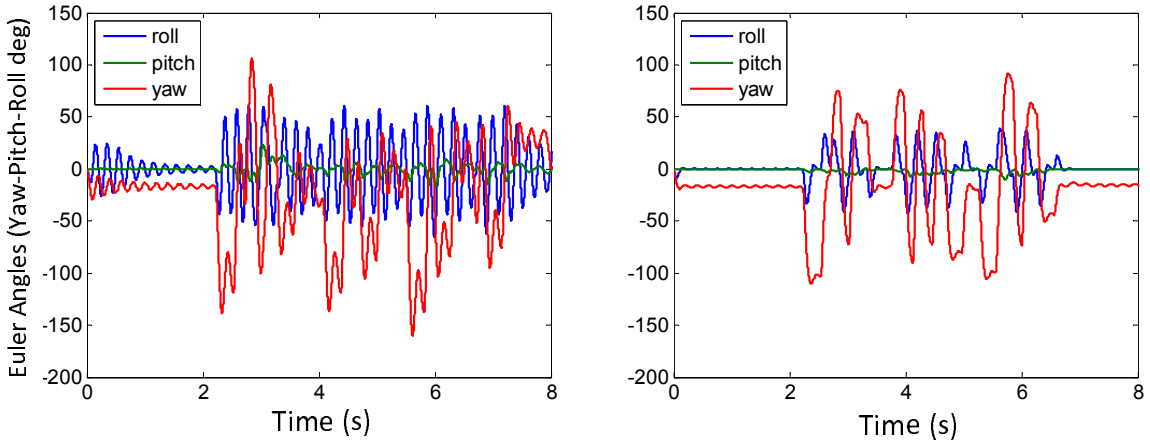

Figure 5-10. Comparison of Euler angles without (left) and with (right) haltere feedback. Haltere damping is 50% of critical. Aero-damping is 50% of critical at 2000 deg/s.

without a detailed model of time-varying aerodynamic force, the ability to capture all the salient features of obstruction avoidance is limited. The 6DOF simulation models aerodynamic drag, but does not account for the actual geometry of the fly. The basic bank-to-turn model representation commands the fly's roll orientation in proportion to magnitude of the heading error, including the influence of obstruction avoidance. To approximate the resulting effect of aerodynamic planform along with active reorientation torques, a combination of pitch and yaw torques in the fly's body frame are applied. These pitch and yaw torques are calculated based on the roll angle so that the net torque causes a reorientation in the horizontal plane if the roll angle is estimated accurately. As the heading error decreases, the commanded roll decreases and, likewise, the reorientation torque decreases. Figures 5-11 and 5-12 demonstrate the obstruction avoidance maneuver with two different assumption for roll estimation. In Figure 5-11 the assumption is that the reorientation torque is intrinsically derived as if a reflexive response based on the desired roll orientation. This mode has the potential to introduce large out-of-plane motions due to large errors in roll orientation. In the second figure, Figure 5-12, the assumption is that the actual roll orientation is directly measured optically, through wing loading or through some other form of estimation, allowing for minimization of out-of-plane motion.

For comparison the work of Schilstra and Van Hateren was used as shown in Figure 5-13 [53]. This work shows averages for a large number of observations and includes attitude defined in terms of a yaw-pitch-roll inertial to body transformation and angular velocity and acceleration defined with respect to the fly body system.

5.4 Discussion

This chapter touches upon a broad range of phenomena including both flight control and behavioral response. Derivations of several potential kinematic flight control mechanisms for an insect with a single pair of wings were provided, formalizing the general discussions of Taylor [65] with the additional generalization of ipsilateral versus

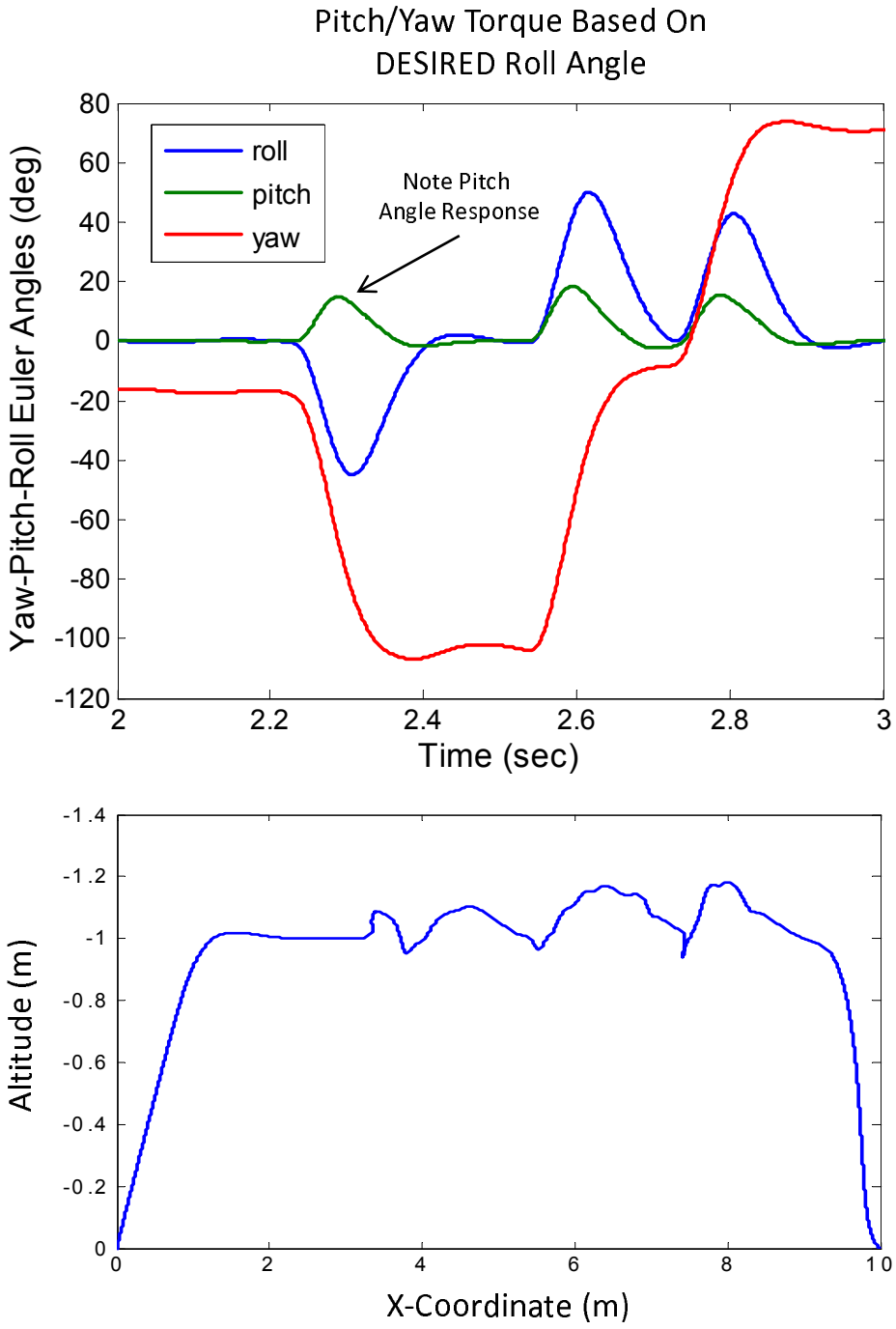

Figure 5-11. Obstruction avoidance response based on desired roll angle. This method of determining body torques leads to significant response of the pitch Euler angle. The plot of altitude also shows significant deviations from level flight.

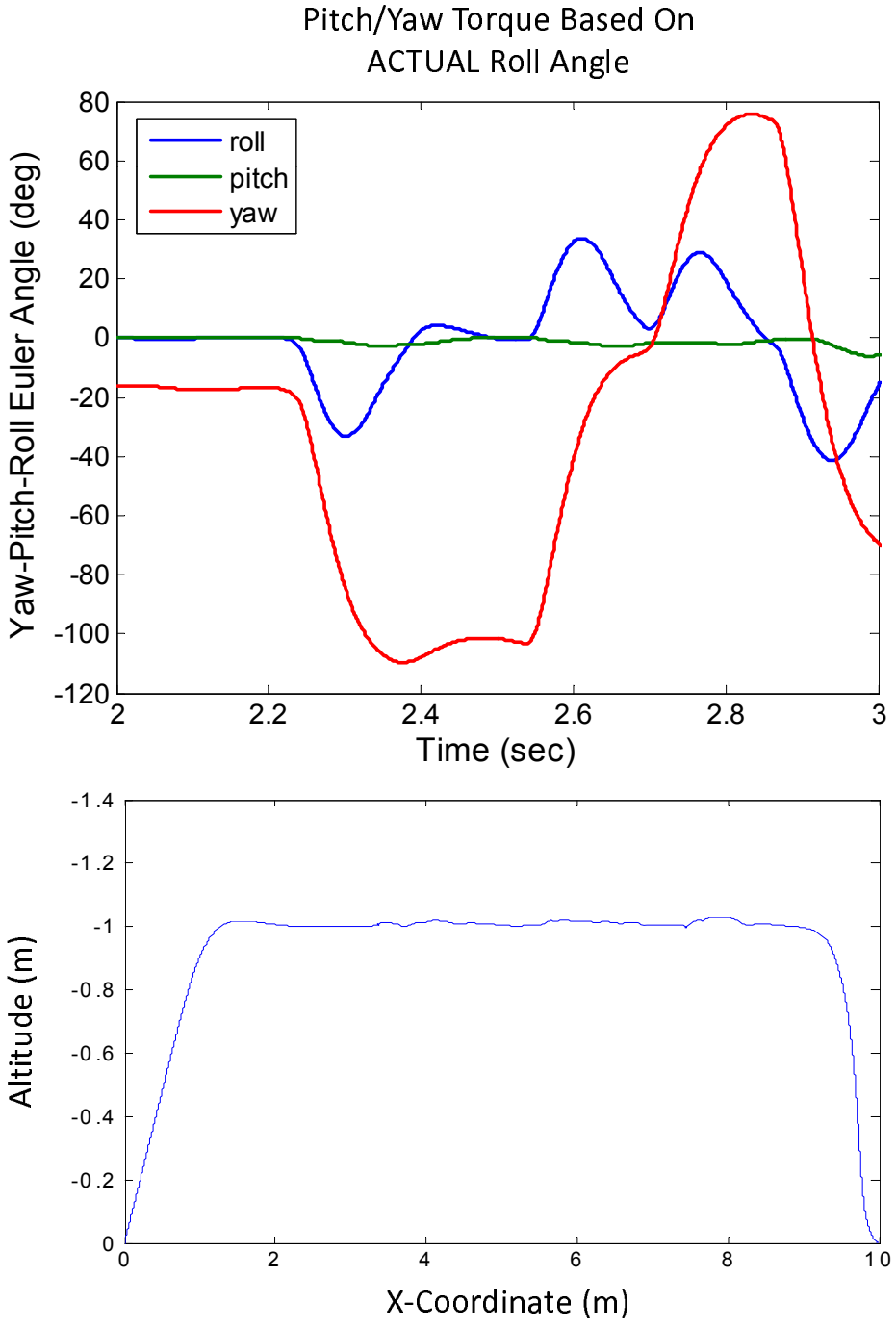

Figure 5-12. Obstruction avoidance response based on actual roll angle. This method of determining body torques leads to lower deviation of the pitch Euler angle from nominal. The plot of altitude shows minimal variation from level flight.

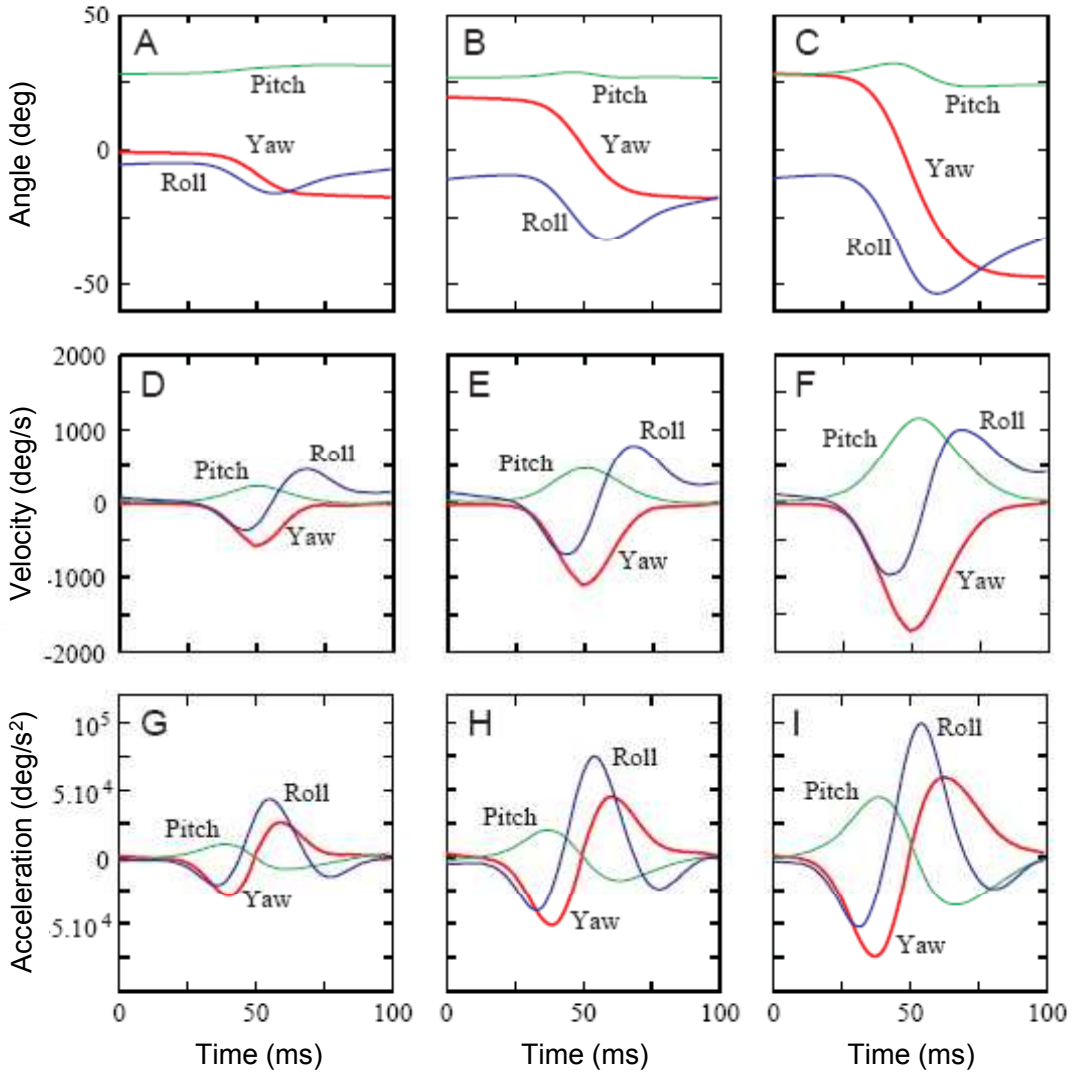

Figure 5-13. Measured saccade results from Schilstra and Van Hateren, 1999. Averages of saccades from 10 flies showing a yaw change (yaw, pitch, roll Euler angles) to the left, with a magnitude of 10-20° (1217 saccades, A, D, G), 30-40° (946 saccades, B, E, H) and 60-90° (677 saccades, C, F, I).

contralateral feedback. These specific derivations only covered a couple of the possible control mechanisms discussed by Taylor. For example, the case of using abdominal motion to shift the center of gravity in order to affect pitching moment was not directly discussed. Observations indicate that the predominate mechanisms may vary markedly from species to species and even between flight regimes for a given species [65]. The general conclusion of the analysis provided should extend to other means of generating torques. That is, the control can be implemented so that the net rotational response of the body is the same whether symmetrical torques are generated based on bilateral combination of the haltere feedback, or whether control response is based purely on ipsilateral feedback.

Observation that timing of the stroke reversal is a mechanism of control appears to be supported by comparison of results shown in (5–45)-(5–50) and (5–64)-(5–69). The result based on wing abduction to stabilize the body, (5–45)-(5–50), requires both the desired force in the z-direction and the pitch rate as inputs to influence the pitch control moment. If a stabilizing pitch moment can be generated through control of stroke reversal, while maintaining the lift force roughly through the center of gravity, then the six control parameters become purely decoupled as shown in (5–64)-(5–69). This coupling evident in (5–45)-(5–50) is a direct consequence of the use of abduction angle as a control parameter and is even evident in the case where contralateral influence is allowed to ensure control symmetry of control force magnitudes. On the other hand, the ipsilateral cases, where there is a lack of knowledge of control response on the other side, leads to errors in net lift force due to the independence of the control forces. Ideally, contralateral influence would be allowed to ensure control force symmetry and a moment would be generated during stroke reversal to control pitch motion. In this way, all control responses are purely decoupled and, due to the symmetry of the control forces, the desired vertical and horizontal forces on the body are maintained.

The above discussion assumes the ability to generated the required control forces when commanded, without error or coupling. This is generally unrealistic, especially in the

viscous, time varying flowfield associated with flapping wings. If the muscles of the wing impart a force to impart a net pronation, one would expect both a resulting force in the plane of the stroke and some resulting change in the out-of-plane thrust being generated by the wing. Direct quantification of these effects can be very difficult due to unsteady nature of the flowfield and the aero-elasticity of the wings. The implication to flight stability of unavoidable cross-coupling in torque generation mechanisms was addressed through a Lyapunov stability analysis [71]. The intent was to infer a "rule-of-thumb" for what level of cross-coupling can exist while still guaranteeing stability. A Lyapunov analysis does not in general tell where the system is unstable, but instead characterizes and bounds a region of stability. The case for control proportional to the measured rates, with cross coupling into the other axes, showed that, for an assumed rigid body, the system will be asymptotically stable as long as the ratio of the maximum cross coupling term to the minimum control gain is less than 0.5. The addition of viscous rotational drag was shown to enhance stability. The Reynold's number, which is the ratio of inertial to viscous forces, is relatively low for an insect due to small size scales and velocities, therefore viscous drag should play a prominent role, aiding flight stability.

The 6DOF simulation contained both behavioral features and basic feedback control logic. Behaviorally, the simulation used non-linear activation functions to make decisions with regard to whether or not to pursue a target, what mode to use in moving toward the target, and whether to react to obstructions. The obstruction avoidance reactions in particular allowed for investigation of saccadic behavior. One of the fundamental objectives of the simulation was to determine the ability of the halteres with the assumed encoding and decoding scheme to provide adequate control stability. The stability analysis previously discussed assumed perfect feedback signals. With noise and other disturbances, a stable but bounded performance would be expected.

The general case shown in Figure 5-3 provides numerous obstacles to traverse. The simulated insect successfully navigates through the obstacles whether with feedback of

perfect measurements or with feedback of haltere measurements encoded by the modeled sensilla. The stability is bounded with the haltere measurements, i.e. the body rates do not converge as desired to zero. This can readily be seen in Figure 5-7 where the solution is stable but it oscillates within a bounded region determined by the quantization associated with sensilla sampling. The errors from the halteres were seen to be less than 10% in general (Figure 5-6), however, during low level disturbances, as seen at the beginning of Figure 5-7, the errors were much larger and more erratic. This is expected due to the upstroke/downstroke summation and differencing going on as represented by (4–6 and 4–7). In addition, the reconstruction of the body rates combines the error from the two halteres. These errors may cancel or add, depending on the rate component being constructed and the signs of the errors. Hengstenburg observed that in *Calliphora* that the halteres have little influence below 50 deg/sec, and, therefore, large drifts would be expected if the halteres were used to maintain orientation [3]. Similarly, Hengstenburg observed that the vision system has limited capability at higher frequencies. Optic flow based feedback is likely to play an important role in the region where the haltere quantization errors are largest.

Behavioral responses are tightly tied to non-linear activation [72]. Saccades have been characterized as obstruction avoidance maneuvers in flies [66]. In Figure 5-13, experimental observations of saccades are described by an Euler angle transformation sequence. Defined in yaw-pitch-roll order, the saccade involves a yawing motion away from the obstruction, accompanied by a simultaneous slight pitch up and dorsal roll toward the center of the turn. Care must be taken in interpreting the data since the defined order of the Euler angle transformation strongly influences the description. After the maneuver settles out, the end result is a velocity vector along a new heading. A characteristic seen in the measured data is the asymmetry in the roll response. The roll response decays back to zero much more slowly than the initial response. This is particularly evident in Figure 5-13c for large saccade angles. The simulated avoidance

behavior did not demonstrate this asymmetry. Two possible explanations are provided for this difference. The first deals with the approximation of aerodynamic forces in the simulation. In a real bank-to-turn maneuver, aerodynamic forces would be maximum during the beginning of the roll maneuver when heading error is at a maximum. As the fly comes around, roll, which is assumed to be driven in proportion to heading error, will decrease and the fly will gradually assume a nominal orientation at the new heading. In the simulation, the yaw torque around the inertial z-axis is applied in proportion to the roll angle independent of any estimation of the actual aerodynamic forces. This is stated with one caveat, rotational drag is included in the simulation. These limitations in how aerodynamic forces are modeled are possibly a factor in the discrepancy. A second possible explanation would be that the roll response of the fly may be reflexive reaction to an activation response that rises much more rapidly than it decays. In the simulation, the roll response is driven uniformly by the error in heading once activated. Either of these explanations, or a combination, might explain the discrepancy between the measured and simulation data, and both can be explored in future studies.

5.5 Concluding Remarks

The 6DOF simulation demonstrated that the halteres, as modeled, provide sufficient accuracy to enhance stability above and beyond what aerodynamic damping alone might provide. There are many assumptions that went into the demonstration of this statement. The bandwidth of the attitude control system, the proportionality constants for the rate feedback (damping) used, the damping and stiffness characteristics of the haltere itself all influence the result and were chosen objectively prior to achieving the result. Real flies are catastrophically unstable without halteres, but not with the additional damping gained by gluing a string to their abdomen [5]. In the simulation, elimination of the halteres, as shown in Figure 5-10, was not catastrophic. This implies that the aerodynamic drag was perhaps overestimated in the simulation and the halteres may have an even more significant influence than the chosen control gains allowed. However, even as modeled, it

is clear that the halteres, with their limited dynamic response, coarse quantization, and encoding limitations provide a substantial improvement in flight performance.

The simulation as implemented had numerous limitations. One of the most glaring limitations was the lack of true aerodynamic models. Because of this, control schemes for flapping wings could not be directly investigated. Neither could the form of feedback, ipsilateral versus contralateral. The Lyapunov stability analysis, including derivations of control schemes with and without contralateral influence was meant to provide additional confidence in the simulation results. Fruitful areas for future investigation include the addition of aerodynamic models and the addition of higher fidelity optical sensing models. The use of cylindrical obstructions was a compromise dictated by the lack of a compound eye model. Performance demonstration in an environment with more general obstructions is desired and will be pursued in the future.

CHAPTER 6
CONCLUSION

The work embodied in this dissertation was intended to establish a working theory for haltere functionality. In line with this objective, three major tasks have been completed:

1. The mathematical basis for haltere dynamic response has been documented, a novel mechanism for rate decoupling has been proposed, and performance limitations have been analyzed.

2. A model for the haltere, compatible with the insect sensory physiology, has been demonstrated, providing for the first time a plausible theory for how angular rates are encoded by campaniform sensilla.

3. A behavioral flight simulation has been constructed that demonstrates the ability of halteres to stabilize flight in the presence of disturbances and non-linearly activated behavioral response.

At the beginning of this research, the literature consisted of only basic kinematic analysis of the haltere and observation of the haltere's influence. Understanding of the physical and mathematical basis behind the ability of the haltere to encode and decouple the angular rates it responds to was very limited in the literature. Prior kinematic analysis, performed primarily by Pringle and Nalbach, was sufficient to determine the basic inertial forces that act on the haltere as it oscillates back and forth [14], [23]. That level of analysis is limited in its ability to address the sensory mechanisms of the haltere which are related to haltere deflection and, therefore, directly tied to the influence of damping and stiffness in the haltere structure. Additional deficiencies in the literature were a lack of treatment of decoupling mechanisms for the forces proportional to the body rates and a lack of any substantial theory for how the rate components are encoded in the campaniform sensilla. The work described in this dissertation addresses these deficiencies. In addition, it provides analysis with regard to insect flight stability in general and the implications of ipsilateral versus bilateral feedback into the flight control system. Further, a proposed model for the haltere with dynamic cross coupling errors and sensilla quantization limitations has been shown to sufficiently capture the body rates to

stabilize flight under general dynamic conditions, including saccadic maneuvers activated by obstructions.

Chapter 3 performs a full dynamic assessment of the haltere with variations in stiffness and damping. The model of the haltere was general by design, representing the structure in non-dimensional terms to avoid any conclusions tied to a specific configuration or species. Higher level physical understanding was being sought to allow for a fundamental theory of the sensory mechanisms involved. The results of the dynamic simulations led to the theory that by measuring the averaged slope, and the averaged magnitude of the haltere trajectory, the two observable rate components in the plane of haltere oscillation could be decoupled. An alternative articulation of this assertion is that, relative to the stroke center, a symmetric response of the haltere is caused by the yaw rate and an anti-symmetric response is caused by the lateral rate component. For a proportional relationship between the rate components and the described features to hold over the range of haltere output, the governing equations must be approximately linear. This linearity was demonstrated mathematically and through parametric analysis over a broad range of body rates.

Chapter 4 took the models described in Chapter 3 and added to them a model of the bed of campaniform sensilla that experimental biologists have correlated with rate encoding and stimulation of wing control muscles. These sensilla respond in a binary, unidirectional manner and are distributed over the base of the haltere so as to fractionate the dynamic range of output using the 100 or so sensilla. A theory was proposed and successfully demonstrated using models and simulations to show that these very simple sensilla can in fact encode both the sign and magnitude of the two rate components. In an amazing twist, it is the very characteristic that we would try to avoid as a limitation, the unidirectional sensitivity of the sensilla, that makes them uniquely suited for capturing the symmetry and asymmetry, and associated signs of the rate components. Nature is, by this theory, recording the signs of the rate components using the phasing of the response

of these unidirectional sensors. There are several limitations of the work described in Chapter 4. First, the models used are open-loop and the test cases were general but limited in scope. Second, the theory provides no direct experimental substantiation. Data in the experimental community is very limited with regard to characterization of campaniform sensilla and a means by which the resulting afferents might be decoded according to the described theory cannot yet be identified due to limited understanding of the function of the complicated control structure of the wings. The proposed model is very specific, and experimental biologists should be able to directly examine the proposed theory in the future.

Chapter 5 addresses the open-loop limitation described for Chapter 4. The models proposed in Chapter 3 and 4 for haltere dynamics and rate encoding were incorporated in a 6 degree-of-freedom (6DOF) simulation of a Dipteran insect. This simulation was written specifically for this research and allows for competing behavioral objectives stimulated by non-linear activation functions. The goal was to demonstrate the ability of the proposed haltere model to stabilize flight in the presence of dynamic obstruction avoidance reactions. If the model was functionally adequate, the simulated insect would navigate through a complex environment with randomly distributed obstructions, using maneuvers representative of the highly dynamic saccades of flies, and then acquire and intercept the desired target. In order to facilitate saccade-like behavior, a bank-to-turn response was programmed for large heading errors. The simulation performed well, demonstrating that the halteres as modeled, with limited resolution and errors associated with cross-coupling and dynamic response, were sufficient to provide rate stabilizing feedback for the simulated insect.

The simulation described has a number of limitations associated with force generation. Stroke-averaged forces on the body are assumed to be generated by the wings without error. Aerodynamic simulation of the complex unsteady flow associated with the wings was outside the scope of this effort. Because of this assumption, a specific mechanism

for control implementation was not needed, and implications of feedback pathways were ignored, whether ipsilateral or bilateral. To address these modeling limitations, separate analysis was performed of both rate stabilization in the presence of cross-coupling and aerodynamic damping, and ipsilateral versus bilateral feedback. The conclusion of the stability analysis was that a fly or any other body approximately described by Euler's equations should be robust to cross-coupling disturbances up to fifty percent of the desired control torque. The second study concluded that ipsilateral haltere feedback to the wings, with appropriate constant control gains, is equivalent to control based on bilaterally calculated inertial rates, except for a residual error in the vertical force. This error is due to potential asymmetric correction of roll rate.

The significance of this work to engineering design is not clear. Building a haltere based inertial measurement unit is probably not advantageous given the current availability of two axis rate gyros on a chip for approximately thirty five US dollars. We may however learn more subtle lessons from the way nature has integrated together its solution. For example, 1) extremely simple strain sensors, highly integrated into the structure, can provide feedback over a wide dynamic range by distributing them appropriately, a process referred to in biology as range fractionation. 2) A structure originally designed for force generation may with adaptation be used for rate sensing. The two rear wings of flies have adapted for rate sensitivity. With a few strain sensors, a rotating motor on a micro-air vehicle may be able to provide beneficial rate feedback to create a stabilized sensing platform. 3) Rate sensors do not need to be situated on orthogonal axes. The planes of haltere oscillation are oriented approximately 120 degrees apart, not 90. Due to the symmetry of the geometry, the difference is simply a constant factor from the control system perspective. 4) The use and advantage of symmetry in designs is grossly underutilized. The symmetry we see everywhere in nature has been maintained for reasons associated with control design. The symmetry of the haltere dynamic response can be used so that a single oscillating non-linear device can measure

two independent rate components. The bilateral symmetry of the haltere/wing geometry allows for direct ipsilateral feedback, eliminating the need for precalculation of inertial rates prior to feedback. 5) Related to signal symmetry, unidirectional strain sensing may be advantageous in certain circumstances, allowing for an unconventional way of determining both magnitude and phasing of an oscillating signal.

The halteres appear to be only one means of measuring inertial motion in insects. Dipteran insects have halteres. Dragon flies appear to use their head as a sensitive proof mass to sense angular acceleration. Moths vibrate their antennae to provide rate feedback in a way that is not completely understood. As we continue to build smaller more tightly integrated flying vehicles, there are many lessons we can learn from the varied designs of nature. However, we must be careful to assess the natural solutions we choose. Both nature and man need robust solutions that can deal with the complexities and uncertainties of our respective missions, but our definitions of success are quite different. In nature it is survival of the population that is important and the success of the individual is of little consequence. In man's designs we strive for very high performance of the individual for reasons of cost and consequence. The difference that these requirements dictate in terms of repeatability and predictability is likely quite significant.

APPENDIX A
DERIVATION OF THE HALTERE DYNAMICS EQUATION

The expression in (3–12) can be determined by defining two reference frames in addition to the body fixed frame. These frames are related by the stroke angle γ and the out-of-plane displacement angle θ, as shown in Figure A-1. When these angles are zero, the three frames are co-aligned. The associated angular velocities are

$$
\begin{aligned}
{}^{e}\vec{\omega}^{b} &= \Omega_1\hat{b}_1 + \Omega_2\hat{b}_2 + \Omega_3\hat{b}_3 && \text{(A–1)}\\
{}^{b}\vec{\omega}^{h} &= \dot{\gamma}\hat{b}_2 && \text{(A–2)}\\
{}^{h}\vec{\omega}^{f} &= \dot{\theta}\hat{h}_1. && \text{(A–3)}
\end{aligned}
$$

The position and velocities, as observed in the various reference frames, of the mass at the end of the haltere (Point 2) are

$$
\begin{aligned}
\vec{P}_{12} &= r\hat{f}_3 && \text{(A–4)}\\
{}^{h}\vec{v}^{2} &= {}^{h}\vec{\omega}^{f} \times \vec{P}_{12} && \text{(A–5)}\\
{}^{b}\vec{v}^{2} &= {}^{h}\vec{v}^{2} + {}^{b}\vec{\omega}^{h} \times \vec{P}_{12} && \text{(A–6)}\\
{}^{e}\vec{v}^{2} &= {}^{b}\vec{v}^{2} + {}^{e}\vec{\omega}^{b} \times \vec{P}_{12}. && \text{(A–7)}
\end{aligned}
$$

The expressions leading to the acceleration of the haltere relative to the inertial frame are

$$
\begin{aligned}
{}^{h}\vec{a}^{2} &= {}^{h}\vec{\alpha}^{f} \times \vec{P}_{12} + {}^{h}\vec{\omega}^{f} \times {}^{h}\vec{\omega}^{f} \times \vec{P}_{12} && \text{(A–8)}\\
{}^{b}\vec{a}^{2} &= {}^{h}\vec{a}^{2} + 2({}^{b}\vec{\omega}^{h} \times {}^{h}\vec{v}^{2}) + {}^{b}\vec{\alpha}^{h} \times \vec{P}_{12} + {}^{b}\vec{\omega}^{h} \times {}^{b}\vec{\omega}^{h} \times \vec{P}_{12} && \text{(A–9)}\\
{}^{e}\vec{a}^{2} &= {}^{b}\vec{a}^{2} + 2({}^{e}\vec{\omega}^{b} \times {}^{b}\vec{v}^{2}) + {}^{e}\vec{\alpha}^{a} \times \vec{P}_{12} + {}^{e}\vec{\omega}^{b} \times {}^{e}\vec{\omega}^{b} \times \vec{P}_{12}. && \text{(A–10)}
\end{aligned}
$$

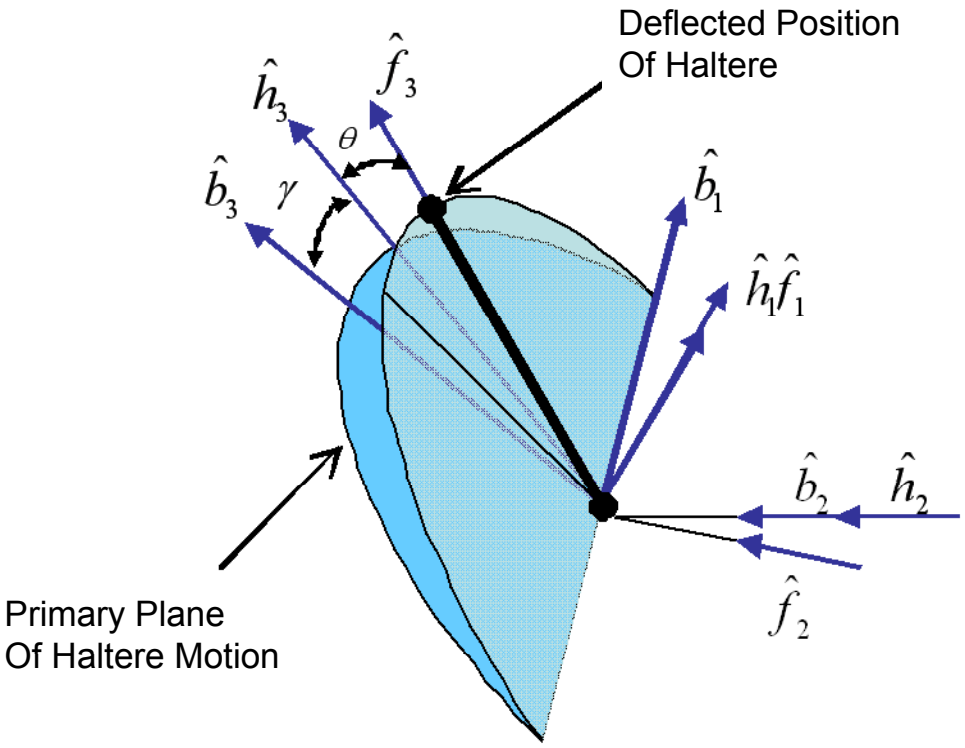

Figure A-1. The relative orientation of the reference frames associated with the equation of motion derivation are shown above. The "h" frame is rotated by angle γ with respect the "b" frame. The "f" frame is rotated by angle θ with respect to the "h" frame.

The expression in (A–10) assumes that the acceleration of the body (Point 1) is small relative to the relevant haltere acceleration terms. This results in the acceleration of point 2 with respect to the earth (inertial) frame in the direction as

$$\begin{aligned}
\hat{f}_2 \cdot^e \vec{a}^2 &= r[\dot{\Omega}_3 \sin(\gamma) - \dot{\Omega}_1 \cos(\gamma) - \dot{\gamma}^2 \cos(\theta)\sin(\theta) \\
&\quad +2\dot{\gamma}[(\Omega_3 \cos(\gamma) + \Omega_1 \sin(\gamma))\cos^2(\theta) - \Omega_2 \cos(\theta)\sin(\theta)] \\
&\quad +(\Omega_3^2 \cos^2(\gamma) + \Omega_1^2 \sin^2(\gamma) - \Omega_2^2)\cos(\theta)\sin(\theta) \\
&\quad +(\Omega_2\Omega_3 \cos(\gamma) + \Omega_1\Omega_2 \sin(\gamma))\cos(2\theta) \\
&\quad +2\Omega_1\Omega_3 \cos(\theta)\sin(\theta)\cos(\gamma)\sin(\gamma) - \ddot{\theta}].
\end{aligned} \tag{A–11}$$

The final expression in (3–12) is obtained by taking the dot product of the inertial force, $(-m^e\vec{a}^2)$, in the direction of the out-of-plane deflection $(\hat{f}_2)$ and then adding the forces associated with stiffness and damping to create a zero sum as

$$\hat{f}_2 \cdot (\vec{F}_{inertial} + \vec{F}_{damping} + \vec{F}_{stiffness}) = 0. \tag{A–12}$$

Since $r\theta$ increases in the negative $\hat{f}_2$ direction, the stiffness and damping forces were defined as

$$\hat{f}_2 \cdot \vec{F}_{damping} = rm2\zeta\omega_n\dot{\theta} \tag{A–13}$$

$$\hat{f}_2 \cdot \vec{F}_{damping} = rm\omega_n^2\theta. \tag{A–14}$$

The resulting expression was divided by the product of the radius of gyration and mass to put it in the final non-dimensional form as

$$\frac{-\hat{f}_2 \cdot^e \vec{a}^2}{r} + 2\zeta\omega_n\dot{\theta} + \omega_n^2\theta = 0. \tag{A–15}$$

APPENDIX B
DERIVATION OF 6DOF EQUATIONS OF MOTION

The following derivation provides the equations of motion used for the simulation results provided in Chapter 5. The derivation of the quaternion dynamics in terms of the current quaternion state and the body rates is provided by reference [69]. Definitions of the symbols used in the derivation are shown in Table B-1.

Table B-1. Definitions of variables and symbols associated with 6DOF equations of motion.

Symbol	Definition
W	: body weight
$\xi = [e_0, e_x, e_y, e_z]^T$	: quaternion defining body to inertial transformation
$\vec{g} = \ g\hat{k}$	: gravity vector
$\vec{F} = F_{bx}\hat{b}_1 + F_{by}\hat{b}_1 + F_{bz}\hat{b}_3$	: external forces expressed in body frame
$\vec{T} = T_{bx}\hat{b}_1 + T_{by}\hat{b}_1 + T_{bz}\hat{b}_3$	: external torques expressed in body frame
${}^i\vec{V} = u\hat{b}_1 + v\hat{b}_1 + w\hat{b}_3$	: inertial velocity expressed in the body frame
${}^i\vec{\omega}^b = p\hat{b}_1 + q\hat{b}_1 + r\hat{b}_3$	: inertial rotation rate expressed in the body frame
I_b	: inertia matrix relative to the mass center in the body frame
$\frac{{}^i d}{dt}$	: derivative with respect to the inertial frame
$[\ \ ]_b$	: vector expressed in the body frame
$\otimes$	: quaternion multiplication
$\times$	: cross product

The translational dynamics of the body in terms of body relative measurements are found by equating the inertial response to the applied forces. The inertial acceleration can be represented in terms of body referenced angular rates and velocities as

$$\begin{aligned} \frac{{}^i d^i\vec{V}}{dt} &= \frac{{}^b d^i\vec{V}}{dt} + {}^i\vec{\omega}^b x^i\vec{V} = \frac{{}^b d}{dt}\begin{bmatrix} u \\ v \\ w \end{bmatrix}_b + \begin{bmatrix} p \\ q \\ r \end{bmatrix}_b \times \begin{bmatrix} u \\ v \\ w \end{bmatrix}_b, \\ \frac{{}^i d^i\vec{V}}{dt} &= \begin{bmatrix} \dot{u} \\ \dot{v} \\ \dot{w} \end{bmatrix}_b + \begin{bmatrix} qw - rv \\ ru - pw \\ pv - qu \end{bmatrix}_b . \end{aligned} \tag{B–1}$$

To put the forces in the body frame, assume the self generated forces are given in the body frame and use the quaternion to transform the gravitational force into the body frame. The sum of forces is

$$\begin{aligned}
\frac{{}^i d^i \vec{V}}{dt} &= \frac{g}{W}\vec{F} + g\hat{k} = \frac{g}{W}\begin{bmatrix} F_{bx} \\ F_{by} \\ F_{bz} \end{bmatrix}_b + g\xi^{-1}\otimes\hat{\mathbf{k}}\otimes\xi \\
&= \frac{g}{W}\begin{bmatrix} F_{bx} \\ F_{by} \\ F_{bz} \end{bmatrix}_b + g\begin{bmatrix} e_0 \\ -e_x \\ -e_y \\ -e_z \end{bmatrix} \otimes \begin{bmatrix} 0 \\ 0 \\ 0 \\ 1 \end{bmatrix} \otimes \begin{bmatrix} e_0 \\ e_x \\ e_y \\ e_z \end{bmatrix} \\
\frac{{}^i d^i \vec{V}}{dt} &= \frac{g}{W}\begin{bmatrix} F_{bx} \\ F_{by} \\ F_{bz} \end{bmatrix}_b + g\begin{bmatrix} 2(e_z e_x - e_y e_0) \\ 2(e_0 e_x + e_y e_z) \\ e_0^2 + e_z^2 - e_x^2 - e_y^2 \end{bmatrix}_b
\end{aligned} \tag{B–2}$$

Equating these results gives

$$\begin{bmatrix} \dot{u} \\ \dot{v} \\ \dot{w} \end{bmatrix} = \frac{g}{W}\begin{bmatrix} F_{bx} \\ F_{by} \\ F_{bz} \end{bmatrix} + g\begin{bmatrix} 2(e_z e_x - e_y e_0) \\ 2(e_0 e_x + e_y e_z) \\ e_0^2 + e_z^2 - e_x^2 - e_y^2 \end{bmatrix} + \begin{bmatrix} rv - qw \\ pw - ru \\ qu - pv \end{bmatrix}. \tag{B–3}$$

The position in the inertial frame is found through integration of the velocity after transformation into the inertial frame,

$$\begin{bmatrix} \dot{x} \\ \dot{y} \\ \dot{z} \end{bmatrix} = \begin{bmatrix} e_0 \\ e_x \\ e_y \\ e_z \end{bmatrix} \otimes \begin{bmatrix} 0 \\ u \\ v \\ w \end{bmatrix} \otimes \begin{bmatrix} e_0 \\ -e_x \\ -e_y \\ -e_z \end{bmatrix}. \tag{B–4}$$

Expanding the quaternion multiplications gives

$$\begin{aligned}
\begin{bmatrix} \dot{x} \\ \dot{y} \\ \dot{z} \end{bmatrix} &= \begin{bmatrix} e_0 * S_x + e_x * S_0 + e_y * S_z - e_z * S_y \\ e_0 * S_y - e_x * S_z + e_y * S_0 + e_z * S_x \\ e_0 * S_z + e_x * S_y - e_y * S_x + e_z * S_0 \end{bmatrix}, \text{ where} \qquad \text{(B–5)} \\
S_0 &= u * e_x + v * e_y + w * e_z \\
S_x &= u * e_0 - v * e_z + w * e_y \\
S_y &= u * e_z + v * e_0 - w * e_x \\
S_z &= -u * e_y + v * e_x + w * e_0.
\end{aligned}$$

Similarly, the rotational dynamics are found by equating the inertial response to the applied torques around the center of gravity,

$$\frac{^i d}{dt}([I_b]^i \vec{\omega}^b) = [I_b]\frac{^b d^i \vec{\omega}^b}{dt} +^i \vec{\omega}^b x [I_b]^i \vec{\omega}^b. \qquad \text{(B–6)}$$

Where

$$I_b = \begin{bmatrix} I_{xx} & -I_{xy} & -I_{xz} \\ -I_{xy} & I_{yy} & -I_{yz} \\ -I_{xz} & -I_{yz} & I_{zz} \end{bmatrix}_b.$$

This expression becomes

$$\begin{aligned}
[I_b]\frac{^b d^i \vec{\omega}^b}{dt} +^i \vec{\omega}^b x [I_b]^i \vec{\omega}^b &= [I_b] \begin{bmatrix} \dot{p} \\ \dot{q} \\ \dot{r} \end{bmatrix}_b + \begin{bmatrix} p \\ q \\ r \end{bmatrix}_b \times \begin{bmatrix} pI_{xx} - qI_{xy} - rI_{xz} \\ -pI_{xy} + qI_{yy} - rI_{yz} \\ -I_{xz}p - qI_{yz} + rI_{zz} \end{bmatrix}_b \\
&= [I_b] \begin{bmatrix} \dot{p} \\ \dot{q} \\ \dot{r} \end{bmatrix}_b - \qquad \text{(B–7)}
\end{aligned}$$

$$\begin{bmatrix} rq(I_{yy}-I_{zz})+I_{yz}(q^2-r^2)-rpI_{xy}+pqI_{xz} \\ pr(I_{zz}-I_{xx})+I_{xz}(r^2-p^2)-pqI_{yz}+qrI_{xy} \\ pq(I_{xx}-I_{yy})+I_{xy}(p^2-q^2)-qrI_{xz}+prI_{yz} \end{bmatrix}_b .$$

Equating this to the applied torques in the body frame and solving for the required derivatives gives

$$\begin{bmatrix} \dot{p} \\ \dot{q} \\ \dot{r} \end{bmatrix}_b = \begin{bmatrix} I_{xx} & -I_{xy} & -I_{xz} \\ -I_{xy} & I_{yy} & -I_{yz} \\ -I_{xz} & -I_{yz} & I_{zz} \end{bmatrix}_b^{-1} \cdot \left(\begin{bmatrix} rq(I_{yy}-I_{zz})+I_{yz}(q^2-r^2)-rpI_{xy}+pqI_{xz} \\ pr(I_{zz}-I_{xx})+I_{xz}(r^2-p^2)-pqI_{yz}+qrI_{xy} \\ pq(I_{xx}-I_{yy})+I_{xy}(p^2-q^2)-qrI_{xz}+prI_{yz} \end{bmatrix}_b + \begin{bmatrix} T_{bx} \\ T_{by} \\ T_{bz} \end{bmatrix}_b \right) . \tag{B–8}$$

The quaternion derivatives, which are a function of the body rate vector, are provided without proof as

$$\begin{bmatrix} \dot{e}_0 \\ \dot{e}_x \\ \dot{e}_y \\ \dot{e}_z \end{bmatrix} = \frac{1}{2} \begin{bmatrix} -e_x & -e_y & -e_z \\ e_0 & -e_z & e_y \\ e_z & e_0 & -e_x \\ -e_y & e_x & e_0 \end{bmatrix} \begin{bmatrix} p \\ q \\ r \end{bmatrix}_b . \tag{B–9}$$

See [69] for a derivation of (B–9). Equations (B–3),(B–4),(B–8), and(B–9) make up thirteen equations that when integrated define linear and angular position and velocity states of the body in terms of a quaternion transformation.

APPENDIX C
DERIVATION OF CONTROL USING HALTERE FEEDBACK

C.1 Contralateral Haltere Influence with Abduction as a Control Parameter

See Table 5-3 and Figure 5-4 for a definition of terms used in the following derivations. The torques from the wings are the cross product of the position of the center of pressure, relative to the center of gravity, and the wing force. Therefore,

$$\begin{aligned}\vec{T}_R &= \vec{R}_R \times \vec{F}_R \\ \vec{T}_L &= \vec{R}_L \times \vec{F}_L\end{aligned}$$

where

$$\begin{aligned}\vec{R}_R &= (d - L\sin(\alpha_0 + \delta_{\alpha R}))\hat{\imath}_x + (w + L\cos(\alpha_0 + \delta_{\alpha R}))\hat{\imath}_y \\ \vec{R}_L &= (d - L\sin(\alpha_0 + \delta_{\alpha R}))\hat{\imath}_x - (w + L\cos(\alpha_0 + \delta_{\alpha R}))\hat{\imath}_y\end{aligned}$$

and

$$\begin{aligned}\vec{F}_R &= F_{Rx}\hat{\imath}_x + F_{Ry}\hat{\imath}_y + F_{Rz}\hat{\imath}_z \\ \vec{F}_L &= F_{Lx}\hat{\imath}_x + F_{Ly}\hat{\imath}_y + F_{Lz}\hat{\imath}_z.\end{aligned}$$

Taking the cross products gives

$$\vec{T}_R = \det\begin{bmatrix}\hat{\imath}_x & \hat{\imath}_y & \hat{\imath}_z \\ R_{Rx} & R_{Ry} & 0 \\ F_{Rx} & F_{Ry} & F_{Rz}\end{bmatrix}, \quad \vec{T}_L = \det\begin{bmatrix}\hat{\imath}_x & \hat{\imath}_y & \hat{\imath}_z \\ R_{Lx} & R_{Ly} & 0 \\ F_{Lx} & F_{Ly} & F_{Lz}\end{bmatrix}$$

$$\begin{aligned}\vec{T}_R &= R_{Ry}F_{Rz}\hat{\imath}_x - R_{Rx}F_{Rz}\hat{\imath}_y + (R_{Rx}F_{Ry} - R_{Ry}F_{Rx})\hat{\imath}_z \\ \vec{T}_L &= R_{Ly}F_{Lz}\hat{\imath}_x - R_{Lx}F_{Lz}\hat{\imath}_y + (R_{Lx}F_{Ly} - R_{Ly}F_{Lx})\hat{\imath}_z \\ \vec{T}_R &= F_{Rz}(w + L\cos(\alpha_0 + \delta_{\alpha R}))\hat{\imath}_x - F_{Rz}(d - L\sin(\alpha_0 + \delta_{\alpha R}))\hat{\imath}_y + \qquad \text{(C–1)} \\ &\quad (F_{Ry}(d - L\sin(\alpha_0 + \delta_{\alpha R})) - F_{Rx}(w + L\cos(\alpha_0 + \delta_{\alpha R})))\hat{\imath}_z \\ \vec{T}_L &= -F_{Lz}(w + L\cos(\alpha_0 + \delta_{\alpha L}))\hat{\imath}_x - F_{Lz}(d - L\sin(\alpha_0 + \delta_{\alpha L}))\hat{\imath}_y + \qquad \text{(C–2)}\end{aligned}$$

$$(F_{Ly}(d - L\sin(\alpha_0 + \delta_{\alpha L})) + F_{Lx}(w + L\cos(\alpha_0 + \delta_{\alpha L})))\hat{\imath}_z.$$

To generate a stabilizing control response, torques have to be generated in the opposite direction of the measured angular rates. Neither haltere measures rates in the roll, pitch, yaw frame of the insect. The combination of the responses from the two halteres produces rates proportional to the rates in the body frames. For example, the body rates in terms of the haltere measurements are

$$\begin{aligned} p &= -\frac{\Omega_{b3} + \Omega_{c3}}{2\sin(\eta)} \\ q &= \frac{\Omega_{b3} - \Omega_{c3}}{2\cos(\eta)} \\ r &= -\Omega_{b1} = -\Omega_{c1} = -\Omega_1. \end{aligned}$$

Therefore, the control torques must be

$$\begin{aligned} T_x &= -K_x p = K_x \cdot \frac{\Omega_{b3} + \Omega_{c3}}{2\sin(\eta)} \\ T_y &= -K_y q = -K_y \cdot \frac{\Omega_{b3} - \Omega_{c3}}{2\cos(\eta)} \\ T_z &= -K_z r = K_z \cdot \Omega_1. \end{aligned}$$

The combined torques can be found by combining (C–1) and (C–2), expressed in terms of the abduction deviation $\delta_{\alpha R}$ and the two stroke averaged forces F_{Rx} and F_{Ry} as

$$\begin{aligned} T_x &= F_{Rz}(w + L\cos(\alpha_0 + \delta_{\alpha R})) - F_{Lz}(w + L\cos(\alpha_0 + \delta_{\alpha L})) \\ T_y &= -F_{Rz}(d - L\sin(\alpha_0 + \delta_{\alpha R})) - F_{Lz}(d - L\sin(\alpha_0 + \delta_{\alpha L})) \\ T_z &= (F_{Ry}(d - L\sin(\alpha_0 + \delta_{\alpha R})) + F_{Ly}(d - L\sin(\alpha_0 + \delta_{\alpha L}))) \\ &\quad +(F_{Lx}(w + L\cos(\alpha_0 + \delta_{\alpha L})) - F_{Rx}(w + L\cos(\alpha_0 + \delta_{\alpha R}))) \\ F_x &= F_{Lx} + F_{Rx} \\ F_y &= F_{Ry} + F_{Ly} = 0 \\ F_z &= F_{Rz} + F_{Lz}. \end{aligned} \tag{C–3}$$

If the control deviation in abduction angle, $\delta_{\alpha R}$, is assumed to be small, then

$$\begin{aligned}
\sin(\alpha_0 + \delta_\alpha) &\approx \sin(\alpha_0) + \cos(\alpha_0)\delta_\alpha \\
\cos(\alpha_0 + \delta_\alpha) &\approx \cos(\alpha_0) - \sin(\alpha_0)\delta_\alpha \\
d - L\sin(\alpha_0) &= 0.
\end{aligned}$$

Applying these approximations to (C–3) gives

$$\begin{aligned}
T_x &\approx (F_{Rz} - F_{Lz})(w + L\cos(\alpha_0)) + L\sin(\alpha_0)(F_{Lz}\delta_{\alpha L} - F_{Rz}\delta_{\alpha R}) \\
T_y &\approx F_{Rz}(\cos(\alpha_0)\delta_{\alpha R}) + F_{Lz}(\cos(\alpha_0)\delta_{\alpha L}) \\
T_z &\approx -(F_{Ry}(\cos(\alpha_0)\delta_{\alpha R}) + F_{Ly}(\cos(\alpha_0)\delta_{\alpha L})) \\
&\quad +(F_{Lx} - F_{Rx})(w + L\cos(\alpha_0)) + L\sin(\alpha_0)(F_{Rx}\delta_{\alpha R} - F_{Lx}\delta_{\alpha L}) \\
F_x &= F_{Lx} + F_{Rx} \\
F_y &= F_{Ry} + F_{Ly} = 0 \\
F_z &= F_{Rz} + F_{Lz}.
\end{aligned} \tag{C–4}$$

Defining the right and left wing forces as half of the desired body force plus a differential force gives

$$\begin{aligned}
F_{Rx} &= \frac{F_{xd}}{2} + \Delta F_{Rx} \\
F_{Lx} &= \frac{F_{xd}}{2} + \Delta F_{Lx} \\
F_{Ry} &= \Delta F_{Ry} \\
F_{Ly} &= \Delta F_{Ly} \\
F_{Rz} &= \frac{F_{zd}}{2} + \Delta F_{Rz} \\
F_{Lz} &= \frac{F_{zd}}{2} + \Delta F_{Lz}.
\end{aligned}$$

Applying these to the torques represented by (C–4) gives

$$T_x \approx (\Delta F_{Rz} - \Delta F_{Lz})(w + L\cos(\alpha_0))$$

$$
\begin{aligned}
& + L\sin(\alpha_0)(\frac{F_{zd}}{2}(\delta_{\alpha L} - \delta_{\alpha R}) + \Delta F_{Lz}\delta_{\alpha L} - \Delta F_{Rz}\delta_{\alpha R}) \\
T_y &\approx (\frac{F_{zd}}{2} + \Delta F_{Rz})(\cos(\alpha_0)\delta_{\alpha R}) + (\frac{F_{zd}}{2} + \Delta F_{Lz})(\cos(\alpha_0)\delta_{\alpha L}) \\
T_z &\approx -(\Delta F_{Ry}(\cos(\alpha_0)\delta_{\alpha R}) + \Delta F_{Ly}(\cos(\alpha_0)\delta_{\alpha L})) \\
& + (\Delta F_{Lx} - \Delta F_{Rx})(w + L\cos(\alpha_0)) \\
& + L\sin(\alpha_0)(\frac{F_{xd}}{2}(\delta_{\alpha R} - \delta_{\alpha L}) + \Delta F_{Rx}\delta_{\alpha R} - \Delta F_{Lx}\delta_{\alpha L}) \\
F_x &= F_{Lx} + F_{Rx} \\
F_y &= F_{Ry} + F_{Ly} = 0 \\
F_z &= F_{Rz} + F_{Lz}.
\end{aligned}
\tag{C–5}
$$

If precalculation of the body rates, (p, q, r), from the measurements is allowed, then it can be required that

$$
\begin{aligned}
\Delta F_{Rx} &= -\Delta F_{Lx} \\
\Delta F_{Ry} &= -\Delta F_{Ly} \\
\Delta F_{Rz} &= -\Delta F_{Lz} \\
\delta_{\alpha L} &= \delta_{\alpha R}.
\end{aligned}
$$

The resulting expressions for the control torques become

$$
\begin{aligned}
-K_x p &\approx 2\Delta F_{Rz}(w + L(\cos(\alpha_0) - \sin(\alpha_0)\delta_\alpha) \\
-K_y q &\approx F_{zd}\cos(\alpha_0)\delta_\alpha \\
-K_z r &\approx -2\Delta F_{Rx}(w + L\cos(\alpha_0) - \sin(\alpha_0)\delta_\alpha).
\end{aligned}
\tag{C–6}
$$

The control parameter, $\delta_{\alpha R}$, can be approximated from the second of the expressions in (C–6) and the wing control forces can be found from the remaining two expressions in (C–6) as

$$
\delta_\alpha \approx \frac{-K_y q}{F_{zd} L\cos(\alpha_0)}
$$

$$
\begin{aligned}
\Delta F_{Rz} &= \frac{-K_x p}{2(w + L\cos(\alpha_0 + \delta_\alpha))} \\
\Delta F_{Rx} &= \frac{K_z r}{2(w + L\cos(\alpha_0 + \delta_\alpha))} \\
\Delta F_{Lx} &= -\Delta F_{Rx} \\
\Delta F_{Lz} &= -\Delta F_{Rz}.
\end{aligned}
$$

Summing torques and forces confirms the desired result, i.e.,

$$
\begin{aligned}
T_x &= -K_x p \\
T_y &= -K_y q \\
T_z &= -K_z r \\
F_x &= F_{xd} \\
F_y &= 0 \\
F_z &= F_{zd}.
\end{aligned}
$$

C.2 Ipsilateral Haltere Influence with Abduction as a Control Parameter

In the case of ipsilateral feedback, there is no pre-knowledge of the measurements on the other side and the control force is assumed to be a function of only measurements on that side. The desired average force in the sagittal plane is assumed to be pre-known based on higher level navigation functions. Beginning with (C–3) from the previous derivation,

$$
\begin{aligned}
T_x &= F_{Rz}(w + L\cos(\alpha_0 + \delta_{\alpha R})) - F_{Lz}(w + L\cos(\alpha_0 + \delta_{\alpha L})) \\
T_y &= -(F_{Rz}(d - L\sin(\alpha_0 + \delta_{\alpha R})) + F_{Lz}(d - L\sin(\alpha_0 + \delta_{\alpha L}))) \\
T_z &= (F_{Ry}(d - L\sin(\alpha_0 + \delta_{\alpha R})) + F_{Ly}(d - L\sin(\alpha_0 + \delta_{\alpha L}))) \\
&\quad +(F_{Lx}(w + L\cos(\alpha_0 + \delta_{\alpha L})) - F_{Rx}(w + L\cos(\alpha_0 + \delta_{\alpha R}))) \\
F_x &= F_{Lx} + F_{Rx} \\
F_y &= F_{Ry} + F_{Ly} = 0
\end{aligned}
$$

$$F_z = F_{Rz} + F_{Lz}.$$

The forces are again defined in terms of equal distribution of desired net force and commanded control deviations as

$$\begin{aligned} F_{Rx} &= \frac{F_{xd}}{2} + \Delta F_{Rx} \\ F_{Lx} &= \frac{F_{xd}}{2} + \Delta F_{Lx} \\ F_{Ry} &= \Delta F_{Ry} \\ F_{Ly} &= \Delta F_{Ly} \\ F_{Rz} &= \frac{F_{zd}}{2} + \Delta F_{Rz} \\ F_{Lz} &= \frac{F_{zd}}{2} + \Delta F_{Lz}. \end{aligned}$$

Therefore,

$$\begin{aligned} F_x &= F_{xd} + \Delta F_{Rx} + \Delta F_{Lx} \\ F_y &= \Delta F_{Ry} + \Delta F_{Ly} \approx 0 \\ F_z &= F_{zd} + \Delta F_{Rz} + \Delta F_{Lz}. \end{aligned}$$

The control torques are defined in terms of haltere measurements as

$$\begin{aligned} T_x &= -K_x p = K_x \frac{\Omega_{b3} + \Omega_{c3}}{2\sin(\eta)} \\ T_y &= -K_y q = -K_y \frac{\Omega_{b3} - \Omega_{c3}}{2\cos(\eta)} \\ T_z &= -K_z r = K_z \Omega_1, \end{aligned}$$

which leads to the following relationships between control parameters and haltere measurements,

$$\begin{aligned} K_x \frac{\Omega_{b3} + \Omega_{c3}}{2\sin(\eta)} &= (\frac{F_{zd}}{2} + \Delta F_{Rz})(w + L\cos(\alpha_0 + \delta_{\alpha R})) \\ &\quad -(\frac{F_{zd}}{2} + \Delta F_{Lz})(w + L\cos(\alpha_0 + \delta_{\alpha L})) \end{aligned}$$

$$
\begin{aligned}
&\approx (\Delta F_{Rz}(w + L\cos(\alpha_0 + \delta_{\alpha R})) - \Delta F_{Lz}(w + L\cos(\alpha_0 + \delta_{\alpha L})))\\
-K_y\frac{\Omega_{b3} - \Omega_{c3}}{2\cos(\eta)} &= -((\frac{F_{zd}}{2} + \Delta F_{Rz})(d - L\sin(\alpha_0 + \delta_{\alpha R}))\\
&\quad +(\frac{F_{zd}}{2} + \Delta F_{Lz})(d - L\sin(\alpha_0 + \delta_{\alpha L})))\\
K_z\Omega_1 &= (\Delta F_{Ry} + \Delta F_{Ly})(d - L\sin(\alpha_0 + \delta_{\alpha R}))\\
&\quad +(\Delta F_{Lx} - \Delta F_{Rx})(w + L\cos(\alpha_0 + \delta_{\alpha R})).
\end{aligned}
$$

In the simplification of the first term, $\cos(\alpha_0 + \delta_{\alpha R}) \approx \cos(\alpha_0 + \delta_{\alpha L})$ has been assumed. In addition, the net lateral force is assumed to be small in breaking up the torques into left and right components, giving

$$
\begin{aligned}
K_x\frac{\Omega_{b3}}{2\sin(\eta)} &= \Delta F_{Rz}(w + L\cos(\alpha_0 + \delta_{\alpha R}))\\
K_x\frac{\Omega_{c3}}{2\sin(\eta)} &= -\Delta F_{Lz}(w + L\cos(\alpha_0 + \delta_{\alpha L}))\\
-K_y\frac{\Omega_{b3}}{2\cos(\eta)} &= -(\frac{F_{zd}}{2} + \Delta F_{Rz})(d - L\sin(\alpha_0 + \delta_{\alpha R}))\\
K_y\frac{\Omega_{c3}}{2\cos(\eta)} &= -(\frac{F_{zd}}{2} + \Delta F_{Lz})(d - L\sin(\alpha_0 + \delta_{\alpha L}))\\
K_z \cdot \frac{\Omega_1}{2} &= \Delta F_{Lx}(w + L\cos(\alpha_0 + \delta_{\alpha R}))\\
K_z \cdot \frac{\Omega_1}{2} &= -\Delta F_{Rx}(w + L\cos(\alpha_0 + \delta_{\alpha R})).
\end{aligned}
\tag{C–7}
$$

Solving these expressions for the control forces results in

$$
\begin{aligned}
\Delta F_{Rx} &= -\frac{K_z\Omega_1}{2(w + L\cos(\alpha_0 + \delta_{\alpha R}))}\\
\Delta F_{Lx} &= \frac{K_z\Omega_1}{2(w + L\cos(\alpha_0 + \delta_{\alpha L}))}\\
\Delta F_{Rz} &= K_x\frac{\Omega_{b3}}{2\sin(\eta)(w + L\cos(\alpha_0 + \delta_{\alpha R}))}\\
\Delta F_{Lz} &= -K_x\frac{\Omega_{c3}}{2\sin(\eta)(w + L\cos(\alpha_0 + \delta_{\alpha L}))}.
\end{aligned}
\tag{C–8}
$$

Using this result in the third and fourth expression of (C–7) allows for the solution of the desired abduction angles. Small angles are assumed for the abduction angles, allowing the

following identities:

$$\begin{aligned}
\sin(\alpha_0 + \delta_\alpha) &\approx \sin(\alpha_0) + \cos(\alpha_0)\delta_\alpha \\
\cos(\alpha_0 + \delta_\alpha) &\approx \cos(\alpha_0) - \sin(\alpha_0)\delta_\alpha \\
d - L\sin(\alpha_0) &= 0
\end{aligned}$$

$$\begin{aligned}
0 &\approx K_x \frac{\Omega_{b3}}{2\sin(\eta)(w + L\cos(\alpha_0) - L\sin(\alpha_0)\delta_{\alpha R})} \\
&\quad + K_y \frac{\Omega_{b3}}{2\cos(\eta)L\cos(\alpha_0)\delta_{\alpha R}} + \frac{F_{zd}}{2} \\
0 &\approx K_x \frac{\Omega_{c3}}{2\sin(\eta)(w + L\cos(\alpha_0) - L\sin(\alpha_0)\delta_{\alpha L})} \\
&\quad + K_y \frac{\Omega_{c3}}{2\cos(\eta)L\cos(\alpha_0)\delta_{\alpha L}} - \frac{F_{zd}}{2}.
\end{aligned}$$

Solving these expressions for the abduction control parameters gives

$$\begin{aligned}
\delta_{\alpha R} &\approx \frac{C_1\Omega_{b3}}{C_2\Omega_{b3} - C_3 F_{zd}} \\
\delta_{\alpha L} &\approx \frac{C_1\Omega_{c3}}{C_2\Omega_{c3} + C_3 F_{zd}}, \text{ where} \\
C_1 &= K_y \sin(\eta)(w + L\cos(\alpha_0)) \\
C_2 &= (K_y \sin(\eta)\sin(\alpha_0) - K_x \cos(\eta)\cos(\alpha_0))L \\
C_3 &= \sin(\eta)(w + L\cos(\alpha_0))\cos(\eta)\cos(\alpha_0)L.
\end{aligned}$$

Therefore, the resulting expressions for the control parameters are

$$\begin{aligned}
\Delta F_{Rx} &= -\frac{K_z\Omega_1}{2(w + L\cos(\alpha_0 + \delta_{\alpha R}))} \\
\Delta F_{Lx} &= \frac{K_z\Omega_1}{2(w + L\cos(\alpha_0 + \delta_{\alpha L}))} \\
\Delta F_{Rz} &= K_x \frac{\Omega_{b3}}{2\sin(\eta)(w + L\cos(\alpha_0 + \delta_{\alpha R}))} \\
\Delta F_{Lz} &= -K_x \frac{\Omega_{c3}}{2\sin(\eta)(w + L\cos(\alpha_0 + \delta_{\alpha L}))} \\
\delta_{\alpha R} &\approx \frac{C_1\Omega_{b3}}{C_2\Omega_{b3} - C_3 F_{zd}}
\end{aligned}$$

$$
\begin{aligned}
\delta_{\alpha L} &\approx \frac{C_1\Omega_{c3}}{C_2\Omega_{c3} + C_3F_{zd}}, \text{ where} \\
C_1 &= K_y \sin(\eta)(w + L\cos(\alpha_0)) \\
C_2 &= (K_y \sin(\eta)\sin(\alpha_0) - K_x\cos(\eta)\cos(\alpha_0))L \\
C_3 &= \sin(\eta)(w + L\cos(\alpha_0))\cos(\eta)\cos(\alpha_0)L.
\end{aligned}
$$

Summing the forces and torques gives

$$
\begin{aligned}
F_x &\approx F_{xd} \\
F_y &\approx 0 \\
F_z &= F_{zd} + \Delta F_{Rz} + \Delta F_{Lz} \\
T_x &= -K_x p \\
T_y &= -K_y q \\
T_z &= -K_z r.
\end{aligned}
$$

C.3 Ipsilateral Haltere Influence with Aerodynamic Wing Moment as a Control Parameter

Beginning with (C–3) from Section C.1, the sum of the forces and torques are represented as

$$
\begin{aligned}
T_x &= F_{Rz}(w + L\cos(\alpha_0 + \delta_{\alpha R})) - F_{Lz}(w + L\cos(\alpha_0 + \delta_{\alpha L})) \\
T_y &= -(F_{Rz}(d - L\sin(\alpha_0 + \delta_{\alpha R})) + F_{Lz}(d - L\sin(\alpha_0 + \delta_{\alpha L}))) \\
T_z &= (F_{Ry}(d - L\sin(\alpha_0 + \delta_{\alpha R})) + F_{Ly}(d - L\sin(\alpha_0 + \delta_{\alpha L}))) \\
&\quad +(F_{Lx}(w + L\cos(\alpha_0 + \delta_{\alpha L})) - F_{Rx}(w + L\cos(\alpha_0 + \delta_{\alpha R}))) \\
F_x &= F_{Lx} + F_{Rx} \\
F_y &= F_{Ry} + F_{Ly} = 0 \\
F_z &= F_{Rz} + F_{Lz}.
\end{aligned}
$$

Defining the right and left wing forces as half of the desired body force plus a differential force gives

$$\begin{aligned} F_{Rx} &= \frac{F_{xd}}{2} + \Delta F_{Rx} \\ F_{Lx} &= \frac{F_{xd}}{2} + \Delta F_{Lx} \\ F_{Ry} &= \Delta F_{Ry} \\ F_{Ly} &= \Delta F_{Ly} \\ F_{Rz} &= \frac{F_{zd}}{2} + \Delta F_{Rz} \\ F_{Lz} &= \frac{F_{zd}}{2} + \Delta F_{Lz}. \end{aligned}$$

Therefore, the sum of the forces in terms of the desired net force plus right and left control forces becomes

$$\begin{aligned} F_x &= F_{xd} + \Delta F_{Rx} + \Delta F_{Lx} \\ F_y &= \Delta F_{Ry} + \Delta F_{Ly} \approx 0 \\ F_z &= F_{zd} + \Delta F_{Rz} + \Delta F_{Lz}. \end{aligned}$$

For this case net moments in the y-direction are added to the torques created by the net wing forces. These moments are defined as

$$\begin{aligned} \vec{M}_R &= M_R \hat{\imath}_y \\ \vec{M}_L &= M_L \hat{\imath}_y. \end{aligned}$$

The desired control torques are the same as before,

$$\begin{aligned} T_x &= K_x \frac{\Omega_{b3} + \Omega_{c3}}{2\sin(\alpha)} \\ T_y &= -K_y \frac{\Omega_{b3} - \Omega_{c3}}{2\cos(\alpha)} \\ T_z &= K_z \Omega_{b1} = K_z \Omega_{c1}. \end{aligned}$$

Summing the torques and moments and equating them to the desired control commands gives

$$\begin{aligned}
K_x\frac{\Omega_{b3}+\Omega_{c3}}{2\sin(\eta)} &= (\frac{F_{zd}}{2}+\Delta F_{Rz})(w+L\cos(\alpha_0+\delta_{\alpha R})) \\
&\quad -(\frac{F_{zd}}{2}+\Delta F_{Lz})(w+L\cos(\alpha_0+\delta_{\alpha L})) \\
&\approx (\Delta F_{Rz}(w+L\cos(\alpha_0+\delta_{\alpha R}))-\Delta F_{Lz}(w+L\cos(\alpha_0+\delta_{\alpha L}))) \\
-K_y\frac{\Omega_{b3}-\Omega_{c3}}{2\cos(\eta)} &= -((\frac{F_{zd}}{2}+\Delta F_{Rz})(d-L\sin(\alpha_0+\delta_{\alpha R})) \\
&\quad +(\frac{F_{zd}}{2}+\Delta F_{Lz})(d-L\sin(\alpha_0+\delta_{\alpha L})))+M_R+M_L \\
K_z\Omega_1 &= (\Delta F_{Ry}+\Delta F_{Ly})(d-L\sin(\alpha_0+\delta_{\alpha R})) \\
&\quad +(\Delta F_{Lx}-\Delta F_{Rx})(w+L\cos(\alpha_0+\delta_{\alpha R})).
\end{aligned}$$

The net force in the lateral direction will still be assumed to be small. Breaking up the torques into left and right components gives

$$\begin{aligned}
K_x\frac{\Omega_{b3}}{2\sin(\eta)} &= \Delta F_{Rz}(w+L\cos(\alpha_0+\delta_{\alpha R})) \\
K_x\frac{\Omega_{c3}}{2\sin(\eta)} &= -\Delta F_{Lz}(w+L\cos(\alpha_0+\delta_{\alpha L})) \\
-K_y\frac{\Omega_{b3}}{2\cos(\eta)} &= -(\frac{F_{zd}}{2}+\Delta F_{Rz})(d-L\sin(\alpha_0+\delta_{\alpha R}))+M_R \\
K_y\frac{\Omega_{c3}}{2\cos(\eta)} &= -(\frac{F_{zd}}{2}+\Delta F_{Lz})(d-L\sin(\alpha_0+\delta_{\alpha L}))+M_L \\
K_z\frac{\Omega_1}{2} &= \Delta F_{Lx}(w+L\cos(\alpha_0+\delta_{\alpha R})) \\
K_z\frac{\Omega_1}{2} &= -\Delta F_{Rx}(w+L\cos(\alpha_0+\delta_{\alpha R})).
\end{aligned}$$

Assuming that the angles $\delta_{\alpha R}$ and $\delta_{\alpha L}$ are intentionally trimmed to zero, these expressions become

$$\begin{aligned}
K_x\frac{\Omega_{b3}}{2\sin(\eta)} &= \Delta F_{Rz}(w+L\cos(\alpha_0)) \\
K_x\frac{\Omega_{c3}}{2\sin(\eta)} &= -\Delta F_{Lz}(w+L\cos(\alpha_0))
\end{aligned}$$

$$
\begin{aligned}
-K_y \frac{\Omega_{b3}}{2\cos(\eta)} &= M_R \\
K_y \frac{\Omega_{c3}}{2\cos(\eta)} &= M_L \\
K_z \frac{\Omega_1}{2} &= \Delta F_{Lx}(w + L\cos(\alpha_0)) \\
K_z \frac{\Omega_1}{2} &= -\Delta F_{Rx}(w + L\cos(\alpha_0)).
\end{aligned}
$$

Therefore, the control parameters can be found directly to be

$$
\begin{aligned}
\Delta F_{Rz} &= K_x \frac{\Omega_{b3}}{2\sin(\eta)(w + L\cos(\alpha_0))} \\
\Delta F_{Lz} &= -K_x \frac{\Omega_{c3}}{2\sin(\eta)(w + L\cos(\alpha_0))} \\
M_R &= -K_y \frac{\Omega_{b3}}{2\cos(\eta)} \\
M_L &= K_y \frac{\Omega_{c3}}{2\cos(\eta)} \\
\Delta F_{Lx} &= K_z \frac{\Omega_1}{2(w + L\cos(\alpha_0))} \\
\Delta F_{Rx} &= -K_z \frac{\Omega_1}{2(w + L\cos(\alpha_0))}.
\end{aligned}
$$

Summing the torques on the left and the right gives

$$
\begin{aligned}
T_x &= (\Delta F_{Rz} - \Delta F_{Lz})(w + L\cos(\alpha_0)) \\
&= K_x \frac{\Omega_{b3} + \Omega_{c3}}{2\sin(\eta)} = -K_x p \\
T_y &= M_R + M_L = K_y \frac{\Omega_{c3} - \Omega_{b3}}{2\cos(\eta)} \\
&= -K_y q \\
T_z &= (\Delta F_{Lx} - \Delta F_{Rx})(w + L\cos(\alpha_0)) \\
&= K_z \frac{\Omega_1 + \Omega_1}{2} = -K_z r \\
F_x &= F_{xd} \\
F_y &\approx 0 \\
F_z &= F_{zd} + \Delta F_{Rz} + \Delta F_{Lz}.
\end{aligned}
$$

Therefore, the roll moment is nominally controlled by the difference between the left and right vertical force (body relative) generated by the wings. Pitch torque is generated by the moments generated by the wings and the yaw force is generated by the forward or rearward lateral force generated by the wings. The sum of the forces is used to provide forward velocity and to counteract gravity, with the net lateral force assumed to be small.

REFERENCES

[1] W. P. Chan and M. H. Dickinson, "Position specific central projections of mechanosensory neurons on the haltere of the blow fly, *Calliphora* ," *J Comp Neurol*, vol. 369(3), pp. 405–418, 1996.

[2] J. L. Fox and T. L. Daniel, "A neural basis for gyroscopic force measurement in the halteres of *Holorusia*," *J Comp Physiol A*, vol. 194, pp. 887–897, 2008.

[3] R. Hengstenberg, "Mechanosensory control of compensatory head roll during flight in the blowfly *Calliphora erythrocephala Meig.*" *J Comp Physiol A*, vol. 163, pp. 151–165, 1988.

[4] W.-C. Wu and R. Wood, "Angular rate sensor using micro electromechanical haltere," United States Patent 7107842, Sep. 2006.

[5] G. Fraenkel, "The function of the halteres of flies," *Proc. Zool. Soc. Lond. A*, vol. 109, pp. 69–78, 1939.

[6] W. Derham, *Physico-theology. 3rd edn*, W. Innys, Ed. London, 1714.

[7] H. Loew, "Uber die schwinger der dipteren," *Berl Ent Zeitschr*, vol. 2, pp. 225–230, 1858.

[8] F. J. Schelver, "Beobachtungen uber den flug and das gesumme einiger zweiflugliger insekten und insbesondere uber die schwingkolbechen und schuppchen unter den flugeldecken," *Wiedemann's Arch Zool. Jahrb. Physiol.*, vol. 2, pp. 210–218, 1802.

[9] J. de Bellesme, "Rech. exp. sur les fonctions du balancier chez les insectes dipteres," *Paris*, 1867.

[10] E. Weinland, "Uber die schwinger (halteren) der dipteren," *Zeitschr wiss Zool*, vol. 51, pp. 55–166, 1891.

[11] W. v. Buddenbrock, "Einige bermerkungen uber den schwirrflug der insekten mit besonderer berucksichtigung der halteren der zweiflugler," *Verh Heidelb Nat Med Ver N F 13*, vol. 13, 1917.

[12] ——, "Die vermutliche losung der halterenfrage," *Pflug Archiv*, vol. 175, pp. 125–164, 1919.

[13] G. Fraenkel and J. W. S. Pringle, "Halteres of flies as gyroscopic organs of equilibrium," *Nature*, vol. 141, pp. 919–920, 1938.

[14] J. W. S. Pringle, "The gyroscopic mechanism of the halteres of diptera," *Philos T Roy Soc B*, vol. 233, pp. 347–384, Nov. 1948.

[15] A. Brauns, "Morphologische und physiologische untersuchungen zum halterenproblem unter besonderer berucksichtigung brachypterer arten," *Zool Jahrb Physiol*, vol. 59, pp. 245–386, 1939.

[16] J. W. S. Pringle, *Insect Flight*. Cambridge University Press, 1957.

[17] R. Faust, "Untersuchungen sum haleterenproblem," *Zool. Jahrb. Physiol.*, vol. 63, pp. 325–366, 1952.

[18] D. C. Sandeman and H. Markl, "Head movements in flies (calliphora) produced by deflexion of the halteres," *J. Exp. Biol.*, vol. 85, pp. 43–60, 1980.

[19] D. C. Sandeman, "Angular acceleration, compensatory head movements and the halteres of flies (*Lucilia serricata*)," *J Comp Physiol A*, vol. 136, pp. 361–367, 1980.

[20] R. Hengstenberg, D. C. Sandeman, and B. Hengstenberg, "Compensatory head roll in the blowfly *Calliphora* during flight," *Proc. R. Soc. Lond. B*, vol. 227, pp. 455–482, 1986.

[21] R. Hengstenberg, "Multisensory control in insect oculomotor systems," in *Visual motion and its role in the stabilization of gaze*, F. Miles and J. Wallman, Eds. Elsevier, 1992, ch. 13, pp. 285–298.

[22] ——, "Stabilizing head/eye movements in the blowfly *Calliphora erythrocephala*," in *The head-neck sensory motor system*, P. V. A. Berthoz, W. Graf, Ed. Oxford University Press, 1992, ch. 5, pp. 49–55.

[23] G. Nalbach, "The halteres of the blowfly *Calliphora* I. Kinematics and dynamics," *J Comp Physiol A*, vol. 173, pp. 293–300, Sep. 1993.

[24] ——, "Extremely non-orthogonal axes in a sense organ for rotation: Behavioural analysis of the dipteran haltere system," *J Neurosci*, vol. 61, pp. 149–163, Jan. 1994.

[25] G. Nalback and R. Hengstenberg, "The halteres of the blowfly *Calliphora* II. Three-dimensional organization of compensatory reactions to real and simulated rotations," *J Comp Physiol A*, vol. 175, pp. 695–708, Dec. 1994.

[26] W. P. Chan, F. Prete, and M. Dickinson, "Visual input to the efferent control system of a fly's "gyroscope"," *Science*, vol. 280, p. 289:292, 1998.

[27] G. Heide, "Neural mechanisms of flight control in diperta," in *Insect flight. BIONA Report 2, vol 1*, N. W, Ed. Fischer, Stuttgart, 1983, pp. 35–52.

[28] A. Fayyazuddin and M. H. Dickinson, "Haltere afferents provide direct, electronic input to a steering motor neuron in the blowfly, *Calliphora*," *J Neurosci*, vol. 16, pp. 5225–5232, 1996.

[29] H. Pflugstaedt, "Die halteren der dipteren," *Z Wiss Zool*, vol. 100, pp. 1–58, 1912.

[30] W. Gnatzy, U. Grunert, and M. Bender, "Campaniform sensilla of *Calliphora vicina* I. Topography," *Zoomorphology*, vol. 106, pp. 312–319, 1987.

[31] J. W. S. Pringle, "Proprioception in insects II. The action of the campaniform sensilla on the legs," *J Exp Biol*, vol. 15, pp. 114–131, 1938.

[32] U. Thurm, A. Stedtler, and R. Foelix, "Reizwirksame verformungen der terminalstrukturen eines mechanorezeptors," *Verh Dtsch Zool Ges*, vol. 67, pp. 37–41, 1974.

[33] A. Stedtler, "Die reprasentation von schwingungen der fliegenhatlere in den reaktionen ihrer mechanorezeptor-felder," *Staatsexamens-Arbeit, Universitat Bochum*, 1974.

[34] S. N. Zill and D. T. Moran, "The exoskeleton and insect proprioception. I. Responses of tibial campaniform sensilla to external and muscle-generated forces in the american cockroach, *Periplaneta americana*," *J Exp Biol*, vol. 91, pp. 1–24, 1981.

[35] M. Dickinson, "Comparison of encoding properties of campaniform sensilla on the fly wing," *J Exp Biol*, vol. 151, pp. 245–261, 1990.

[36] R. C. Elson, "Flight motor neurone reflexes driven by strain-sensitive wing mechanoreceptors in the locust," *J Comp Physiol A*, vol. 161, pp. 747–760, 1987.

[37] ——, "Interneuronal processing of inputs from the campaniform sensilla of the locust hindwing," *J Comp Physiol A*, vol. 161, pp. 761–776, 1987.

[38] A. Mielke and G. Heide, "Effects of artificially generated haltere nerve afferences on the activation of the flight steering muscles in *Calliphora*. gene-brain-behavior," in *Proceedings of teh 21st Gottingen Neurobiology Conference*, N. Elsner and M. Heisenberg, Eds. Stuttgart: Thieme, 1993, p. 207.

[39] M. Egelhaaf, "Visual afferences to flight steering muscles controlling optomotor responses of the fly," *J Comp Physiol A*, vol. 165, pp. 719–730, 1989.

[40] G. Heide and K. G. Gotz, "Optomotor control of course and altitude in *Drosophila* is achieved by at least three pairs of flight steering muscles," *J Exp Biol*, vol. 199, pp. 1711–1726, 1996.

[41] F. S. J. Hollick, "The flight of the dipterous fly *Muscina stabulans* (fallen)," *Philos T Roy Soc B*, vol. 230, pp. 357–390, Nov. 1940.

[42] M. Dickinson, "Haltere-mediated equilibrium reflexes of the fruit fly, *Drosophila melanogaster*," *Philos T Roy Soc B*, vol. 354, pp. 903–916, May 1999.

[43] C. N. Balint and M. H. Dickinson, "The correlation between wing kinematics and steering muscle activity in the blowfly *Calliphora vicina*," *J Exp Biol*, vol. 204, pp. 4213–4226, 2001.

[44] ——, "Neuromuscular control of aerodynamic forces and moments in the blowfly, *Calliphora vicina*," *J Exp Biol*, vol. 207, pp. 3813–3838, 2004.

[45] A. R. Ennos, "The kinematics and aerodynamics of the free flight of some diperta," *J Exp Biol*, vol. 142, pp. 49–85, 1989.

[46] J. A. Bender and M. H. Dickinson, "A comparison of visual and haltere-mediated feedback in the control of body saccades in *Drosophila melanogaster*," *J Exp Biol*, vol. 209, pp. 4597–4606, 2006.

[47] A. Sherman and M. H. Dickinson, "A comparison of visual and haltere-mediated equilibrium reflexes in the fruit fly," *J Exp Biol*, vol. 206, pp. 295–302, Jan. 2003.

[48] J. A. Bender and M. H. Dickinson, "Visual stimulation of saccades in magnetically tethered *Drosophila*," *J Exp Biol*, vol. 209, pp. 3170–3182, 2006.

[49] M. S. Tu and M. H. Dickinson, "Modulation of negative work output from a steering muscle of the blowfly, *Calliphora vicina*," *J Exp Biol*, vol. 192, pp. 2007–224, 1994.

[50] ——, "The control of wing kinematics by two steering muscles of the blowfly, *Calliphora vicina*," *J Comp Physiol A*, vol. 178, pp. 813–830, 1996.

[51] A. Fayyazuddin and M. H. Dickinson, "Convergent mechanosensory input structures the firing phase of a steering motor neuron in the blowfly *Calliphora*," *J. Neurophysiol.*, vol. 82, pp. 1916–1926, Oct. 1999.

[52] V. Apostolyuk, "Theory and design of micromechanical vibratory gyroscopes," *MEMS/NEMS Handbook, Springer*, vol. 1, p. 173:195, 2006.

[53] C. Schilstra and J. H. Van Hateren, "Blowfly flight and optic flow I. Thorax kinematics and flight dynamics," *J Exp Biol*, vol. 202, pp. 1481–1490, 1999.

[54] G. K. Taylor and H. G. Krapp, "Sensory systems and flight stability: What do insects measure and why?" *Adv. Insect Physiol.*, vol. 34, 2008.

[55] P. N. R. Usherwood, H. I. Runion, and J. I. Campbell, "Structure and physiology of a chordotonal organ in the locust leg," *J Exp Biol*, vol. 48, pp. 305–323, 1968.

[56] G. S. Fraenkel and D. L. Gunn, *The orientation of animals: kinesis, taxes and compass reactions*. Dover, 1961.

[57] S. Uga and M. Kuwabara, "The fine structure of campaniform sensillum on the haltere of the fleshfly *Boettcherisca peregrina*," *J. Electron Microsc.*, vol. 16, pp. 304–312, Aug. 1967.

[58] U. Grunert and W. Gnatzy, "Campaniform sensilla of *Calliphora vicina* (insecta, diptera) II. Typology," *Zoomorphology*, vol. 106, pp. 320–328, 1987.

[59] S. N. Zill, D. T. Moran, and F. G. Varela, "The exoskeleton and insect proprioception. II. Reflex effects of tibial campaniform sensilla in the american cockroach, *Periplaneta americana*," *J Exp Biol*, vol. 94, pp. 43–55, 1981.

[60] S. N. Zill and D. T. Moran, "The exoskeleton and insect proprioception. III. Activity of tribal campaniform sensilla during walking in the american cockroach, *Periplaneta americana*," *J Exp Biol*, vol. 94, pp. 57–75, 1981.

[61] J. A. Miyan and A. W. Ewing, "How diptera move their wings: A re-examination of the wing base articulation amd muscle systems concerned with flight," *Philos T Roy Soc B*, vol. 311, pp. 271–302, 1985.

[62] J. M. Zanker, "The wing beat of *Drosophila melanogaster*. III. Control," *Philos T Roy Soc B*, vol. 327, pp. 45–64, 1990.

[63] D. L. Grodnitsky, "Evolution and classification of insect flight kinematics," *Evolution*, vol. 49, pp. 1158–1162, 1995.

[64] M. Dickinson and M. S. Tu, "The function of dipteran flght muscle," *Comp. Biochem. Physiol.*, vol. 116A, p. 223:238, 1997.

[65] G. K. Taylor, "Mechanics and aerodynamics of insect flight control," *Biol. Rev.*, vol. 76, pp. 449–471, 2001.

[66] M. H. Dickinson, "Insect flight," *Current Biology*, vol. Vol 16 No 9, pp. R310–R314, 2006.

[67] M. H. Dickinson, F.-O. Lehmann, and W. P. Chan, "The control of mechanical power in insect flight," *Amer. Zool.*, vol. 38, pp. 718–728, 1998.

[68] N. J. Strausfeld and W. Gronenberg, "Descending neuron supplying the neck and flight motor of diptera: Organization and neuroanatomical relationships with visual pathways," *J. Comp. Neurol.*, vol. 302, pp. 954–972, 1990.

[69] W. F. Phillips, *Mechanics of Flight*. Wiley, Hoboken, NJ, ISBN 0-471-33458-8, 2004.

[70] K. E. Atkinson, *An Introduction to Numerical Analysis Second Edition*. John Wiley & Sons, 1989.

[71] H. K. Khalil, *Nonlinear Systems Third Edition*. Prentice Hall, 2002.

[72] V. Braitenberg, *Vehicles: Experiments in synthetic psychology*. MIT Press, 1986.

BIOGRAPHICAL SKETCH

Rhoe Thompson is an Aerospace Engineer employed by the Air Force Research Laboratory at Eglin Air Force Base. He received his BS and ME degrees at the University of Florida in 1986 and 1992, respectively. In October 1986 he began working in the Air Force Armament Laboratory on missile defense technology development associated with guidance and control of kinetic energy interceptors. General activities, while still related to missile defense, changed in the early 1990's to become focused on ground testing of infrared guidance systems in hardware-in-the-loop environments. In 2001, he assumed the role of Chief Engineer of the Kinetic Kill Vehicle Hardware-In-The Loop Facility (KHILS), an internationally renowned facility for testing weapons and development of test technologies. Currently, while pursuing his Ph.D. he is a member of a team of engineers within AFRL studying biological systems for application to micro- air vehicles and innovative sensor systems.